https://doi.org/10.15388/vu.thesis.228
https://orcid.org/0000-0001-9673-0507

VILNIAUS UNIVERSITETAS

Dominyka
DAPKUTĖ

Mezenchiminių kamieninių ir vėžinių ląstelių atsakas į teranostinių nanodalelių poveikį – ląstelių terapijos link

DAKTARO DISERTACIJA

Gamtos mokslai,
Biofizika (N 011)

VILNIUS 2021

Disertacija rengta 2016-2020 metais Vilniaus universiteto Gyvybės mokslų centro Biomokslų institute.
Eksperimentiniai darbai atlikti Nacionaliniame vėžio institute, Biomedicininės fizikos laboratorijoje.
Mokslinius tyrimus rėmė Lietuvos mokslo taryba (2017-2019 m.m. gauta stipendija už akademinius pasiekimus).

Mokslinis vadovas:
prof. habil. dr. Ričardas Rotomskis (Vilniaus universitetas, gamtos mokslai, biofizika – N 011).

Gynimo taryba:
Pirmininkas – **prof. dr. Daumantas Matulis** (Vilniaus universitetas, gamtos mokslai, biofizika – N 011).
Nariai:
dr. Petras Juzėnas (Norvegijos Radžio ligoninės Vėžio tyrimų institutas, Oslo universitetinė ligoninė, gamtos mokslai, biofizika – N 011).
dr. Augustas Pivoriūnas (Valstybinis mokslinių tyrimų institutas Inovatyvios medicinos centras, gamtos mokslai, biochemija – N 004).
prof. habil. dr. Vytenis Arvydas Skeberdis (Lietuvos sveikatos mokslų universitetas, gamtos mokslai, biofizika – N 011).
prof. dr. Edita Sužiedėlienė (Vilniaus universitetas, gamtos mokslai, biochemija – N 004).

Disertacija ginama viešame Gynimo tarybos posėdyje 2021 m. rugsėjo mėn. 30 d. 10 val. Vilniaus universiteto Gyvybės mokslų centro R-401 auditorijoje.
Adresas: Saulėtekio al. 7, LT-10527, Vilnius, Lietuva
Tel. +37052234420; el. paštas: info@gmc.vu.lt.

Disertaciją galima peržiūrėti Vilniaus universiteto bibliotekoje ir VU interneto svetainėje adresu: https://www.vu.lt/naujienos/ivykiu-kalendorius

https://doi.org/10.15388/vu.thesis.228
https://orcid.org/0000-0001-9673-0507

VILNIUS UNIVERSITY

Dominyka
DAPKUTĖ

Mesenchymal stem cell and cancer cell response to treatment with theranostic nanoparticles – towards cell therapy

DOCTORAL DISSERTATION

Natural Sciences,
Biophysics (N 011)

VILNIUS 2021

This dissertation was prepared between at Vilnius University Life Sciences Center Institute of Biosciences between 2016 and 2020.
Experimental work was carried out at the National Cancer Institute, Biomedical Physics Laboratory.
The research was supported by Research Council of Lithuania (a scholarship was granted for academic achievement in 2017-2019).

Academic supervisor:
Prof. Habil. Dr. Ričardas Rotomskis (Vilnius University, Natural Sciences, Biophysics – N 011)

Dissertation Defense Panel:
Chairman – **Prof. Dr. Daumantas Matulis** (Vilnius University, Natural Sciences, Biophysics – N 011).
Members:
Dr. Petras Juzenas (Institute for Cancer Research, Norwegian Radium Hospital, Oslo University Hospital, Natural Sciences, Biophysics – N 011).
Dr. Augustas Pivoriunas (State Research Institute Centre for Innovative Medicine, Natural Sciences, Biochemistry – N 004).
Prof. Habil. Dr. Vytenis Arvydas Skeberdis (Lithuanian University of Health Sciences, Natural Sciences, Biophysics – N 011).
Prof. dr. Edita Suziedeliene (Vilnius University, Natural Sciences Biochemistry – N 004).

The dissertation shall be defended at a public meeting of the Dissertation Defense Panel at 10 h on 30th September 2021 in the meeting room R-401 of Vilnius University Life Sciences Center.
Address: Sauletekio ave. 7, LT-10527, Vilnius, Lithuania
Tel. +37052234420; e-mail: info@gmc.vu.lt.

The text of this dissertation can be accessed at the library of Vilnius University as well as on the website of Vilnius University: www.vu.lt/lt/naujienos/ivykiu-kalendorius

TURINYS

SANTRUMPOS

AFM – atomo jėgos mikroskopas (angl. *atomic force microscope*)
APC – alofikocianinas (angl. *allophycocyanin*)
Ce6 – chlorinas e6 (angl. *chlorin e6*)
CXCR4 – C-X-C motyvą turintis receptorius 4
DLS – dinaminė šviesos sklaida (angl. *dynamic light scattering*)
DMEM – Dulbecco‘s modifikuota Eagle terpė (angl. *Dulbecco's Modified Eagle Medium*)
DPBS – Dulbecco‘s fosfatinis buferinis tirpalas (angl. *Dulbecco phosphate buffer saline*)
EPR – padidintas pralaidumas ir užsilaikymas (angl. *enhanced permeability and retention*)
EthD-1 – etidžio homodimeras-1
FBS – fetalinis veršiuko serumas (angl. *fetal bovine serum*)
FITC – fluoresceino izotiocianatas (angl. *fluorescein isothiocyanate*)
FLIM – fluorescencijos gyvavimų trukmių mikroskopija (angl. *fluorescence lifetime imaging microscopy*)
FRET – Fiorsterio rezonansinė energijos pernaša (angl. *Förster resonance energy transfer*)
GFP – žaliai fluorescuojantis baltymas (angl. *green fluorescent protein*)
KT – kvantiniai taškai (angl. *quantum dots*)
KT-Ce6 – kvantinių taškų ir fotosensibilizatoriaus chlorino e6 kompleksas
LDH – laktatodehidrogenazė (angl. *lactate dehydrogenase*)
LLC – Luiso plaučių karcinomos ląstelių linija (angl. *Lewis lung carcinoma*)
MKL – mezenchiminės kamieninės ląstelės (angl. *mesenchymal stem cells*)
P/S – antibiotikų penicilino ir streptomicino mišinys
PBS – fosfatinis buferinis tirpalas (angl. *phosphate buffered saline*)
PDT – fotodinaminė terapija (angl. *photodynamic therapy*)
PE – fikoeritrinas (angl. *phycoerythrin*)
PEG – polietilenglikolis (angl. *polyethylene glycol*)
PFA – paraformaldehidas
PL – fotoliuminescencija (angl. *photoluminescence*)
PS – fotosensibilizatorius (angl. *photosensitizer*)
SOSG – žaliasis singuletinio deguonies jutiklis (angl. *singlet oxygen sensor green*)

Drąsios idėjos yra tarsi judančios šachmatų figūros. Jos gali būti numuštos, bet gali ir pradėti pergalingą žaidimą.[1]

Johanas Volfgangas fon Gėtė

ĮVADAS

Vėžys išlieka viena mirtingiausių ligų pasaulyje, kai kuriose šalyse išstumianti širdies ir kraujagyslių ligas iš pirmosios vietos. Skaičiuojama, kad 2020 metais onkologinė liga buvo diagnozuota beveik 19,3 mln. žmonių pasaulyje ir nusinešė 10 mln. gyvybių (Sung ir kt., 2021). Onkologinių susirgimų daugiaveidiškumas, imuninės sistemos nesugebėjimas sukontroliuoti ligos bei greitai įgyjamas atsparumas gydymui neleidžia medikams visuomet sėkmingai kovoti su vėžiu. Ankstyvosios diagnostikos trūkumas ir prastas chemoterapinių vaistų selektyvumas yra vieni pagrindinių onkologijos iššūkių.

Fotosensibilizatorių (PS) ir nanodalelių kompleksai gali tapti terapiniu metodu, sprendžiančiu dabartines vėžio gydymo problemas (Chilakamarthi ir Giribabu, 2017). PS yra terapinės molekulės, kurios yra inertiškos tamsoje, bet ląstelėms toksiškomis tampa UV-Vis spektriniame diapazone – dėl molekulinių virsmų kaskadų susidaro aktyviosios deguonies formos. Kadangi terapinis poveikis pasiekiamas tik apšvietus šviesa ir fotodinaminė terapija (PDT) veikia lokaliai, sisteminiai šalutiniai poveikiai, įprasti standartinei chemoterapijai, sumažėja, o gydymo efektyvumas padidėja (Dougherty et al., 1998). PDT ne tik tiesiogiai sunaikina vėžines ląsteles, bet ir pažeidžia naviko kraujagysles bei sukelia imuninės sistemos aktyvaciją, todėl sustabdomas tolimesnis naviko augimas ir tuo pačiu sužadinamas priešvėžinis imunitetas (Agostinis ir kt., 2011). PDT yra minimaliai invazinė ir nereikalauja kompleksinių chirurginių intervencijų, gali būti kartojama kelis kartus be kaupiamojo toksiškumo, veiksmingai naikina ar bent jau sumažina naviko ribas (Triesscheijn ir kt., 2006). Per pastaruosius keturis dešimtmečius PDT veiksmingumas buvo įrodytas šlapimo pūslės, plaučių, stemplės, smegenų, galvos ir kaklo, gimdos kaklelio ir odos vėžio atvejais (Huang, 2005). Vienas iš perspektyvesnių PDT taikomų PS yra chlorinas e6 (Ce6) – iš chlorofilo gaunamas antros kartos fotosensibilizatorius, turintis stiprią sugertį raudonojoje spektro dalyje ir didelį singuletinio deguonies generavimo

[1] *"Gewagte Ideen sind wie das Ziehen von Schachfiguren. Sie können geschlagen werden, aber sie können eine Siegespartie eröffnen."* Johann Wolfgang von Goethe

našumą (Cunderlíková ir kt., 1999). Vis dėlto, jo panaudojimą klinikinėje praktikoje riboja nedidelis susikaupimas navike.

Tobulėjant nanotechnologijoms, PDT nebuvo pamiršta. Nanodalelės, pagamintos tiek iš natūralių, tiek iš sintetinių junginių, gali išspręsti daugelį kylančių terapinių problemų. Pirma, dėl didelio paviršiaus ploto prie nanodalelių galima prijungti daugybę PS molekulių bei įvairius kitus priešvėžinius vaistus, kurie veikia sinergiškai. Antra, nanodalelės gali apsaugoti į navikus gabenamas terapines molekules nuo biologinės aplinkos poveikio, taip pat išspręsti agregacijos ir hidrofobiškumo problemas, būdingas hidrofobiniams arba amfifiliniams fotosensibilizatoriams (Lucky ir kt., 2015). Nanomedžiagos taip pat įgyja unikalių savybių, pavyzdžiui, nuo dydžio priklausomą didelio kvantinio našumo fotoliuminescenciją (PL). Optinė biopsija, paremta fluorescencinės spektroskopijos ir vaizdinimo metodikomis, galėtų būti tinkama priemonė vizualizuojant navikus ar metastazes bei jų ribas (Wang ir Van Dam, 2004), o dabartinių neefektyvių optinių žymenų problemas gali išspręsti nanodalelės. Puslaidininkinės fotoliuminescuojančios nanodalelės kvantiniai taškai (KT) pasižymi geresnėmis optinėmis savybėmis nei bet kokie organiniai dažikliai, jos yra stabilesnės, ryškesnės, turi platų sugerties ir siaurą PL spektrus, didelį daugiafotonio sužadinimo skerspjūvį (Yao ir kt., 2018). KT taip pat gali veikti kaip energijos donorai – esant KT fotoliuminescencijos ir PS sugerties spektrų sanklotai bei nanodalelei ir PS esant kelių nanometrų atstumu, tarp jų gali vykti Fiorsterio rezonansinė energijos pernaša (FRET) (Valanciunaite ir kt., 2014). Taip susiformavus KT ir PS kompleksui ar biokonjugatui gaunama *teranostinė* platforma – ryški nanodalelių PL atlieka diagNOSTINĘ funkciją, o PS – TERApinę.

Vis dėlto, pačios nanodalelės ir jų kompleksai neužtikrina pakankamo selektyvumo navikams ir yra linkusios nespecifiškai kauptis tam tikruose organuose, pavyzdžiui, kepenyse, limfmazgiuose, blužnyje. Nesvarbu, kokia nanodalelių pristatymo strategija pasirenkama – pasyvus (pasitelkiant EPR efektą) ar aktyvus (funkcionalizuojant naviką atpažįstančiomis molekulėmis), daugiau nei 99 % suleistų nanodalelių atsiduria mononuklearinėje fagocitų sistemoje (Polo ir kt., 2017). Neseniai atliktas tyrimas parodė, kad tik 0,7 % iš intraveniškai suleistų nanodalelių pasiekia navikus, o kadangi navikai sudaryti iš skirtingų ląstelių tipų, įskaitant nevėžines ląsteles, su nanodalelėmis kontaktuoja tik 2 iš 100 piktybinių ląstelių. Tai reiškia, kad vos 0,0014 % iš sistemiškai pateiktų nanodalelių sąveikauja su vėžinėmis ląstelėmis (Dai ir kt., 2018).

Terapinių medžiagų transportavimas ląstelėmis prieš porą dešimtmečių buvo pasiūlytas kaip alternatyvus nanodalelių pristatymo būdas. Eritrocitai, makrofagai ir limfocitai jau buvo panaudoti tokiai užduočiai atlikti, tačiau jų selektyvumas navikams ribotas (Singh ir Mitragotri, 2020). Priešnavikinių vaistų pristatymas naudojant ląsteles, natūraliai migruojančias į navikus, yra biologiškai suderinamas, kliniškai saugus ir ikiklinikinių tyrimų metu parodė didelę sėkmę (McMillan ir kt., 2011). Mezenchiminės kamieninės ląstelės (MKL) yra laikomos vienu iš perspektyviausių pasirinkimų. MKL yra multipotentinės ląstelės, turinčios imunomoduliacinių, regeneracinių ir onkotropinių savybių. MKL į navikus migruoja chemokinų koncentracijos gradiento kryptimi ir gali patekti į pagrindinį naviką bei į tolimesnes mikro- ir makrometastazes (Momin ir kt., 2010). Remiantis tyrimais, toks nanodalelių transportavimo būdas padidina nanodalelių kiekį navike keturiais kartais (Durymanov ir kt., 2015).

Norint pasiūlyti navikų ankstyvosios diagnostikos ir terapijos problemų sprendimo būdą, šiame darbe tirtas mezenchiminių kamieninių ir vėžinių ląstelių atsakas į nanodaleles, bei KT ir fotosensibilizatoriaus Ce6 komplekso, gabenamo mezenchiminėmis kamieninėmis ląstelėmis, potencialios teranostinės galimybės.

Darbo tikslas: ištirti odos mezenchiminių kamieninių ląstelių gebėjimą selektyviai nugabenti į navikus teranostines nanodaleles, užtikrinant terapinį poveikį ir diagnostinį potencialą.

Darbo uždaviniai:

1. Ištirti KT susikaupimą ir pasiskirstymą 2D, 3D vėžinių ląstelių monokultūrose ir *in vivo* navikų modeliuose.
2. Suformuoti KT ir Ce6 kompleksą, ištirti jo fizikochemines savybes, singuletinio deguonies generacijos efektyvumą, stabilumą skirtingose terpėse ir baltymų įtaką KT-Ce6 kompleksui.
3. Išskirti odos MKL eksplantų kultūros metodu ir charakterizuoti jas pagal MKL požymius.
4. Nustatyti KT ir KT-Ce6 komplekso kaupimąsi odos MKL bei ląstelių gebėjimą transportuoti nanodaleles *in vitro* ir *in vivo* sistemose.
5. Įvertinti KT-Ce6 komplekso, gabenamo odos MKL, diagnostinį ir fotodinaminį efektyvumą *in vitro* ir *in vivo* sistemose.

Mokslinis naujumas

Įprastai tokio tipo tyrimai atliekami su kaulų čiulpų ar riebalinio audinio kamieninėmis ląstelėmis, o su dermos MKL atliekamų tyrimų skaičius nedidelis. Mūsų žiniomis, migraciniai ir teranostinių medžiagų transportavimo tyrimai su tokiomis ląstelėmis atlikti pirmą kartą. Dėl didelio regeneracijos poreikio, odos audiniuose yra gausu MKL, o pats audinys gali būti paimamas minimaliai invazinėmis procedūromis, greitai regeneruoja, turi didelį paviršiaus plotą. Oda, likusi po įvairių operacijų kaip medicininės atliekos, galėtų būti lengvai panaudojama ekonomiškam ir donorui draugiškam priešvėžiniam gydymui.

Disertacinis darbas atliktas su žmogaus odos MKL, kurių išskyrimui naudotas eksplantų kultūros metodas. Tai yra santykinai retai naudojamas kamieninių ląstelių išskyrimo metodas. Kituose moksliniuose tyrimuose kamieninės ląstelės gaunamos naudojant fermentinės disociacijos būdą, kuomet įvairūs fermentai atpalaiduoja MKL iš donorinio audinio. Tačiau tokia procedūra gali neigiamai paveikti ląstelių paviršiaus baltymus, MKL savybes, tokias kaip proliferacija, heterogeniškumas ir išeiga. Naudojant eksplantų kultūrą yra išlaikoma MKL mikroaplinka – tarpląstelinis užpildas, stromos ląstelės, signalinės molekulės, citokinai, augimo faktoriai, 3D aplinka, todėl perėjimas į 2D ląstelių kultūrą yra švelnesnis, tokios MKL pasižymi didesniu proliferacijos pajėgumu, galima gauti didelius MKL kiekius iš mažo kiekio donorinės medžiagos.

Darbe buvo naudotos žmogaus MKL, o migracijos efektas gautas nepaisant rūšinių barjerų – MKL migravo ir imunodeficitinėse pelėse su žmogaus naviku (signalas žmogus→žmogus), ir pelėse su pelės naviku (signalas žmogus→pelė), todėl buvo parodytas terapijos universalumas bei maža alogeninių reakcijų tikimybė ateityje taikant panašų gydymo būdą su donoro ląstelėmis.

Darbe analizuota serumo baltymų įtaka KT ir Ce6 komplekso stabilumui bei singuletinio deguonies generacijai. Kitos studijos, analizuojančios KT-Ce6 komplekso savybes, tiria kompleksą tik buferiniuose tirpaluose be baltymų, pavyzdžiui, DPBS. Mūsų tyrimuose buvo parodyta, kad serumo baltymai „ištraukia“ Ce6 iš KT amfifilinio polimero, todėl suprastėja singuletinio deguonies generacija ir PDT efektyvumas. Darbe pirmą kartą parodyta, kad MKL padeda apsaugoti KT-Ce6 kompleksą nuo destabilizacijos. Mūsų žiniomis, esame pirmieji, ištyrę fotosensibilizatoriaus kompleksaciją su amfifiliniu polimeru dengtais skirtingo krūvio KT ir tokių kompleksų fotodinaminius efektus.

Literatūroje galima rasti tyrimų su KT-Ce6 kompleksu, tačiau pirmą kartą jo efektyvumas buvo parodytas ne vien *in vitro* modelinėje sistemoje, bet ir gyvame organizme.

Praktinė reikšmė

MKL, kaip teranostinių nanodalelių nešiklių, potencialas ateityje turi būti patikrintas didesnės apimties laboratorinių gyvūnų eksperimentuose, kad tyrimus būtų galima saugiai perkelti į I-II fazės klinikines studijas. Su MKL, transportuojančiomis vaistus, atliktų klinikinių tyrimų skaičius vis dar yra menkas. Klinikinių tyrimų registre *clinicaltrials.gov* registruoti vos keturi tyrimai su MKL, kurios transportuoja interferoną β arba onkolitinius virusus. Norint šią sistemą pilnai taikyti onkologinėmis ligomis sergančių pacientų gydymui, reikia išsamesnio efekto patikrinimo bei palyginimo tarp MKL, gautų iš skirtingų šaltinių. Taip pat, siekiant personalizuoti gydymą, svarbu įvertinti terapijos tinkamumą skirtingos lokalizacijos navikams.

Iš sunkiųjų metalų pagaminti kvantiniai taškai dėl lėtinio toksinio poveikio rizikos gali būti netinkami šios gydymo strategijos perkėlimui į kliniką. Tačiau šiame etape šios nanodalelės puikiai tinka kaip modelinė sistema, vertinant MKL specifinio transportavimo potencialą *in vitro* bei *in vivo* navikų modeliuose. Dar didesnę praktinę reikšmę tyrimai įgis ateityje sukūrus kvantinių taškų fizikocheminėms savybėms prilygstančias biodegraduojančias ar lengvai iš organizmo pašalinamas nanodaleles. KT-Ce6 kompleksas, sužadinamas UV-Vis spektriniame diapazone, taip pat gali būti sunkiau pritaikomas standartinėje klinikinėje diagnostikoje, ypač gilesniuose audiniuose esančių navikų vaizdinimui bei gydymui. Tačiau mūsų tyrimuose gautas diagnostinis efektas būtų tinkamas norint nustatyti naviko ribas ar išplitimą chirurginių operacijų metu, taip pat pastebėti galimą vėžinių ląstelių infiltraciją į sarginius limfmazgius ar aplinkinius organus. Taip pat, šiuolaikinės šviesolaidinės sistemos ir endoskopinės technologijos leidžia PDT naudoti su endoskopinėmis, laparoskopinėmis ar intraoperacinėmis šviesos sistemomis. Norint pagerinti skvarbą pro audinius ir terapijos efektyvumą, KT-Ce6 kompleksui sužadinti galima naudoti daugiafotonį sužadinimą. Pagrindinis jo pranašumas yra infraraudonosios spinduliuotės, kurią audiniai sugeria mažiau, naudojimas, todėl žadinanti spinduliuotė gali prasiskverbti į gilesnius audinių sluoksnius. Daugiafotonis sužadinimas ar nanodalelių, sužadinamų artimąją infraraudonąją spinduliuote, naudojimas yra būsimos tokių tyrimų ir klinikinio pritaikymo kryptys.

1. METODAI

1.1. Kvantinių taškų ir jų kompleksų fizikocheminių savybių charakterizavimas

1.1.1. Kvantiniai taškai

Visuose tyrimuose naudoti CdSe/ZnS KT, bet skyrėsi jų PL smailių vertės ir dangalai. Pirminiuose tyrimuose, kuriuose atrinkti teranostiniam kompleksui formuoti tinkamiausi KT, buvo naudoti keturių tipų CdSe/ZnS KT – dengti fosfolipidais su PEG molekulėmis ir turintys amino arba karboksilo funkcines grupes (iš eBioscience Inc.) arba padengti amfifiliniu polimeru ir turintys PEG-amino arba karboksilo funkcines grupes (iš Invitrogen Corp.) (visų PL λ_{max} = 605 nm).

Tolimesniuose tyrimuose naudoti dviejų tipų KT, kurie atrinkti kaip tinkamiausi kompleksacijai su Ce6, t.y. amfifiliniu polimeru dengti ir karboksilo grupėmis funkcionalizuoti KT, kurių λ_{max} = 655 nm (Qdot® 655 ITK™) ir λ_{max} = 625 nm (Qdot® 625 ITK™) (abu iš Invitrogen Corp.). PL bangos ilgis buvo vienintelis skirtumas tarp naudotų KT, nes jų dydis nesiskyrė – Qdot® 655 ITK™ hidrodinaminis diametras yra 14,55 nm (Xu ir kt., 2016), o Qdot® 625 ITK™ atomo jėgos mikroskopu (AFM) ir dinaminės šviesos sklaidos (DLS) metodu gautas nanodalelių dydis ~14,5 nm (Pav. 1.1) (Dapkute ir kt., 2017).

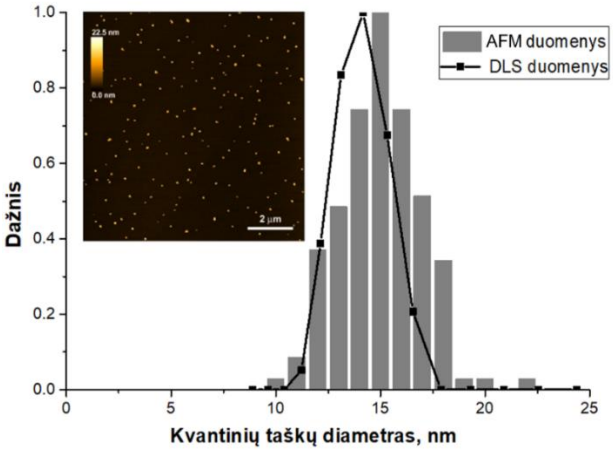

Pav. 1.1. Kvantinių taškų dydžio nustatymas AFM ir DLS metodais. Nuotraukoje – nanodalelių žėručio paviršiuje AFM mikrografija. Pagal Dapkute ir kt., 2017.

1.1.2. Kvantinių taškų ir chlorino e6 komplekso formavimas

KT-Ce6 kompleksas suformuotas kaip aprašyta Skripka ir kt., 2018 ir Dapkute ir kt., 2021. Ce6 buvo įsigytas iš Frontier Scientific Inc. Pradinis tirpalas paruoštas ištirpinant nedidelį kiekį Ce6 miltelių 0,2 M NaOH tirpale ir praskiedžiant fosfatiniame buferyje (PB) (pH 7). Tiksli tirpalo koncentracija apskaičiuota pagal Lamberto-Bugerio-Bero dėsnį:

$$A = \varepsilon \times c \times l \quad (1)$$

kur A yra sugertis ties 405 nm, ε – Ce6 molinės ekstinkcijos koeficientas ties 405 nm (175 000 $M^{-1}cm^{-1}$), c – Ce6 koncentracija, l – optinio kelio ilgis (kiuvetės storis) (1 cm).

KT-Ce6 kompleksas gaunamas įpilant 0,005 μM KT į Ce6 tirpalą (koncentracijos nuo 0,0005 μM iki 4 μM) ir laikant kambario temperatūroje.

Ląsteliniams tyrimams naudotas spektriniais matavimais atrinktas 1:100 KT ir Ce6 santykis ir 4 valandų kompleksacijos trukmė, bet koncentracijos padidintos 3,2 karto, nes atlikti tyrimai parodė, kad didžiausia netoksiška KT koncentracija yra 16 nM (Dapkute ir kt., 2017; Saulite ir kt., 2017). Atitinkami KT (0,016 μM) ir Ce6 (1,6 μM) tirpalai naudoti kaip kontrolės.

1.1.3. Fizikocheminių savybių nustatymas

Spektroskopiniai matavimai buvo atlikti su KT-Ce6 tirpalais, kurių molinis santykis buvo nuo 1:0,1 iki 1:800, įvairiais laiko momentais. KT-Ce6 komplekso stabilumas įvertintas skirtinguose tirpaluose (PBS, DMEM ir DMEM su FBS). Tirpalų sugerties, PL ir fluorescencijos gesimo kinetikos matavimai detaliai aprašyti Skripka ir kt., 2018 ir Dapkute ir kt., 2021.

KT ir KT-Ce6 komplekso hidrodinaminis skersmuo išmatuotas DLS metodu. Dalelių hidrodinaminis dydis ir zeta potencialas ζ nustatyti Brookhaven ZetaPALS matuokliu (Brookhaven Instruments).

1.1.4. Singuletinio deguonies generacijos įvertinimas

Po švitinimo 470 nm bangos ilgiu susidaręs singuletinis deguonis nustatytas naudojant SOSG (Thermo Fisher Scientific). Ce6, KT ar KT-Ce6 kompleksas PBS, DMEM ar DMEM su FBS tirpaluose buvo sumaišyti su SOSG vandeniniu tirpalu. Švitinimas atliekamas su 470 ± 5 nm bangos ilgio

šviesa naudojant MAX-302 ksenono lempą (Asahi Spectra Co., Ltd) surenkant vienkartinę 17,7 J/cm^2 dozę. Švitinimo laikas dozei buvo apskaičiuojamas pagal formulę:

$$t = D \times S/P \quad (2)$$

kur t yra laikas (s), D – dozė (17,7 J/cm^2), S – plotas (cm^2), P – šviesos galia (W), kuri matuojama kaskart prieš švitinimą galios matuokliu.

Rezultatai pateikti kaip fluorescencijos intensyvumo skirtumas ties SOSG emisijos smaile (525 nm) prieš ir po švitinimo (Dapkute ir kt., 2021).

1.2. Ląstelių tyrimai

1.2.1. Odos MKL išskyrimas, kultivavimas

Tyrimuose naudotos pirminės žmogaus odos MKL. Ląstelės buvo išskiriamos iš perteklinės vokų odos, likusios atliekant blefaroplastiką Vilniaus miesto klinikinėje ligoninėje. Tyrimą patvirtino ir leidimą atlikti biomedicininį tyrimą suteikė Vilniaus regioninis biomedicininių tyrimų etikos komitetas (leidimo Nr. 158200-18 / 6-1036-548), pacientai pasirašė informuoto asmens sutikimo formą. Ląstelės buvo išskirtos remiantis eksplantų kultūros metodu, kaip aprašyta Dapkute ir kt., 2021. Pirmosios ląstelės, išaugančios iš eksplantų, vizualiai matomos po 3-5 dienų. MKL kultivuojamos DMEM, papildytu F12 maistinių medžiagų mišiniu (DMEM/F12, 3:1 v/v), 10% FBS ir 1% P/S (visi iš Gibco) plastikiniuose ląstelių kultivavimo induose be papildomo paviršiaus padengimo. Tyrimuose naudota beseruminė terpė buvo sudaryta iš DMEM/F12 (3:1 v/v) ir 1% P/S. Norint panaikinti nuo donoro priklausomus nuokrypius, eksperimentai buvo pakartoti su mažiausiai trimis skirtingais donorais.

1.2.2. MKL identifikavimas

Išskirtos MKL buvo įvertintos pagal morfologiją, imunofenotipą ir diferenciacijos potencialą. Imunofenotipas buvo nustatytas kaip aprašyta Dapkute ir kt., 2017 ir Dapkute ir kt., 2021. Naudoti šie monokloniniai pelės antikūnai prieš žmogaus antigenus: CD90, konjuguotas su FITC, CD184 (CXCR4), konjuguotas su PE (abu iš BD Biosciences), CD44-FITC (Thermo Fisher Scientific), CD73-FITC, CD105-PE, CD45-FITC, CD34, konjuguotas su APC, CD14-PE (visi penki iš eBioscience). Nudažytos ląstelės buvo analizuojamos tėkmės citometru Accuri C6 (Accuri Cytometers, Inc.)

surenkant bent 1×10^4 gyvybingų ląstelių. Duomenys apdoroti FlowJo (Tree Star, Inc.) ir Accuri C6 programomis (Accuri Cytometers, Inc.).

Diferenciacijos potencialui nustatyti monosluoksniu augančios MKL buvo paveiktos StemPro™ (Gibco) adipogeninės ar osteogeninės diferenciacijos terpe, keičiant terpę kas 3-4 dienas, o chondrogeninė diferenciacija atlikta 15 ml konusiniuose mėgintuvėliuose MKL nucentrifuguojant 200 ×g 7 min ir paveikiant StemPro™ chondrogenine terpe. Ląstelės buvo auginamos diferenciacijos terpėse iki 21 dienos. Diferencijuotos ląstelės buvo fiksuojamos 10% neutraliu buferiniu formalinu. Adipogeniniai mėginiai buvo įvertinti pagal Oil Red O (žymi lipidus), osteogeninė diferenciacija patvirtinta Alizarin Red dažu (žymi kalcio sankaupas), o chondrogeninė diferenciacija parodyta ląstelių darinį supjausčius kriomikrotomu ir pjūvius nudažius toluidino mėliu (žymi proteoglikanus) (dažai įsigyti iš Sigma Aldrich) (Dapkute ir kt., 2021).

1.2.3. Ląstelių linijų kultivavimas

Tyrimuose naudotos ląstelių linijos: žmogaus krūties vėžio MDA-MB-231 (ATCC HTB-26 ™), žmogaus krūties epitelio MCF-10A (ATCC CRL-10317 ™), pelės plaučių karcinomos LLC1 (ATCC CRL-1642 ™) (visos įsigytos iš Amerikos kultūrų tipo kolekcijos (ATCC)), žmogaus krūties vėžio MCF-7 (ECACC 86012803) (iš Europos autentiškų ląstelių kultūrų kolekcijos (ECACC)).

MDA-MB-231, MCF-7 ir LLC linijos buvo kultivuojamos DMEM, papildytame 10% FBS ir 1% P/S. MCF-10A buvo kultivuojamos žmogaus krūties epitelio ląstelių (angl. *human mammary epithelial cells*, HuMEC) bazinėje beseruminėje terpėje, papildytoje 1% HuMEC papildu, 0,4% jaučio hipofizės ekstraktu (visi iš Thermo Fisher Scientific) ir 1% P/S. Ląstelės buvo kultivuojamos inkubatoriuje 37 °C temperatūroje su 5% CO_2 iki 90 % konfluencijos.

1.2.4. Nanodalelių kaupimosi ir pasiskirstymo ląstelėse tyrimai

Didžiausia netoksiška KT koncentracija buvo nustatyta standartiniu LDH citotoksiškumo testu (CytoTox 96®, Promega) ir detaliai aprašyta Dapkute ir kt., 2017.

Nanodalelių detekcijai konfokalinės mikroskopijos būdu vėžinės ląstelės arba MKL užsėjamos vaizdinimui tinkamose plokštelėse ir inkubuojant su KT arba KT-Ce6 kompleksu seruminėje/beseruminėje terpėje atitinkamą laiką.

Ląstelės buvo papildomai dažomos branduolių dažu Hoechst 33342 (Sigma Aldrich), o PFA fiksuotose ląstelėse buvo papildomai dažomas citoskeletas (f-aktinas) su Alexa Fluor® 488 Phalloidin (Thermo Fisher Scientific). Norint detaliai nustatyti nanodalelių viduląstelinę lokalizaciją buvo pažymėtos ankstyvosios ir vėlyvosios endosomos bei lizosomos atliekant laikinąją ląstelių transfekciją su Cell Light® Reagent-GFP, BacMam 2.0 reagentais (Thermo Fisher Scientific). Ankstyvosioms endosomoms pažymėti naudota BacMam 2.0 sistema Rab5a baltymui, vėlyvosioms endosomoms – Rab7a baltymui, o lizosomoms – Lamp1 baltymui (Saulite ir kt., 2017). KT ir KT-Ce6 komplekso vaizdinimo tyrimai yra vienas iš pagrindinių metodų, todėl aprašytas detaliai šiuose šaltiniuose: Dapkute ir kt., 2017; Jarockyte ir kt., 2018; Saulite ir kt., 2018; Saulite ir kt., 2017; Skripka ir kt., 2018; Dapkute ir kt., 2021.

Nanodalelių kiekybinis susikaupimas 2D ląstelių monosluoksniuose ir 3D ląsteliniuose sferoiduose išmatuotas BD Accuri C6 tėkmės citometru (Dapkute ir kt., 2017; Jarockyte ir kt., 2018; Dapkute ir kt., 2021). Surenkama bent 1×10^4 gyvybingų ląstelių iš 2D ląstelių kultūros ir bent 5×10^3 iš 3D ląstelių kultūros. Duomenys apdoroti FlowJo ir Accuri C6 programomis. 3D sferoidai formuojami kabančio lašo metodu ir matuojami kaip aprašyta Jarockyte ir kt., 2018.

1.2.5. MKL migracijos tyrimai

MKL tropizmas įvertintas Transwell® įdėklais (*insertais*) su polikarbonatine membrana ir 8 μm poromis (Corning Inc). Apatinėje plokštelės dalyje buvo: vėžinių MDA-MB-231 arba nevėžinių MCF-10A ląstelių monosluoksniai beseruminėje terpėje, taip pat pro 0,22 μm filtrą filtruota beseruminė augimo terpė, nusiurbta nuo MDA-MB-231 ląstelių, MKL augimo terpė su 20% FBS (teigiama kontrolė) ir beseruminė terpė (neigiama kontrolė). Į įdėklus (*insertus*) patalpinamos MKL su/be KT. Po 24 valandų numigravusios ląstelės buvo užfiksuotos 4% PFA ir nudažytos Hoechst dažu (Pav. 1.2). Ląstelės vaizdintos konfokaliniu mikroskopu ir skaičiuotos ne mažiau nei 5 skirtinguose laukuose. Duomenys sunormuoti į teigiamą kontrolę ir pateikti kaip vidurkis ± SD (Dapkute ir kt., 2017).

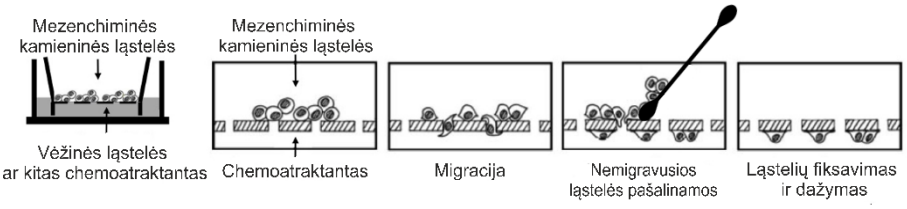

Pav. 1.2. *In vitro* migracijos schematinis atvaizdavimas. Pagal Ladewig ir kt., 2015.

1.2.6. Fotodinaminės terapijos (PDT) tyrimai

Ląstelės (MDA-MB-231, MKL arba jų kokultūros santykiu 1:2), augančios vaizdinimui pritaikytose plokštelėse, buvo paveikiamos KT-Ce6 kompleksu 6 valandas ir švitinamos mėlyna šviesa ($\lambda_{žad}$ = 470 ± 5 nm) surenkant vienkartinę 17,7 J/cm^2 dozę kiekviename šulinėlyje. Šviesa fokusuojama tik į vieną šulinėlį vienu metu. Tamsinio poveikio plokštelė laikoma tokiomis pačiomis sąlygomis šalia, tik apsaugota nuo šviesos poveikio. Po švitinimo ląstelės grąžinamos į inkubatorių. Ląstelių kokultūros švitinamos du kartus kas 24 valandas.

Praėjus ≥16 valandų po paskutinio švitinimo ląstelės dažomos LIVE/DEAD gyvybingumo dažais (Thermo Fisher Scientific) – gyvos ląstelės nudažomos kalceinu (žaliai), o žuvusios – etidžio homodimeru (EthD-1) (raudonai). Ląstelės vaizdinamos lazeriniu skenuojančiu konfokaliniu mikroskopu Nikon Eclipse TE2000-S, C1 Plus (Nikon). PDT tyrimai detaliai aprašyti Skripka ir kt., 2018 ir Dapkute ir kt., 2021.

KT-Ce6 komplekso tamsinio toksiškumo ir fotodinaminio efekto kiekybinis įvertinimas atliktas naudojant XTT ląstelių gyvybingumo, išreikšto per metabolinį aktyvumą, testą (Biological Industries), kuris plačiau aprašytas Dapkute ir kt., 2021.

1.2.7. Konfokalinė mikroskopija ir FLIM

KT ir KT-Ce6 komplekso viduląstelinė lokalizacija ir PDT efektas nustatyti lazeriniu skenuojančiu konfokaliniu mikroskopu Nikon Eclipse TE2000-S, C1 Plus (Nikon, Japan), naudojant 60× NA1.4 imersinį objektyvą arba 20× NA 0.5 sausą objektyvą ir EZ-C1 v3.90 programą. Diodinis lazeris (404 nm) naudotas sužadinti Hoechst 33342, argono jonų lazeris (488 nm) – GFP, Alexa Fluor 488® Phalloidin, kalceinui, EthD-1, o helio-neono lazeris (543 nm) – KT ir KT-Ce6 kompleksui.

Konfokalinio mikroskopo sistema papildomai turi integruotą spektrometrą (Ocean Optics), todėl galima atlikti detalius fluorescencinės spektroskopijos matavimus *in vitro*. Fluorescencijos gyvavimo trukmės mikroskopija (FLIM) atlikta naudojant Lifetime ir FCS papildymą Nikon C1si mikroskopui (PicoQuant GmbH). Vaizdinimo sistema sudaryta iš impulsinio diodinio lazerio (405 nm) ir laike koreliuotų pavienių fotonų skaičiavimo detektorių (TCSPC) (PicoHarp 300, PicoQuant GmbH). Konfokalinės mikrokospijos ir FLIM metodikos plačiau aprašytos Dapkute ir kt., 2021.

Nuotraukos apdorotos EZ-C1 Bronze v3.80 (Nikon) and ImageJ 1.48 (National Institute of Health) programomis. FLIM histogramos gautos su SymPhoTime 64 v.2.4.4874 (PicoQuant GmbH) programa.

1.3. Tyrimai su laboratoriniais gyvūnais

Visų tyrimų su gyvūnais protokolai buvo patvirtinti Valstybinės maisto ir veterinarijos tarnybos (leidimo Nr. G2-29), eksperimentai atliekami laikantis Europos sąjungos 2010/63/EU Direktyvos reguliacijų. Tyrimai atlikti su CB17 SCID imunodeficitinėmis pelėmis (Taconic Biosciences) ir C57BL/6 linijos pelėmis (Valstybinis mokslinių tyrimų institutas Inovatyvios medicinos centras), kaip aprašyta Dapkute ir kt., 2017; Jarockyte ir kt., 2018; Dapkute ir kt., 2021. Pelės laikomos pastovioje 22 °C ± 1 °C temperatūroje ir 55 % ± 10 % drėgmėje su 12 val. šviesos/tamsos fotoperiodu, maitinami standartizuotu pašaru ir vandeniu *ad libitum*. Prieš kiekvieną eksperimentą gyvūnai aklimatizuojami 7 dienas.

Navikų sukėlimui CB17 imunodeficitinėms pelėms į riebalinį audinį aplink spenelį suleistos žmogaus vėžinės ląstelės MDA-MB-231 arba MCF-7, o C57BL/6 linijos pelėms – po oda suleidžiant iš C57BL/6 linijos kilusias LLC vėžines ląsteles.

Navikams susiformavus, CB17 imunodeficitinėms pelėms injekcija į naviko centrą suleidžiami kvantiniai taškai intranavikiniam pasiskirstymui ištirti. *In vivo* vaizdinimas atliktas su neinvazine smulkių gyvūnų vaizdinimo sistema UVP iBox Scientia-800 (Ultra-Violet Products). Prieš vaizdinimą ir vaizdinimo metu pelės yra anestezuojamos sevoflurano dujomis, šildantis kilimėlis naudotas vengiant hipotermijos. Pelės eutanazuojamos cervikaline dislokacija po 24 valandų. Navikas išpjaunamas ir analizuojamas po UV lempa *ex vivo*. Vėliau navikas supjaustomas kriomikrotomu ir analizuojamas konfokaliniu mikroskopu. Navikai taip pat mechaniškai ir fermentų pagalba

homogenizuojami, suspensija matuojama tėkmės citometru Accuri C6 (Jarockyte ir kt., 2018).

In vivo migracijos tyrimuose CB17 imunodeficitinėms pelėms ir C57BL/6 pelėms ~10 mm žemiau naviko po oda suleidžiama atitinkamai 5×10^5 MKL ląstelių su KT arba 1×10^6 KT-Ce6 kompleksu viduje (nanodalelių inkubacija atliekama beseruminėje terpėje). Norint ištirti *in vivo* MKL migraciją, pelės laikomos 1 arba 7 dienas. Po atitinkamo laiko pelės eutanazuojamos, navikas ir pagrindiniai organai išimami ir stebimi po UV lempa *ex vivo*, vėliau supjaustomi kriomikrotomu ir analizuojami konfokaliniu mikroskopu arba tėkmės citometru, papildomai dažant su anti-CD44-FITC antikūnu (Dapkute ir kt., 2017, Dapkute ir kt., 2021).

Norint ištirti PDT efektą *in vivo*, praėjus 24 val. po 1×10^6 MKL (tuščios, beseruminėje terpėje inkubuotos su KT, su Ce6 arba su KT-Ce6) suleidimo ~10 mm žemiau naviko po oda, pelės du kartus kas 24 valandas švitinamos 470 nm bangos ilgio šviesa su kasdiene 60 J/cm^2 doze, surenkant suminę 120 J/cm^2 dozę. Navikų dydis sekamas kas 2-4 dienas matuojant slankmačiu. Dalis pelių eutanazuojamos ir tiriamos po 10 dienų vertinant jų navikų dydžius ir metastazės plaučiuose, kitos pelės paliekamos naviko augimo kinetikai ir išgyvenamumui sekti (Dapkute ir kt., 2021).

1.4. Statistinė analizė

Visi eksperimentai buvo pakartoti mažiausiai 3 kartus, jei neapibrėžta kitaip. Duomenys pateikti kaip vidurkiai su standartiniu nuokrypiu. Statistinė analizė atlikta naudojant Stjudento t-testą. Statistiškai reikšmingais rezultatai buvo laikyti, kai $p \leq 0,05$.

2. REZULTATAI IR JŲ APTARIMAS

Šioje dalyje aptariami svarbiausi rezultatai, pateikti su disertacijos tema susijusiose publikacijose, dėmesį kreipiant į teranostinio nanokomplekso veikimą, MKL savybes ir potencialų ląstelių terapijos ir nanotechnologijų kombinavimą vėžinių susirgimų gydymui.

2.1. Nespecifinis nanodalelių kaupimasis 3D sferoiduose ir navikuose

Nepaisant to, kad nanodalelės turi daugybę galimų vėžio diagnostikos ir gydymo pritaikymų, jų panaudojimą riboja tam tikri iššūkiai. Prieš patekdamos į vėžines ląsteles, nanodalelės sąveikauja su sudėtinga žmogaus kraujo aplinka, iš kurios yra greitai pašalinamos mononuklearinės fagocitų sistemos. Be to, nepaisant EPR efekto, nanodalelėms trūksta specifiškumo, ypač mažesnių navikų, kurių kraujagyslės dar nėra išsivysčiusios, atveju. Šiuo metu net diskutuojama, kad EPR efektas, paremtas tarpais tarp naviko kraujagyslių endotelio ląstelių ir prasto limfos nutekėjimo, neatlieka tokios svarbios funkcijos nanodalelių patekime į navikus kaip spekuliuota anksčiau – neseniai Sindhwani su bendraautoriais ištyrė, kad 97 % nanodalelių į navikus patenka dėl aktyvios transcitozės, vykstančios endotelio ląstelėse, o ne dėl EPR efekto (Sindhwani ir kt., 2020).

Jarockyte ir kt. buvo parodyta, kad ne visuomet rezultatai, gaunami *in vitro* modelinėje sistemoje, atitinka realią situaciją navike (Jarockyte ir kt., 2018). Naudodami *in vitro* vėžinių ląstelių 2D monosluoksnių ir 3D sferoidų modelius bei *in vivo* ksenograftinius navikus nustatėme, kad nors 2D monosluoksnyje beveik visos ląstelės sukaupia KT, 3D sferoiduose nanodaleles sukaupusių ląstelių yra tik 60-70 %, priklausomai nuo ląstelių tipo. Nanodalelių susikaupimas navikuose po intranavikinės injekcijos yra dar mažesnis ir gali siekti vos <10 % (Pav. 2.1A). Detaliau panagrinėjus susikaupimo tendencijas matyti, kad ir 3D modelinėje sistemoje, ir navike nanodalelių susikaupimas yra heterogeniškas – KT kaupiasi 3D sferoido ar naviko periferijoje kelių ląstelių storio sluoksnyje, bet į centrinę dalį beveik neprasiskverbia (Pav. 2.1B-C) (Jarockyte ir kt., 2018).

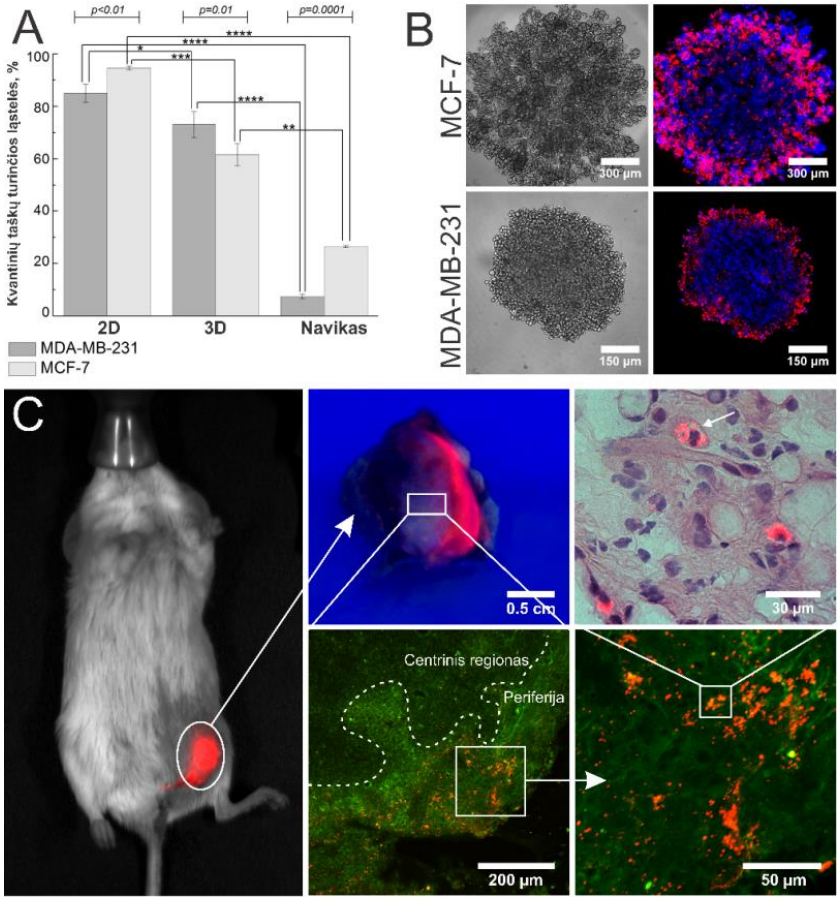

Pav. 2.1. Kvantinių taškų kaupimosi 2D monosluoksniuose, 3D sferoiduose ir navikuose *in vivo* palyginimas. A – kiekybinis susikaupimas, matuotas tėkmės citometrijos būdu; * rodo statistiškai reikšmingus skirtumus tarp grupių. B – susikaupimas 3D sferoiduose, suformuotuose iš MCF-7 ir MDA-MB-231 vėžinių ląstelių. C – susikaupimas navike (gyvūno optinis vaizdinimas UVP Ibox Scientia-800 kamera; makroskopinis išpreparuoto naviko vaizdas po UV lempa; konfokaliniai kriomikrotomu pjaustyto naviko vaizdai). Pagal Jarockyte ir kt., 2018.

Apibendrinant, nanodalelių pasyvus susikaupimas ir pasiskirstymas navike yra minimalus. Verta atsižvelgti į tai, kad tyrimai atlikti taikant tiesioginę intranavikinę injekciją. Toks injekcijos būdas klinikinėje praktikoje taikomas rečiau nei intraveninis ar peroralinis pateikimas dėl metastazių išsėjimo pavojaus (Shyamala ir kt., 2014). Remiantis Dai ir kt. skaičiavimais, kad vos

0,0014 % sistemiškai pateiktų nanodalelių sąveikauja su vėžinėmis ląstelėmis (Dai ir kt., 2018), galime prognozuoti, jog intraveninės injekcijos metu nanodalelių susikaupimas būtų dar mažesnis nei gautas mūsų tyrimų metu. Aktyvus nanodalelių pristatymas naudojant taikinines molekules, tokias kaip aptamerai, antikūnai ar įvairūs ligandai, neužtikrina selektyvumo dėl navikui unikalių žymenų trūkumo, o tikslą atpažįstančios biomolekulės ant nanodalelės paviršiaus yra greitai paslepiamos po serumo baltymais, blokuojančiais atpažinimą (Xiao ir Gao, 2018).

Ferreira su bendraautoriais parodė, kad MKL prasiskverbia į iš įvairių ląstelių tipų suformuotą 3D sferoidų centrą vos per 24 valandas (Ferreira ir kt., 2018). Tai pateikia svarius argumentus tolesniems tyrimams ir naujų terapinių metodų, kurių pagrindas yra teranostinių nanodalelių pristatymas į navikus mezenchiminėmis kamieninėmis ląstelėmis, kūrimui.

2.2. Kvantinio taško ir chlorino e6 komplekso formavimas, charakterizavimas ir nanodalelės dangalo svarba

Norėdami nustatyti, kuris KT dangalo tipas yra tinkamiausias kompleksacijai su chlorinu e6, ištyrėme keturių skirtingų tipų nanodaleles – fosfolipidais ar amfifiliniu polimeru dengtus kvantinius taškus su amino arba karboksilo funkcinėmis grupėmis.

Visi tyrimai su KT-Ce6 kompleksu atliekami žadinant arba švitinant 470 nm bangos ilgiu. Toks bangos ilgis pasirinktas neatsitiktinai – jį gerai sugeria visi naudoti KT, bet Ce6 sugertis šioje spektro dalyje yra minimali (Skripka ir kt., 2018, Dapkute ir kt., 2021). Tokiu būdu komplekse yra sužadinami tik KT, o Ce6 fluorescencija, singuletinio deguonies generacija ir PDT efektas yra nulemti FRET tarp KT ir Ce6.

Nepriklausomai nuo dangalo ir jo krūvio, komplekso formavimasis prasideda iš karto po Ce6 pridėjimo į KT tirpalą ir tęsiasi apie 4 valandas, kol pasiekiama pusiausvyra (Dapkute ir kt., 2021). Hidrofobinė sąveika tarp PS ir nanodalelės įveikia galimą elektrostatinio atstūmimo barjerą, nes kompleksas sėkmingai formuojasi net ir esant neigiamam KT krūviui ir neigiamam Ce6 (Skripka ir kt., 2018). Nors KT hidrodinaminis skersmuo po Ce6 pridėjimo keičiasi nedaug (D_h (KT) = 14 nm, D_h (KT-Ce6 kompleksas) = 14,2 nm (Dapkute ir kt., 2021), KT-Ce6 komplekso susiformavimas matomas pagal kelis požymius. Pirma, KT fotoliuminescencijos intensyvumas sumažėja, nes dalis sužadinimo energijos perduodama prisijungusiam Ce6. Antra, nors fotosensibilizatorius 470 nm šviesą sugeria prastai, ženkliai išauga Ce6

fluorescencija, o fluorescencijos maksimumas pasislenka nuo 660 nm iki 672-674 nm (Pav. 2.2A) dėl pasikeitusios PS aplinkos ir sąveikos su KT fosfolipidinėmis ar amfifilinėmis molekulėmis. Galiausiai kompleksas charakterizuojamas pagal FRET – komplekse esančio KT fluorescencijos gyvavimo trukmė sutrumpėja dėl atsiradusių energijos nuostolių (KT <τ> yra 35,7 ns, o KT-Ce6 komplekso – 14,5 ns) (Pav. 2.2B) (Skripka ir kt., 2018; Dapkute ir kt., 2021).

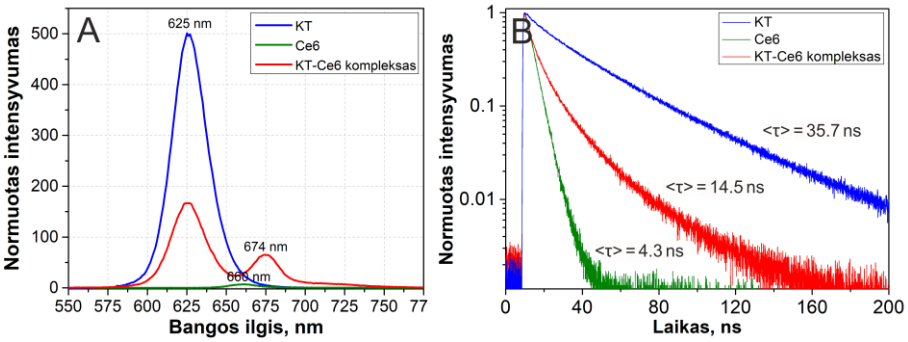

Pav. 2.2. KT-Ce6 komplekso fizikinės charakteristikos. A – Normuoti KT, Ce6 ir KT-Ce6 komplekso fotoliuminescencijos spektrai ($\lambda_{žad.}$ = 470 nm). B – Normuotos KT, Ce6 ir KT-Ce6 komplekso fluorescencijos gesimo kinetikos, matuotos ties jų atitinkamais fluorescencijos maksimumais ($\lambda_{žad.}$ = 405 nm). Pagal Dapkute ir kt., 2021.

Tolimesni skirtingų dangalų KT-Ce6 kompleksų *in vitro* tyrimai parodė, kad MDA-MB-231 krūties vėžio linijos ląstelėse geriausiai kaupiasi ir didžiausią PDT efektyvumą turi būtent amfifiliniu polimeru dengti ir karboksilo grupėmis funkcionalizuoti KT ir jų atitinkamas kompleksas (Pav. 2.3), todėl jie buvo pasirinkti tolimesnėms studijoms su MKL (Skripka ir kt., 2018). Papildomai buvo ištirta, kad prie tokio tipo vieno KT galima prijungti iki 100 molekulių Ce6, taip maksimaliai padidinant PDT efektyvumą (Dapkute ir kt., 2021). KT-Ce6 kompleksas buvo inkubuotas terpėje be baltymų ir aplink nanodalelę nesusiformavo baltymų korona, todėl galime spręsti, kad KT-Ce6 komplekso paviršiaus chemija padarė didelę įtaką ląsteliniam susikaupimui. Kiti autoriai taip pat yra pastebėję, kad neigiami įkrautos nanodalelės geriau patenka į ląsteles (Ryman-Rasmussen ir kt., 2007).

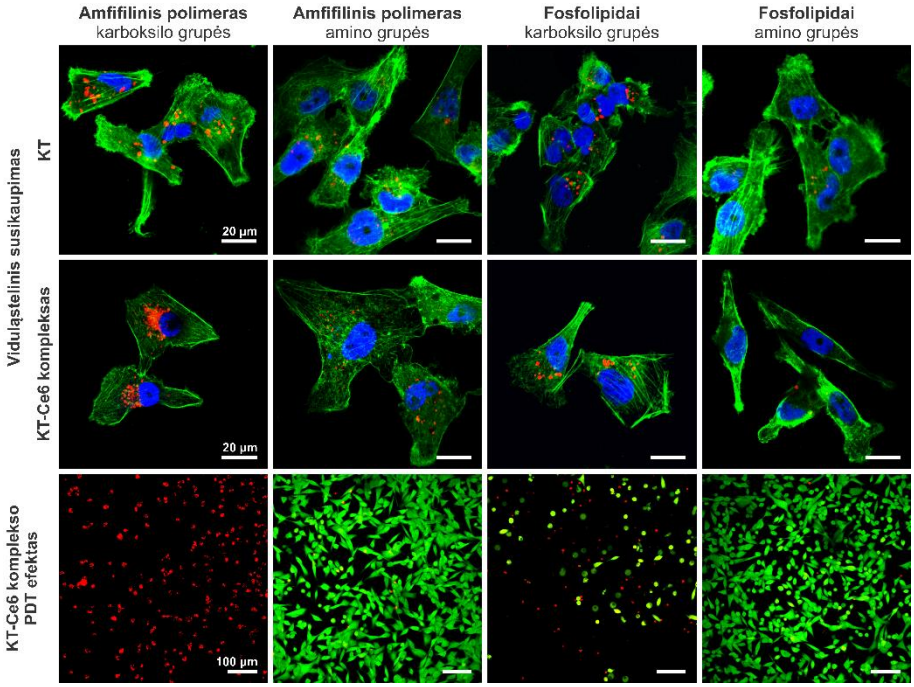

Pav. 2.3. Skirtingo tipo KT ir KT-Ce6 kompleksų viduląstelinis susikaupimas MDA-MB-231 ląstelėse ir PDT efektas po švitinimo 470 nm bangos ilgiu surenkant 17,7 J/cm^2 dozę. Viduląstelinio susikaupimo atveju raudona – KT arba KT-Ce6 kompleksas, žalia – aktino filamentai, mėlyna – branduoliai. PDT efekto atveju žalia – gyvos ląstelės (kalceinas), raudona – negyvos ląstelės (EthD-1). Pagal Skripka ir kt., 2018.

Taigi, sąveika tarp KT ir Ce6 įvyksta greitai ir turi charakteringus požymius, o efektyviausiai veikia KT-Ce6 kompleksas, sudarytas iš KT, padengtų amfifiliniu polimeru ir funkcionalizuotų neigiamo krūvio karboksilo grupėmis. Toks kompleksas geriausiai kaupiasi ląstelėse ir turi didžiausią PDT efektą.

Nemažai diskusijų kyla dėl galimo iš sunkiųjų metalų sudarytų KT toksiškumo. Vis dėlto, tyrimai su smulkiais gyvūnais ir net primatais parodė, kad jei kadmio ar švino turintis branduolys yra padengiamas stabilizuojančiu ir nuo degradacijos apsaugančiu apvalkalu bei biosuderinamumą ir tirpumą vandenyje didinančiu dangalu, nėra sukeliami rimti fiziologiniai nukrypimai nuo normos (Ye ir kt., 2019; Yong ir kt., 2013). Šiuo metu KT su sunkiųjų metalų branduoliu vis dar yra geriausias pasirinkimas iš visų nanodalelių

pagal fotoliuminescencines savybes. Mūsų darbai su KT ir KT-Ce6 kompleksu nėra apriboti nanodalelių tipu, tai reiškia, kad KT gali būti pakeisti kita, mažesnę toksiškumo riziką keliančia nanodalele, kuri yra panašaus dydžio, spektrinių savybių ir padengta amfifiliniu polimeru.

2.3. KT-Ce6 komplekso stabilumo ir singuletinio deguonies generacijos tyrimai

Susiformavęs kompleksas išlaiko savo *zeta* potencialą (ζ_{KT} = -24,3±1 mV, $\zeta_{KT\text{-}Ce6}$ = -25,3±0,6 mV), todėl išlieka koloidiškai stabilus ir neagreguoja visą 96 valandų matavimo laiką (Dapkute ir kt., 2021). Vis dėlto, KT-Ce6 kompleksas yra lengvai destabilizuojamas serumo baltymais. Nors ląstelių mitybinėje terpėje, į kurią nėra papildomai pridėta baltymų, komplekso intensyvumas šiek tiek sumažėja, spektrinės tendencijos bei charakteringos spektrų viršūnės lieka tos pačios (Pav. 2.4C). Tačiau į mitybinę terpę pridėjus jaučio serumo baltymų (FBS), intensyvumas ties KT λ_{max} išauga, viršūnės ties 674 nm intensyvumas stipriai sumažėja, o tai rodo, kad serumo baltymai „ištraukia“ Ce6 iš komplekso sudėties (Pav. 2.4D) (Dapkute ir kt., 2021).

Serumo baltymų įtaka akivaizdi ir singuletinio deguonies susidaryme. Singuletinis deguonis susidaro fotosensibilizatoriui esant sužadintoje būsenoje. Dėl heterociklinės žiedinės struktūros ir pasikartojančių π orbitalių PS iš sužadintos singuletinės būsenos gali pereiti į tripletinę būseną. Tripletinės būsenos PS sužadinimo energiją gali perduoti greta esančiai deguonies molekulei (Pav. 2.4A). Pagrindinė molekulinio deguonies būsena taip pat yra tripletinė dėl dviejų deguonies atomų vienoje molekulėje su nesuporuotais to paties sukinio elektronais. Sužadintas deguonis tampa singuletiniu deguonimi (DeRosa ir Crutchley, 2002). Tokia deguonies forma yra trumpai gyvuojanti (~4 μs), todėl gali nukeliauti tik trumpus atstumus (<0,02 μm). Singuletinis deguonis oksiduoja įvairias biomolekules ir galiausiai pažeidžia esmines ląstelės struktūras (Redmond ir Kochevar, 2006).

SOSG buvo panaudotas įvertinti susidarančiam singuletinio deguonies kiekiui. Jis yra sudarytas iš fluoresceino molekulės, sujungtos su singuletinį deguonį sulaikančia molekule (antracenu). SOSG turi didelį selektyvumą singuletiniam deguoniui – nereaguoja su laisvaisiais radikalais, tokiais kaip hidroksilo radikalas ar superoksidas. Dėl antraceno dalies SOSG pasižymi silpna mėlyna fluorescencija, kuri po oksidacijos singuletiniu deguonimi pasikeičia į stiprią žalią fluorescenciją dėl fluoresceino dalies (Kim ir kt., 2013). KT, Ce6 ir KT-Ce6 tirpalai buvo švitinti 470 nm bangos ilgio šviesa

surenkant 17,7 J/cm^2 dozę. Nei Ce6, nei KT negeneruoja singuletinio deguonies, nes laisvas Ce6 nėra sužadinamas 470 nm bangos ilgio šviesa, o dar 2003 metais Samia su bendraautoriais pastebėjo, kad KT patys aktyviųjų deguonies formų negeneruoja (Samia ir kt., 2003). Tokius rezultatus gavome ir mes (Dapkute ir kt., 2021). Tuo tarpu KT-Ce6 kompleksas sugeneruoja iki 19 kartų daugiau singuletinio deguonies. Generacijos našumas kiek mažesnis beseruminėje ląstelių augimo terpėje dėl sudėtyje esančių singuletinį deguonį neutralizuojančių komponentų, bet terpę papildžius serumu singuletinis deguonies išvis nesusidaro (Pav. 2.4B) (Dapkute ir kt., 2021). Tai yra dar vienas įrodymas, kad KT-Ce6 kompleksas yra nestabilus ir neveiksmingas kraujo serumo baltymų turtingoje aplinkoje.

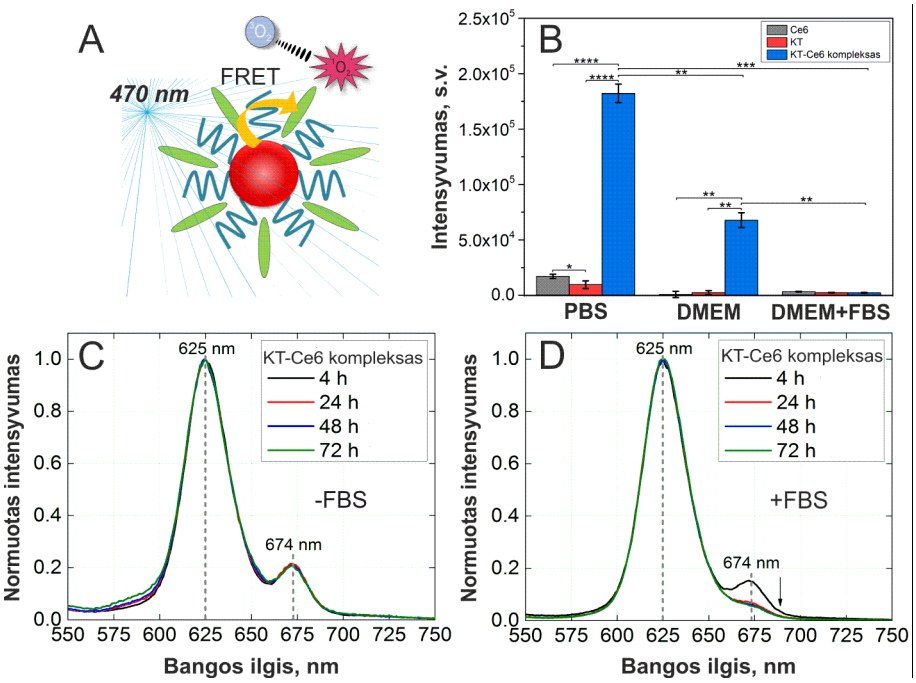

Pav. 2.4. KT-Ce6 komplekso stabilumo ir singuletinio deguonies generavimo tyrimai. A – schematinis sužadinimo energijos perdavimas iš KT (raudona) į Ce6 (žalias ovalas) FRET būdu ir singuletinio deguonies generacijos mėlynos šviesos poveikyje atvaizdavimas. B – SOSG fluorescencijos intensyvumo pokytis po švitinimo ($\lambda_{žad}$ = 470 nm, dozė 17,7 J/cm^2); * rodo statistiškai patikimus skirtumus tarp grupių. C – Normuotas KT-Ce6 komplekso fluorescencijos spektras beseruminėje terpėje. D – Normuotas KT-Ce6 komplekso fluorescencijos spektras seruminėje terpėje. Rodyklė rodo pokyčio kryptį. Pagal Dapkute ir kt., 2021.

Apibendrinant, KT-Ce6 kompleksas išlieka stabilus ilgą laiką ir generuoja didelius kiekius singuletinio deguonies, todėl gali būti naudojamas teranostikoje. Vis dėlto, serumo baltymai destabilizuoja, palyginus, silpną hidrobofinę sąveiką tarp KT dengiančio amfifilinio polimero ir Ce6. Tokie rezultatai limituoja teranostinio KT-Ce6 komplekso panaudojimą intraveninės injekcijos metu. Kitų autorių tyrimai, kuriuose stebima KT-Ce6 komplekso sąveika su ląstelėmis, dažniausiai yra atliekami ląsteles inkubuojant su kompleksu buferiniuose druskų tirpaluose, tokiuose kaip DPBS (Steponkiene ir kt., 2014), HBSS (Hank'o subalansuotas druskos tirpalas, angl. *Hanks Balanced Salt Solution*) (Martynenko ir kt., 2015), arba beseruminėje terpėje (Valanciunaite ir kt., 2014). Mūsų žiniomis, esame pirmieji parodę neigiamą serumo baltymų įtaką nekovalentinio KT-Ce6 komplekso stabilumui.

Iš tyrimų tampa aišku, kad pasyvus ir aktyvus nanodalelių pristatymas į navikus nėra selektyvus, vėžinį audinį pasiekusios nanodalelės neprasiskverbia į gilesnius sluoksnius, o kraujo baltymai greitai neutralizuotų terapinį KT-Ce6 komplekso poveikį. Šie rezultatai padėjo pagrindą teranostinių nanodalelių pristatymo mezenchiminėmis kamieninėmis ląstelėmis tyrimams.

2.4. Odos MKL charakterizavimas

Tyrimuose naudotos žmogaus odos (dermos) mezenchiminės kamieninės ląstelės išskirtos naudojant ekplantų kultūros metodą ir charakterizuotos pagal morfologiją, paviršiaus žymenų raišką ir diferenciacijos potencialą, kaip apibrėžta Tarptautinės ląstelių terapijos draugijos (angl. *International Society for Cellular Therapy*) (Dominici ir kt., 2006). Išskirtos MKL yra verpstės formos, prikimba prie plastiko. MKL pasižymi 100 % MKL būdingų žymenų (CD90, CD73, CD105, CD44) raiška, bet neturi hematopoetinių ląstelių antigenų CD45, CD34, CD14. Paveikus diferenciaciją indukuojančiomis mitybinėmis terpėmis MKL diferencijuojasi adipogenine, osteogenine ir chondrogenine kryptimis (Dapkute ir kt., 2017; Dapkute ir kt., 2021).

Mūsų rezultatai įrodo, kad oda yra tinkamas MKL šaltinis, o eksplantų kultūros metodas yra efektyvus, paprastas ir greitas būdas išskirti MKL išlaikant visas joms būdingas savybes.

2.5. Nanodalelių kaupimasis MKL

Toksiškumo tyrimai parodė, kad KT yra netoksiški MKL koncentracijomis iki 16 nM, todėl ši koncentracija buvo pasirinkta tolimesniems tyrimams kaip

maksimali netoksiška nanodalelių koncentracija (Dapkute ir kt., 2017). Šios koncentracijos KT-Ce6 kompleksas tamsoje taip pat neturi neigiamo toksiško poveikio MKL (Dapkute ir kt., 2021). Saulite ir bendraautoriai ištyrė, kad KT susikaupimas nedaro įtakos ir kitoms MKL savybėms, tokioms kaip proliferacija, imunofenotipas, kryptinga diferenciacija, nėra indukuojama spontaninė diferenciacija (Saulite ir kt., 2017).

KT prie MKL plazminės membranos prisitvirtina jau po 15 min inkubacijos ir į ląstelių vidų patenka aktyvios endocitozės būdu. Endocitozė, prasidėjusi pirmąją inkubacijos valandą, pasiekia sotį po 6 valandų (Dapkute ir kt., 2017; Saulite ir kt., 2017). Saulite ir bendraautoriai parodė, kad KT į ląsteles patenka priklausomai nuo baltymų koronos, susiformuojančios ant nanodalelės paviršiaus – jei baltymų terpėje yra, KT patenka klatrino priklausomos endocitozės būdu, o beseruminėje terpėje – nuo klatrino ir kaveolino/lipidų plaustų priklausančiais endocitozės keliais (Saulite ir kt., 2017). Endocituotos nanodalelės lokalizuojasi pūslelėse ląstelių viduje. Parodyta, kad inkubuojant nanodaleles beseruminėje terpėje jų susikaupimas MKL yra 40 kartų didesnis nei seruminėje terpėje (Dapkute ir kt., 2021). Tai iš dalies galima paaiškinti didesniu skaičiumi aktyvių endocitozės mechanizmų, vykstančių vienu metu nanodalelėms esant beseruminėje terpėje. Detali kolokalizacijos analizė atskleidė KT viduląstelinę dinamiką – pirmas 6 valandas nanodalelės lokalizuojasi ankstyvosiose endosomose ląstelių periferijoje ir aplink branduolį, o vėliau persiskirsto į vėlyvąsias endosomas ir lizosomas (Saulite ir kt., 2017). Vėlesniuose inkubacijos laikuose pūslelių su KT dydis auga, jos susilieja į multivezikulinius kūnus (Dapkute ir kt., 2017). Įdomu tai, kad nanodalelės mezenchiminėse kamieninėse ląstelėse yra ne tik endocituojamos, bet ir gali prisitvirtinti prie MKL sintetinamo tarpląstelinio užpildo (Dapkute ir kt., 2021). Panaši sąveika buvo pastebėta ir kituose darbuose – Kundrotas su bendraautoriais parodė sąsajas tarp MKL užsėjimo tankio ir viduląstelinės bei užląstelinės KT lokalizacijos (Kundrotas ir kt., 2019).

Tiriant KT-Ce6 komplekso stabilumą tirpaluose nustatyta, kad serumo baltymai destabilizuoja kompleksą, todėl seruminė terpė ir intraveninė injekcija nėra tinkami KT-Ce6 komplekso pristatymo būdai. Savo tyrimais parodėme, kad beseruminėje terpėje esantis kompleksas ne tik geriau susikaupia ląstelėse (Pav. 2.5A_1) nei inkubuotas terpėje su serumu (Pav. 2.5A_2), bet ir išlieka stabilus ir efektyvus MKL (Dapkute ir kt., 2021). Naudojant konfokalinę mikroskopiją su fluorescencine laikinės skyros spektroskopija ir FLIM išsiaiškinta, kad MKL viduje esantis kompleksas,

inkubuotas beseruminėje terpėje, išlaiko savo charakteringas spektrų viršūnes ties 624 nm ir 674 nm (Pav. 2.5C_1), o fluorescencijos gyvavimo trukmė yra artima išmatuotai tirpale (Pav. 2.2B) ir siekia $<\tau>$ = 14 ns (Pav. 2.5D_1). Tuo tarpu KT-Ce6 komplekso, inkubuoto terpėje su serumu, fluorescencijos gyvavimo trukmių pasiskirstymas MKL yra platus ir artimas laisvų KT $<\tau>$ (Pav. 2.5D_2), o 674 nm viršūnė išnyksta (Pav. 2.5C_2) (Dapkute ir kt., 2021).

Apibendrinant, KT ir KT-Ce6 kompleksas yra biosuderinami ir efektyviai kaupiasi ląstelėse. MKL apsaugo KT-Ce6 kompleksą nuo destabilizacijos serumo baltymais, todėl ląstelės gali atlikti komplekso nešiklio funkciją.

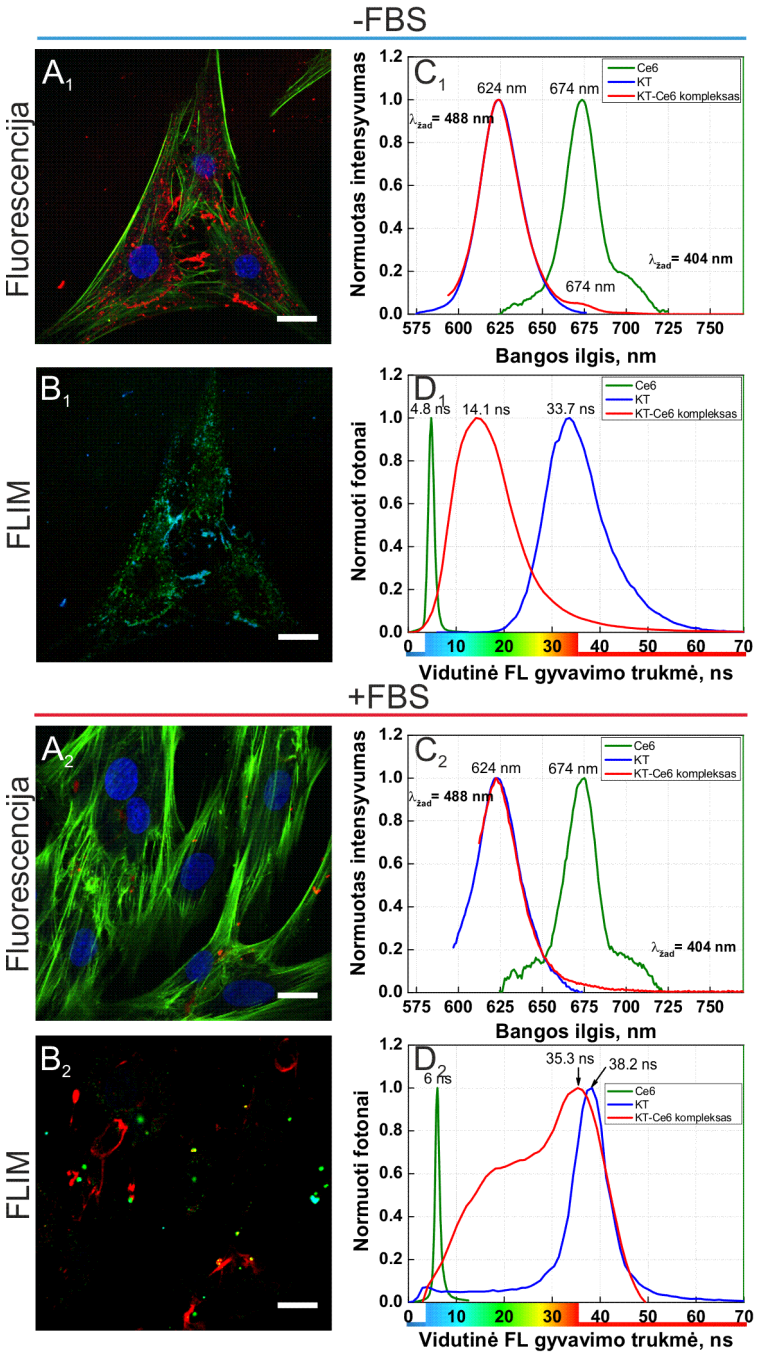

Pav. 2.5. KT-Ce6 viduląstelinė lokalizacija ir stabilumas MKL. A – KT-Ce6 susikaupimas MKL inkubuojant beseruminėje (A_1) ir seruminėje (A_2) terpėje.

Raudona – KT-Ce6 kompleksas, žalia – aktino filamentai, mėlyna – branduoliai. Skalė 20 µm. B – konfokalinės mikroskopijos atitinkami FLIM vaizdai. Skalė 20 µm. Spalvos atitinka fluorescencijos gyvavimo trukmių vaivorykštės skalę. C – normuoti fluorescencijos spektrai. D – vidutinis fluorescencijos gyvavimo trukmių pasiskirstymas ir vaivorykštės skalė. Pagal Dapkute ir kt., 2021.

2.6. MKL sąveika su vėžinėmis ląstelėmis

MKL sąveikauja su įvairiais ląstelių tipais, pavyzdžiui, imuninėmis ląstelėmis. MKL pasižymi imunomoduliuojančiomis ir uždegimines reakcijas slopinančiomis savybėmis, kurios šiuo metu plačiai tyrinėjamos klinikinėse studijose ir yra panaudojamos jau patvirtintuose perianalinių fistulių, osteoartrito, transplantatas prieš šeimininką ligos gydymo būduose (Levy ir kt., 2020). MKL ir vėžinių ląstelių tarpląstelinė sąveika yra tarsi dviašmenis kardas, kartu su gydymo galimybėmis kelianti ir rizikų (Lee ir Hong, 2017). Keletas studijų parodė vėžio vystymąsi skatinančias MKL savybes (Liu ir kt., 2018; Rodini ir kt., 2018) arba spontaninę MKL transformaciją į piktybines ląsteles (Røsland ir kt., 2009), vis dėlto, kai kurie tyrėjai atsiėmė tokias išvadas paaiškėjus, kad MKL kultūros buvo užkrėstos vėžinėmis ląstelėmis, kurios ir sukėlė vėžio progresavimą (Torsvik ir kt., 2010). Priešingi tyrimai atskleidė, kad MKL pasižymi angiogenezę ir vėžinių ląstelių proliferaciją mažinančiu, citotoksiniu ir imunomoduliaciniu poveikiu, todėl pačių MKL priešvėžinės savybės sinergiškai veiktų su gabenamų nanodalelių sukeliamomis pažaidomis (Hmadcha ir kt., 2020).

Esminis MKL paremtos terapijos parametras yra ląstelių migracija link vėžinių ląstelių. Įgimtos onkotropinės MKL savybės kontroliuojamos įvairių chemotaktinių signalų – CXCR4 ir kitų chemokinų receptorių, interleukinų, kraujagyslių endotelio augimo faktoriaus (VEGF), trombocitų kilmės augimo faktoriaus (PDGF) (Hmadcha ir kt., 2020).

Savo tyrimuose parodėme, kaip odos MKL migruoja link krūties vėžio MDA-MB-231 ir nepiktybinių krūties epitelinių MCF-10A ląstelių naudojant Transwell® įdėklus. Ląstelės buvo inkubuojamos beseruminėje terpėje taip eliminuojant galimą MKL migraciją link chemoatraktanto FBS. MKL migracija link teigiamo chemoatraktanto (augimo terpės su FBS) rodo, kad po *ex vivo* kultivacijos MKL išlaiko savo migracines savybes, todėl gali būti padauginamos *in vitro* iki terapijai reikalingo kiekio, nesumažinant ląstelių migracinio potencialo. MKL migracija link vėžinių ląstelių yra 30 kartų

didesnė nei atsitiktinė nekryptinga ląstelių transmigracija pro įdėklo poras link beseruminės terpės. MCF-10A ląstelės buvo pasirinktos kaip sveiko audinio modelis. Gavome, kad migracija link šių nevėžinių ląstelių yra tokia pati, kaip atsitiktinė MKL migracija (<2 %). Vėžinės ląstelės į aplinką sekretuoja įvairius citokinus ir chemokinus, todėl MKL taip pat migruoja ir link terpės nuo vėžinių ląstelių. Palyginamieji migracijos tyrimai atskleidė, kad KT ląstelių migraciją sumažina neženkliai – nėra statistiškai reikšmingo skirtumo tarp nanodalelėmis žymėtų ir nežymėtų MKL transmigracijos (Pav. 2.6A) (Dapkute ir kt., 2017). Norint nustatyti, ar MKL migracija priklauso nuo donoro, buvo palyginta iš trijų skirtingų donorų odos audinių išgautų MKL migracija. Rezultatai neparodė jokių migracijos skirtumų link teigiamos ir neigiamos kontrolės tarp skirtingų donorų ląstelių, tačiau vieno iš trijų donorų MKL migravo geriau tiek su KT, tiek be jų (Dapkute ir kt., 2017).

MKL onkotropinė migracija buvo įrodyta ir *in vivo* modeliuose. Dapkute ir kt. buvo ištirta MKL migracija pelėse, kurioms buvo suformuoti navikai iš žmogaus krūties vėžinių ląstelių (MDA-MB-231). Pelėms MKL su KT viduje buvo suleistos po oda ~10 mm nuo susidariusio naviko. Ištyrus KT turinčias ląsteles įvairiuose organuose, įskaitant navikus ir metastazes, matyti, kad daugiausiai MKL numigruoja į vėžinį audinį. Iškart po suleidimo stebimas signalas blužnyje ir inkstuose, bet po savaitės sumažėja visuose audiniuose, o navike KT žymėtų ląstelių kiekis sumažėja dvigubai. Reikšmingai išaugęs KT kiekis kepenyse po 7 dienų nuo suleidimo gali rodyti MKL su nanodalelėmis persiskirstymą į mononuklearinę fagocitų sistemą ir KT išvalymą iš organizmo (Pav. 2.6B) (Dapkute ir kt., 2017).

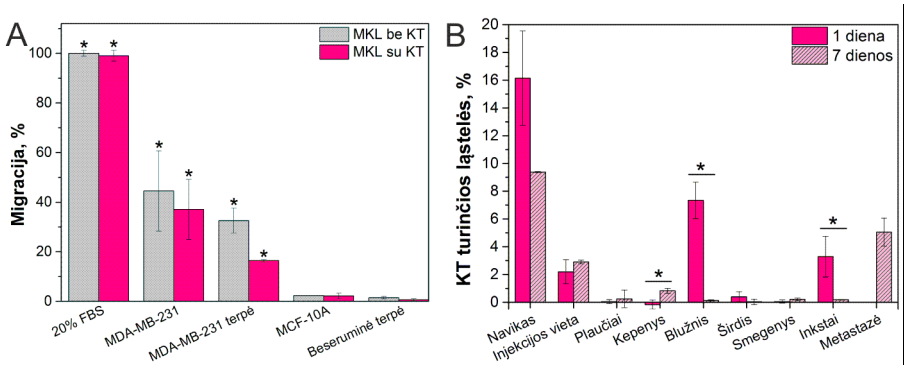

Pav. 2.6. MKL migracija link vėžinių ląstelių. A – MKL *in vitro* migracija pro Transwell® inserto poras link skirtingų chemoatraktantų; * rodo statistiškai reikšmingą skirtumą tarp tiriamų bandinių ir neigiamos kontrolės (beseruminės terpės). B – MKL *in vivo* migracija; naviko homogenato tėkmės

citometrijos rezultatai. Pateikta, kiek iš antikūnu prieš žmogaus CD44 antigeną žymėtų ląstelių yra teigiamos pagal KT signalą; * rodo statistiškai reikšmingą skirtumą tarp 1 ir 7 dienų grupių. Pagal (Dapkute ir kt., 2017).

MKL migracija ir KT-Ce6 komplekso diagnostinis potencialas buvo patvirtinti ir kito tyrimo metu, kuomet navikai buvo sudaryti iš pelių vėžinių ląstelių linijos LLC, o MKL, kaip ir visuose tyrimuose, buvo žmogaus kilmės. Pelių, kurioms ~10 mm žemiau naviko buvo suleistos MKL kartu su teranostiniu kompleksu viduje, išpreparuoti ir po UV lempa padėti navikai pasižymi ryškia raudona fluorescencija, matoma plika akimi (Pav. 2.7A). Detalesnė analizė atskleidė, kad toje pačioje vietoje suleisti KT ar KT-Ce6 kompleksas nepasiekia naviko ir nėra tinkami teranostikai. Tuo tarpu kompleksą įterpus į MKL, naviko pjūvių konfokalinės mikroskopijos mikrografijose matomas ryškus, plačiai pasiskirstęs KT fotoliuminescencijos signalas (Pav. 2.7B), kurio spektras pasižymi dideliu fluorescencijos intensyvumu bei kompleksui charakteringomis viršūnėmis ties 625 nm ir 674 nm (Dapkute ir kt., 2021).

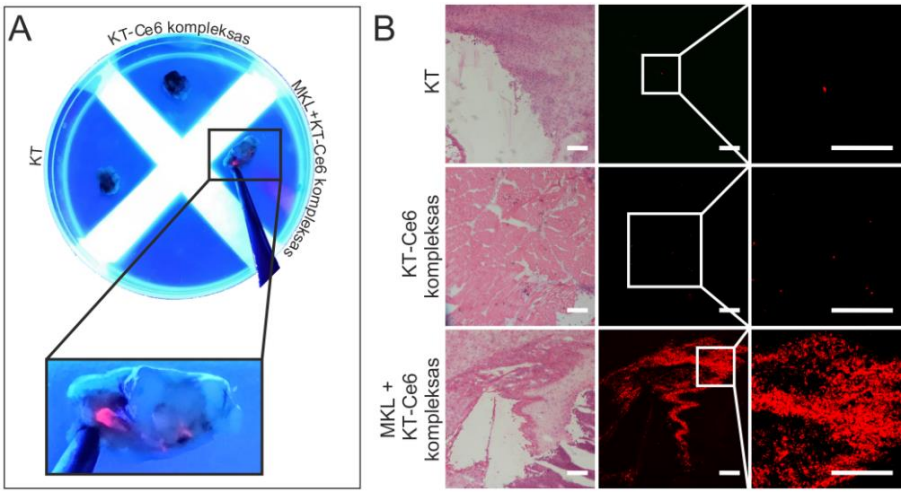

Pav. 2.7. KT-Ce6 komplekso *in vivo* diagnostinis potencialas. A – pelių, kurioms suleisti KT, KT-Ce6 kompleksas ir MKL+KT-Ce6 kompleksas navikai po UV lempa. B – Histologiniai ir konfokaliniai atitinkamų navikų mikropjūvių vaizdai. Skalė 100 µm. Pagal Dapkute ir kt., 2021.

Apibendrinant, šie *in vitro* ir *in vivo* rezultatai užtikrina egzogeninių MKL panaudojimą teranostinių nanodalelių transportavimui. Verta užakcentuoti, kad MKL buvo išskirtos iš žmogaus odos audinių, tačiau buvo patvirtinta jų migracija tiek link žmogaus, tiek link pelės ląstelių kilmės navikų. Kitų autorių jau buvo parodyta, kad MKL migracijai į navikus nėra būdingi rūšiniai barjerai. MKL išvengia alogeninių reakcijų, todėl klinikoje naudojami donorinių (alogeninių) MKL pažangios terapijos vaistiniai preparatai (Yu ir kt., 2018). Li su bendraautoriais, išanalizavę 94 publikacijas su tarprūšiniu MKL panaudojimu, pateikė išvadas, kad net 93,6 % atvejų MKL gali įsitvirtinti ir veikti nepaisant rūšinio barjero (Li ir kt., 2012). Nakamizo tyrimai buvo vieni pirmųjų tokios MKL specifinės migracijos srityje – *in vivo* modeliuose parodyta, kad MKL migruoja tik link vėžinių ląstelių, bet ne panašaus fenotipo nevėžinių ląstelių, migracijai nėra svarbu skirtumai tarp donuojančios ir gaunančios rūšies, o MKL migracija nepriklauso nuo suleidimo būdo – į audinius suleistos MKL link vėžinių ląstelių migruoja taip pat gerai, kaip ir suleistos intraveniškai (Nakamizo ir kt., 2005).

2.7. PDT efektas *in vitro* ir *in vivo* modelinėse sistemose

Anksčiau parodyta, kad kompleksas šviesos poveikyje generuoja singuletinį deguonį (Pav 2.4B). Siekiant įvertinti, kokį fotosensibilizacinį poveikį gali turėti KT-Ce6 kompleksas MKL ir vėžinėms ląstelėms, mezenchiminės kamieninės ir MDA-MB-231 linijos ląstelės buvo inkubuotos su kompleksu ir pašvitintos 470 nm bangos ilgio šviesa surenkant suminę 17,7 J/cm^2 dozę. Tokia švitinimo dozė, kaip pakankama sukelti ląstelių žūčiai taikant chlorinu e6 pagrįstą fotodinaminę terapiją, pasirinkta atlikus dozės titravimo tyrimus ir remiantis ankstesnėmis studijomis (Skripka ir kt., 2018; Steponkiene ir kt., 2014). Taip pat, mūsų rezultatai rodo, kad veikiant tokia doze greičiausiai indukuojama ląstelių apoptozė, o ne nekrozė (Dapkute ir kt., 2021). Nekrozė yra nekontroliuojamas procesas, sukeliantis netiesioginę žalą per uždegiminių procesų kaskadų iniciaciją, kai tuo tarpu apoptozė yra reguliuojama ir sumažina pažaidas gretimoms ląstelėms (D'Arcy, 2019). Gauti rezultatai rodo, kad 100 % MKL žūsta po KT-Ce6 komplekso beseruminėje terpėje ir šviesos poveikio. MDA-MB-231 yra trigubai neigiamos, prastai diferencijuotos ir blogiausią prognozę lemiančios krūties vėžinės ląstelės, atsparios skirtingo tipo gydymui (Chavez ir kt., 2010; Huang ir kt., 2020; Nedeljković ir Damjanović, 2019), todėl mūsų tyrimuose pasirinktos neatsitiktinai. Dėl didesnio atsparumo įvairiems gydymo

metodams, dalis MDA-MB-231 ląstelių išlieka gyvos po taikytos PDT, nors ir su apoptozės požymiais (Dapkute ir kt., 2021). PDT lemia citochromo c, atsakingo už apoptozės indukciją, paleidimą iš mitochondrijų – citoplazmoje susiformuoja apoptosomos, aktyvuojamos kaspazė-3 ir kaspazė-9, kurios atlieka esminę rolę apoptozėje (Redmond ir Kochevar, 2006).

Kiekybiškai XTT ląstelių proliferacijos rinkiniu įvertinus KT-Ce6 komplekso įtaką ląstelių gyvybingumui ir metaboliniam aktyvumui matyti, kad kompleksas netoksiškas tamsoje ir be švitinimo yra inertiškas, tačiau šviesos poveikyje nei MKL ir vėžinės ląstelės, nei jų kokultūra (santykiu 2:1) PDT galiausiai neišgyvena (Pav. 2.8). Verta paminėti, kad fotopažaidos yra sukeliamos tik inkubuojant KT-Ce6 kompleksą beseruminėje terpėje – terpė, papildyta serumo baltymais, ląstelių gyvybingumo nesumažina, nes, kaip minėta ankstesniuose skyriuose, destabilizuojama sąveika tarp KT ir Ce6 (Dapkute ir kt., 2021).

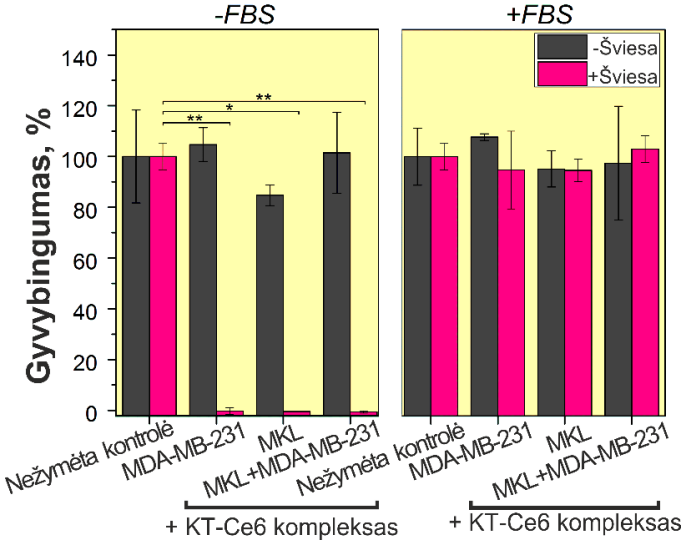

Pav. 2.8. MDA-MB-231, MKL ir MDA-MB-231+MKL kokultūros (santykiu 1:2) gyvybingumas po inkubacijos KT-Ce6 kompleksu ir švitinimo 470 nm bangos ilgio šviesa. * rodo statistiškai reikšmingus skirtumus. Pagal Dapkute ir kt., 2021.

Priešvėžinė mezenchiminėmis kamieninėmis ląstelėmis ir fotosensibilizaciniais procesais paremta terapija buvo įrodyta kokultūrose, sudarytose iš vėžinių ląstelių ir MKL, kurių viduje yra KT-Ce6 kompleksas (santykiu 1:2). Terapijos efektyvumui užtikrinti yra du galimi teranostinių nanodalelių perdavimo iš MKL į vėžines ląsteles būdai.

Pirma, galimas nanodalelių apsikeitimas tarp MKL ir vėžinių ląstelių tiesioginio kontakto ar netiesioginės sąveikos būdu. Saulite su bendraautoriais, naudodami trimačius MKL ir vėžinių ląstelių kokultūros modelius, nustatė, kad trečdalis KT iš MKL yra perduodama greta esančioms vėžinėms ląstelėms (Saulite ir kt., 2018). MKL ir vėžinės ląstelės netiesioginiu būdu gali sąveikauti išmesdamos medžiagas į tarpląstelinį užpildą ar suformuodami charakteringas struktūras, tokias kaip egzosomos ir mikropūslelės, o tiesioginio kontaktavimo metu tarp ląstelių gali susidaryti plyšinės jungtys, nanovamzdeliai, ar membranų ir/ar citoplazmų susiliejimas (Melzer ir kt., 2016). Pietilä su bendraautoriais detaliai aprašė bent tris KT apsikeitimo tarp MKL ir MDA-MB-231 būdus 2D ir 3D kokultūrose – į filopodijas panašiomis struktūromis, tiesioginiu membranų ir ląstelės turinio susiliejimu bei egzosomomis (Pietilä ir kt., 2013). Saulite ir bendraautorių darbe KT iš MKL yra pašalinami greičiausiai P-glikoproteinų efliukso būdu (Saulite ir kt., 2018).

Norėdami padidinti terapijos sėkmingumą pritaikėme antrąjį nanodalelių perdavimo iš MKL vėžinėms ląstelės būdą – dvigubo švitinimo procedūrą, kurios metu po pirmojo švitinimo MKL yra pažeidžiamos ir KT-Ce6 kompleksas paleidžiamas į užląstelinę erdvę, iš kurios yra greitai endocituojamas aplinkinių vėžinių ląstelių, o antrasis švitinimas pažeidžia vėžines ląsteles. Mūsų eksperimentiniai rezultatai parodė, kad po pirmojo kokultūros švitinimo pažeidžiama apie pusė ląstelių, o po antrojo švitinimo (praėjus 24 val. po pirmojo) didžioji dalis ląstelių yra žuvusios arba suapvalėjusios morfologijos ir pažeisto ląstelių vientisumo (Pav. 2.9). (Dapkute ir kt., 2021). Tyrimai patvirtina, kad KT-Ce6 kompleksas išlieka stabilus po pirmojo švitinimo ir dar yra pajėgus toliau kovoti su vėžinėmis ląstelėmis antrojo švitinimo metu.

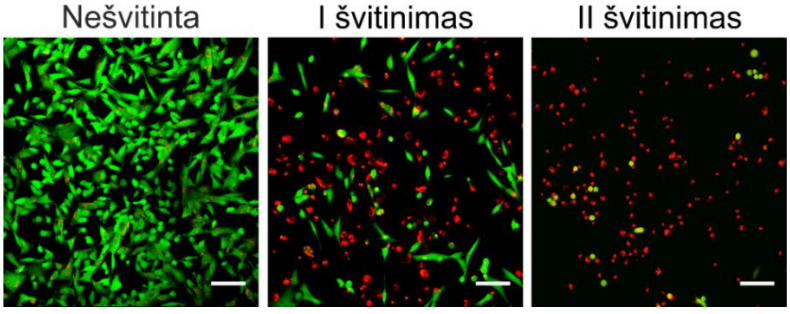

Pav. 2.9. MKL ir MDA-MB-231 ląstelių kokultūros PDT, atliekant dvigubo švitinimo procedūrą. Žalia – gyvos ląstelės (kalceinas), Raudona – negyvos ląstelės (EthD-1). Skalė 100 μm. Pagal Dapkute ir kt., 2021.

Terapinis efektyvumas buvo įrodytas ir pelėse su navikais. Pelėms ~10 mm žemiau naviko buvo suleista viena iš penkių medžiagų – fiziologinis tirpalas, MKL, MKL su KT, MKL su Ce6 arba MKL su KT-Ce6 kompleksu. Komplekso ar jo sudedamųjų dalių terapinis efektyvumas atskirai be MKL netirtas, nes ankstesni tyrimai įrodė, kad tik MKL transportuojamos teranostinės molekulės selektyviai susikaupia navike (Dapkute ir kt., 2017; Dapkute ir kt., 2021). Pelės buvo švitinamos anksčiau patikrinta dvigubo švitinimo procedūra surenkant suminę 120 J/cm^2 terapinę dozę, nes rekomenduojama PDT metu neviršyti 125 J/cm^2 dozės (Dhillon ir kt., 2016). Po gydymo MKL su KT-Ce6 kompleksu viduje, navikai yra 4 kartus mažesni ir pelių išgyvenamumas yra statistiškai reikšmingai didesnis nei kitos grupėse (Pav. 2.10A-C). Verta paminėti, kad pelių, gydytų teranostiniu nanokompleksu, plaučiuose nėra stebima metastatinių mazgelių, kurie yra ypač dažni kitose grupėse dėl greito LLC linijos ląstelių metastazavimo į plaučius (Pav. 2.10D). Apie 2/3 mirčių nuo solidinių navikų sukelia metastazės (Dillekås ir kt., 2019). Todėl toks metastazavimą mažinantis terapijos efektas ženkliai sustiprina pasirinktos gydymo strategijos pritaikomumą ir aktualumą. Histopatologinė analizė parodė, kad MKL su KT-Ce6 kompleksu gydytų pelių navikuose reikšmingai daugiau nekrozės plotų, mažesnis mitozių skaičius bei trigubai didesnis apoptozių skaičius nei negydytose pelėse. Negydytų pelių plaučiuose taip pat buvo rastos dauginės iki 5 mm skersmens metastazės, o tuo tarpu gydytose pelėse buvo nustatytos pavienės 0.5-1 mm skermens mikrometastazės. Pagrindinių pelių organų mikroskopinis palyginamasis vertinimas ir hematologinė analizė neparodė jokių specifinių pakitimų, kurie galėtų kelti susirūpinimą dėl terapijos saugumo (Dapkute ir kt., 2021).

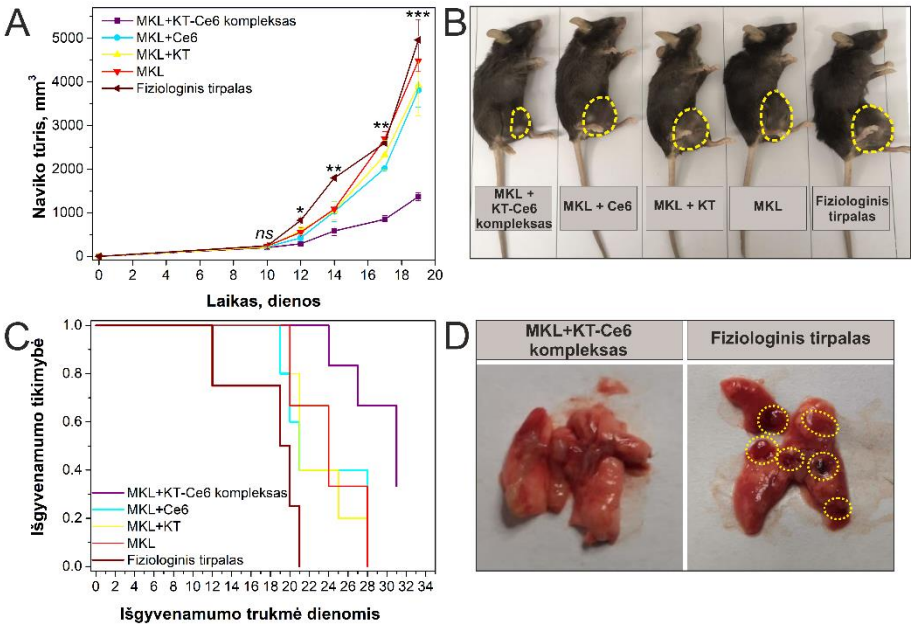

Pav. 2.10. KT-Ce6 komplekso *in vivo* terapinis potencialas. A – naviko augimo kreivė; * rodo statistiškai reikšmingus skirtumus tarp „MKL+KT-Ce6 kompleksas" grupės ir kitų tirtų grupių, *ns* – nėra skirtumo. MKL suleidimas atliktas 10 dieną po naviko iniciacijos, švitinimai atlikti 11 ir 12 tyrimo dienomis. B – reprezentatyvios pelių iš kiekvienos grupės fotografijos (19 diena). Geltonu punktyru pažymėtos naviko ribos. C – Kaplano ir Mejerio išgyvenamumo kreivės. „MKL+KT-Ce6 kompleksas" grupės išgyvenamumas yra statistiškai reikšmingai didesnis (*log-rank* testas p = 0,003). D – pelių, gydytų MKL+KT-Ce6 kompleksu, ir pelių, gydytų fiziologiniu tirpalu, plaučiai. Geltonu punktyru pažymėtos metastazės. Pagal Dapkute ir kt., 2021.

IŠVADOS

1. Pasyvus KT susikaupimas ir pasiskirstymas navike po intranavikinės injekcijos yra minimalus bei heterogeniškas. 3D ląsteliniuose sferoiduose ir navikuose KT kaupiasi tik periferinėse vėžinėse ląstelėse ir neprasiskverbia į 3D sferoido/naviko centrinę dalį.
2. Kompleksas tarp KT ir Ce6 susiformuoja per 4 valandas ir pasižymi charakteringomis savybėmis – KT fotoliuminescencijos intensyvumo sumažėjimu, išaugusia ir pasislinkusia į ilgabangę spektro pusę Ce6 fluorescencija bei sutrumpėjusia KT fluorescencijos gyvavimo trukme. Tinkamiausi komplekso formavimui yra amfifiliniu polimeru ir karboksilo grupėmis funkcionalizuoti KT. KT-Ce6 kompleksas išlieka stabilus vandeniniuose tirpaluose ir generuoja singuletinį deguonį po sužadinimo kompleksui specifiška 470 nm bangos ilgio spinduliuote, tačiau yra destabilizuojamas kraujo serumo baltymais.
3. Ląstelės, išskirtos iš odos audinio eksplantų kultūros metodu, pasižymi didele CD90, CD73, CD105 ir CD44 žymenų raiška, bet neekspresuoja CD45, CD34 ir CD14 paviršiaus biožymenų bei diferencijuojasi adipogenine, osteogenine ir chondrogenine kryptimis, todėl yra charakterizuotos kaip MKL.
4. KT ir KT-Ce6 kompleksas yra greitai endocituojami mezenchiminių kamieninių ląstelių, lokalizuojasi endosomose ir lizosomose, bet nesumažina ląstelių gyvybingumo, kol nėra indukuojami fotocheminiai procesai. KT-Ce6 kompleksas MKL viduje yra apsaugomas nuo neigiamo kraujo serumo baltymų poveikio ir išlieka stabilus bei veiksmingas visos fototerapinės procedūros metu. MKL selektyviai migruoja link vėžinių ląstelių *in vitro* modelinėje sistemoje ir *in vivo* link navikų, suformuotų tiek iš žmogaus, tiek iš pelės vėžinių ląstelių, o tirtos nanodalelės nesumažina MKL migracinio potencialo.
5. MKL padidina KT-Ce6 komplekso susikaupimą navike, o akimi stebima KT fotoliuminescencija yra tinkama siekiant įvertinti naviką ir jo išplitimo ribas. MKL perduoda KT-Ce6 kompleksą vėžinėms ląstelėms ir dvigubo švitinimo procedūros metu sukelia vėžinių ląstelių žūtį. Kombinuota MKL, KT-Ce6 ir netoksiškos šviesos terapija reikšmingai didina išgyvenamumą, lėtina navikų augimą, mažina metastazių atsiradimą ir vėžio progresavimą. Mūsų rezultatai patvirtina, kad MKL, žymėtos KT-Ce6 kompleksu, gali būti pritaikomi vėžio teranostikoje.

SUMMARY

Introduction

The lack of early cancer diagnosis and poor selectivity of current treatment methods are among the main challenges of oncology. Photosensitizer (PS) and nanoparticle complexes can be used as a novel therapeutic modality. PS are inert in the dark and become toxic to cells only in visible light, as they generate reactive oxygen species due to molecular transformation cascades. Since therapeutic effect is achieved only by light illumination, photodynamic therapy (PDT) works locally and systemic side effects, usually associated with standard chemotherapy, are reduced and the treatment effectiveness is increased. PDT is minimally invasive and does not require complex surgical interventions, can be repeated several times without cumulative toxicity, effectively destroys or at least reduces the tumor.

With the development of nanotechnologies, PDT has not been forgotten. Due to their large surface area, nanoparticles can bind numerous PS molecules to its surface, protect therapeutic molecules during transport to tumors as well as solve aggregation and hydrophobicity issues. Nanosized materials also demonstrate unique properties, such as superparamagnetism or photoluminescence (PL). Quantum dots (QDs) are characterized by high quantum yield, photostability, bright PL, wide absorption and narrow emission spectrum, high two photon absorption, all of which are suitable for improved cancer diagnostics. QDs can also serve as energy donors – due to the overlap of QD photoluminescence and PS absorption spectra, excited QDs transfer energy to attached PS *via* Förster resonance energy transfer (FRET). The formation of QD-PS complex provides a *theranostic* platform – the bright PL of the nanoparticles performs a diagNOSTIC function, while the PS offers a THERApeutic one.

However, nanoparticles and their complexes do not have enough selectivity for tumors and tend to accumulate non-specifically in the liver, lymph nodes, spleen. Regardless of whether active or passive targeting was used, more than 99 % of injected nanoparticles do not reach the tumors (Dai et al., 2018).

Cellular hitchhiking of therapeutic agents has been proposed as an alternative way of delivering nanoparticles. Erythrocytes, macrophages and lymphocytes have already been used to perform this task, but their selectivity for tumors is limited (Singh and Mitragotri, 2020). The delivery of anticancer

drugs using cells with innate tumor-tropic properties is biocompatible, clinically safe and has shown great success in preclinical studies (McMillan, Batrakova, and Gendelman, 2011). Mesenchymal stem cells (MSCs) are considered one of the most promising choices. MSCs are multipotent cells with immunomodulating, regenerative and migratory properties, improving nanoparticle delivery by four times (Durymanov, Rosenkranz, and Sobolev, 2015).

This work investigates MSC response to QDs and QD and photosensitizer chlorin e6 (Ce6) complexes and their potential for theranostic.

The aim: to study the ability of skin mesenchymal stem cells to selectively transport theranostic nanoparticles to tumors, ensuring therapeutic effect and diagnostic potential.

The main tasks:

1. To investigate the accumulation and distribution of QDs in 2D, 3D cancer cell monocultures and *in vivo* tumor models.
2. To form QD and Ce6 complex and to analyze its physicochemical properties, single oxygen generation efficacy, stability in different media and the influence of proteins.
3. To isolate MSCs from donor skin tissues using explant culture method and to identify them by MSC characteristics.
4. To determine the accumulation of QDs and QD-Ce6 complex in skin MSCs and MSC ability to transport nanoparticles to tumors in *in vitro* and *in vivo* model systems.
5. To evaluate the diagnostic and photodynamic effect of the QD-Ce6 complex transported by the skin MSCs in *in vitro* and *in vivo* model systems.

Scientific novelty

Usually, similar researches are carried out with bone marrow or adipose tissue derived stem cells, while the number of studies performed on the dermal MSCs is minimal, and to our knowledge, the research on migratory transportation of theranostic nanomaterials using such cells was carried out for the first time. Due to the high demand for regeneration, skin is rich in MSC niches, and the tissue itself can be taken with minimally invasive procedures, quickly regenerates, and has a large surface area. The skin left over from various surgeries as medical waste could be easily used for economical and donor-friendly anticancer treatment.

The work was carried out with human skin MSCs that were isolated by explant culture method, which is a relatively rarely used method of obtaining stem cells. In other studies, stem cells are isolated by enzymatic dissociation, where various enzymes release MSCs from the donor tissue, but at the same time may adversely affect cell surface proteins, MSC properties such as proliferation, heterogeneity, and yield. The extracellular matrix, stromal cells, signaling molecules, cytokines, growth factors, 3D environment of MSCs is maintained in explant culture, therefore the transition to 2D *in vitro* culture is gentler, MSCs have a higher proliferation capacity and yield.

Human MSCs were used in the work, and the migratory effect was obtained despite the species barrier – MSCs migrated in both immunodeficient mice with human tumor xenografts (axis human→ human) and in mouse tumor-bearing models (axis human→mouse), thus showing the versatility of this a therapy and the low probability of allogeneic reactions.

In this work, we explored the influence of serum proteins on the stability of QD-Ce6 complex and its ability to generate singlet oxygen. Other studies analyzing the properties of QD-Ce6 complex investigate the complex only in protein-free solutions. Our studies have shown that serum proteins pull Ce6 out from the coating of QDs, thus minimizing singlet oxygen generation and PDT efficacy. It was shown for the first time that MSCs protect QD-Ce6 complex from destabilization. To our knowledge we are the first ones to study the complex formation and subsequent PDT effect between photosensitizer and QDs with amphiphilic polymer and different surface charge.

Studies with QD-Ce6 complex can be found in the literature, but for the first time its effectiveness was demonstrated not only in the *in vitro* system, but also in a living organism. In this study, theranostic effect was shown in both *in vitr*o and *in vivo* systems and optical fluorescent diagnostics was combined with PDT.

Practical value

The potential of MSCs as carriers of theranostic nanoparticles needs to be tested in larger-scale *in vivo* experiments in order to safely transfer the studies to Phase I/II clinical trials. The number of clinical trials conducted with MSCs delivering drugs is still negligible. Only four studies with MSCs transporting interferon β or oncolytic viruses are registered in the Clinical Trials Registry *clinicaltrials.gov*. The full application of the proposed strategy for the treatment of cancer patients requires a more detailed verification of the effect and comparison between MSCs from different sources. Also, in order to

personalize the treatment, it is important to evaluate the suitability of therapy for tumors of different localization.

QDs made of heavy metals may not be applicable for translating this treatment strategy into the clinic due to the risk of chronic toxicity. However, at current stage, these nanoparticles are well suited as a model system. Research will become even more practical in the future with the development of biodegradable or easily excreted nanoparticles possessing similar physicochemical properties as QDs. Next generation heavy metal-free QDs are being investigated, yet their spectral properties do not equal the characteristics of those, composed of Cd or Pb, therefore they could not fully provide diagnostic function.

QD-Ce6 complex excited in the UV-Vis spectral range may also be more difficult to apply in standard clinical diagnostics, especially for imaging and treatment of tumors in deeper tissues. However, modern fiber optics and endoscopic technologies enable PDT to be used with endoscopic, laparoscopic, or intraoperative light delivery systems. To increase tissue penetration and therapy efficacy, QD-Ce6 complex could be excited using two-photon absorption as QDs have large two-photon cross-section. Its main advantage is the use of near-infrared light, which is less absorbed by the tissue compared to visible light and allows excitation to a deeper layer. Two-photon excitation and use of nanoparticles with an intrinsic near-infrared absorption is the future direction of such research and application.

Results

First, we compared the accumulation of QDs in *in vitro* cancer cell 2D monolayers, 3D spheroids and *in vivo* tumor xenografts and showed that almost all cells accumulate nanoparticles in the 2D monolayer, yet only 60-70 % and 10-30 % of the cells accumulate QDs in 3D spheroids and tumors, respectively. A more detailed analysis indicated that the uptake in both 3D spheroids and tumors is heterogeneous and QDs localize only in the cells on the periphery with almost no penetration into the central part (Jarockyte et al., 2018). As our results demonstrate minimal intratumoral accumulation and distribution of passively targeted nanoparticles, further research and the development of new therapeutic approach based on the delivery of theranostic nanoparticles to tumours *via* MSCs was conducted.

To determine which type of QD coating is the most suitable for formation of the complex with Ce6, we have examined four different types of nanoparticles – coated with either phospholipids or amphiphilic polymer and functionalized with amino or carboxyl functional groups. All studies with QD-Ce6 complex were carried out with excitation or irradiation by complex-specific 470 nm light. This wavelength is absorbed by QDs, yet the absorption of Ce6 in this part of the spectrum is minimal (Skripka et al. 2018; Dapkute et al., 2021). In this way, only QDs are excited in the complex, and Ce6 fluorescence, singlet oxygen generation, and PDT effect are determined by FRET between QDs and Ce6. Our results showed, that no matter the coating and charge, the formation of the complex begins immediately after the mixing Ce6 and QD solutions and lasts about 4 hours until equilibrium is reached (Dapkute et al., 2021). QD-Ce6 complex forms due to non-covalent hydrophobic interaction between non-polar moieties of Ce6 and amphiphilic or lipid-based QD coating. QD-Ce6 complex can be identified by a few parameters (Skripka et al., 2018; Dapkute et al., 2021):

- QD photoluminescence intensity decreases;
- Ce6 fluorescence intensity increases significantly and the fluorescence maximum has a bathochromic shift (660 nm → 672-674 nm);
- Fluorescence lifetime of QDs in QD-Ce6 complex becomes shorter ($<\tau>_{QDs}$ = 35.7 ns, $<\tau>_{QD\text{-}Ce6\ complex}$ = 14.5 ns).

In vitro studies of QD-Ce6 complexes with different coatings demonstrated that the highest intracellular accumulation and PDT effect can be achieved when carboxyl group functionalized amphiphilic polymer coated QDs are used to form QD-Ce6 complex (Skripka et al., 2018). We have also determined that up to 100 Ce6 molecules can be attached to a single amphiphilic polymer coated QD, thus maximizing the efficiency of PDT (Dapkute et al., 2021). To sum up, the interaction between QDs and Ce6 occurs rapidly and has characteristic features, and QD-Ce6 complex, consisting of QDs, coated with negatively charged carboxyl groups functionalized amphiphilic polymer, accumulates the best in cells and has the greatest PDT effect.

At the next stage of the study, we evaluated stability of QD-Ce6 complex in serum-free and serum-supplemented media. In serum-free medium QD-Ce6 complex maintains its characteristic spectral properties, yet serum-supplemented medium lead to a sharp decline of 674 nm peak. Our results

suggest that serum proteins destabilize QD-Ce6 complex and pull Ce6 out from the coating of QDs (Dapkute et al., 2021). Singlet oxygen generation was also affected by protein-rich medium. When irradiated with 470 nm light to collect 17.7 J/cm^2 dose, QD-Ce6 complex generates up to 19 times more singlet oxygen than its free counterparts Ce6 and QDs, therefore the complex is suitable for PDT. Although singlet oxygen generation yield is slightly lower in serum-free cell growth medium, no singlet oxygen forms when the medium is supplemented with serum (Dapkute et al., 2021).

We have successfully isolated human skin (dermal) MSCs from donor skin tissues using explant culture method. Isolated cells were defined as MSCs by morphology, immunophenotyping, and adipogenic, osteogenic, and chondrogenic differentiation. Our results confirm that skin is a suitable source of MSCs, and the explant culture method is an effective, simple, and fast way to isolate MSCs (Dapkute et at., 2017; Dapkute et al., 2021).

Next, we examined the toxicity of nanomaterials to MSCs and showed that maximum non-toxic concentration of QDs is 16 nM (Dapkute et al., 2017). QD-Ce6 complex used at this concentration also does not induce dark toxicity (Dapkute et al., 2021). QDs attach to the plasma membrane of MSCs after 15 min incubation and enter the cells *via* active endocytosis and reaches the saturation after 6 hours (Dapkute et al., 2017; Saulite et al., 2017). Nanoparticles localize in the endocytic vesicles inside the cells as well as attach onto the extracellular matrix. Our studies demonstrated that QD-Ce6 complex in serum-free medium not only accumulates better in cells than when incubated in serum-supplemented medium, but also maintains characteristic spectral peaks at 624 nm and 674 nm while in MSCs. QD-Ce6 complex stability was additionally proven by time-resolved fluorescence spectroscopy and fluorescence lifetime imaging microscopy (Dapkute et al., 2021). In conclusion, QDs and QD-Ce6 complexes are biocompatible and have efficient accumulation in cells. What is more, MSCs protect QD-Ce6 complex from destabilization by serum proteins, allowing cells to act as carriers of the complex.

We then examined MSC tumor-tropic migration. *In vitro* migration of MSCs toward breast cancer cells was up to 30 times higher than random undirected cell migration, while MSC migration toward non-cancerous breast epithelial cells was negligible. Comparative migration studies showed no

statistically significant differences between migration of QD-labeled and unlabeled MSCs (Dapkute et al., 2017). We also studied MSC *in vivo* migration toward human tumor xenografts. The results showed, that upon subcutaneous QD-labeled MSC injection ~10 mm below the tumor, MSCs with nanoparticles inside were detected mainly in the tumor and metastases, almost bypassing healthy tissues (Dapkute et al., 2017). Our research has also confirmed QD-Ce6 complex-loaded MSC migration toward mouse tumor models. Excised tumors had pronounced red fluorescence under UV light, visible to the naked eye. Histological analysis showed that free QDs and free QD-Ce6 complex do not migrate toward tumors and do not label cancerous tissue. Yet, when MSCs+QD-Ce6 complex was injected, mice tumors had widely distributed QD photoluminescence signal (Dapkute et al., 2021). Overall, our *in vitro* and *in vivo* results ensure the use of exogenous MSCs for the delivery of theranostic nanoparticles.

In order to assess the potential PDT effects of QD-Ce6 complex on MSCs and cancer cells, QD-Ce6 complex-loaded cells were irradiated with complex-specific 470 nm wavelength to collect 17.7 J/cm^2 therapeutic dose. Results showed that QD-Ce6 complex incubation in serum-free medium and subsequent light irradiation is lethal to MSCs, while cancer cells are more resistant to treatment, however, remaining cancer cells show signs of apoptosis. Both cell types were almost unaffected upon QD-Ce6 complex incubation in serum-supplemented medium (Dapkute et al., 2021). Next, we explored anticancer effect of QD-Ce6 complex-loaded MSCs co-culturing them with cancer cells. To maximize the efficacy of the therapy, two-step irradiation treatment was performed with two irradiations by 470 nm light achieving 17.7 J/cm^2 dose every 24 hours. Our research demonstrated that after the first irradiation about 50 % of cells remain viable. However, after a second irradiation most of the cells are dead and the remaining ones have rounded morphology and show signs of damaged cellular integrity. Our findings indicate QD-Ce6 complex stability after first irradiation and ability to fight cancer cells during the second one (Dapkute et al., 2021).

Finally, therapeutic efficacy was demonstrated *in vivo*. Tumor-bearing mice were injected with MSCs+QD-Ce6 complex and irradiated twice every 24 hours to collect cumulative therapeutic dose of 120 J/cm^2. Our results demonstrate that tumors treated with QD-Ce6 complex-loaded MSCs were 4

times smaller and mice survival is statistically significantly higher than that of untreated mice. Treatment also prevented macrometastases formation in the lungs, as no metastatic nodules were visible to the naked eye. Histopathological analysis showed that mice treated with MSCs and QD-Ce6 complex have significantly larger necrotic areas, lower mitotic count, and 3-fold higher number of apoptotic cells. When microscopically comparing metastases, their number and size in the lungs is higher in the lungs of untreated mice. Histological assessment of the main organs did not indicate any specific changes that could raise safety concerns (Dapkute et al., 2021).

Conclusions:

1. Passive accumulation and distribution of QDs in the tumor after intratumoral injection is minimal and heterogeneous. In 3D cellular spheroids and tumors, nanoparticles accumulate only in the periphery and do not penetrate into the central part of the 3D spheroid/tumor.
2. The complex between QDs and Ce6 is formed within 4 hours and has characteristic features – a decrease of QD photoluminescence intensity, increased and red-shifted peak of Ce6 fluorescence, and shortened QD fluorescence lifetime. Amphiphilic polymer coated and carboxyl groups functionalized QDs are the most suitable for the complex formation. Moreover, QD-Ce6 complex remains stable in protein-free aqueous solutions and generates high amounts of singlet oxygen after irradiation, but is rapidly destabilized by serum proteins.
3. MSCs were successfully isolated from donor skin tissues and were characterized by morphology, mesenchymal immunophenotype, and differentiation potential.
4. QDs and QD-Ce6 complexes are rapidly taken up by MSCs and are located in endocytic vesicles inside the cells. Furthermore, neither QDs, nor QD-Ce6 complex are not cytotoxic before initiation of photochemical processes. When loaded into MSCs, QD-Ce6 complex is protected from adverse effects of serum proteins and remains effective throughout the PDT procedure. Most importantly, MSCs migrate selectively *in vitro* to cancer cells and *in vivo* to tumors over species barrier. In addition, QDs do not reduce migratory potential of MSCs.
5. MSCs increase stability and intratumoral accumulation of QD-Ce6 complex with QD fluorescence visible to the naked eye. QD-Ce6 complex-loaded MSCs cause cancer cell death during two-step

irradiation treatment. The combination of MSCs, QD-Ce6 complex, and non-toxic light significantly increases survival, reduces tumor growth, metastatic potential and overall cancer progression. Our results confirm that MSCs with QD-Ce6 complex can be applied in cancer theranostics.

Agostinis P, Berg K, Cengel KA, Foster TH, Girotti AW, Gollnick SO ir kt. Photodynamic therapy of cancer: an update. *CA. Cancer J. Clin.* **2011**;61(4):250–81.

Chavez KJ, Garimella SV, Lipkowitz S. Triple Negative Breast Cancer Cell Lines: One Tool in the Search for Better Treatment of Triple Negative Breast Cancer. *Breast Dis.* **2010**;32(1–2):35–48.

Chilakamarthi U, Giribabu L. Photodynamic Therapy: Past, Present and Future. *Chem. Rec.* **2017**;17(8):775–802.

Cunderlíková B, Gangeskar L, Moan J. Acid-base properties of chlorin e6: relation to cellular uptake. *J. Photochem. Photobiol. B.* **1999**;53(1–3):81–90.

Dai Q, Wilhelm S, Ding D, Syed AM, Sindhwani S, Zhang Y ir kt. Quantifying the Ligand-Coated Nanoparticle Delivery to Cancer Cells in Solid Tumors. *ACS Nano*. **2018**;12(8):8423–35.

Dapkute D, Steponkiene S, Bulotiene D, Saulite L, Riekstina U, Rotomskis R. Skin-derived mesenchymal stem cells as quantum dot vehicles to tumors. *Int. J. Nanomedicine*. **2017**;12:8129–42.

Dapkute D, Pleckaitis M, Bulotiene D, Daunoravicius D, Rotomskis R, Karabanovas V. Hitchhiking Nanoparticles: Mesenchymal Stem Cell-Mediated Delivery of Theranostic Nanoparticles. *ACS Appl. Mater. Interfaces*. **2021,** accepted.

D'Arcy MS. Cell death: a review of the major forms of apoptosis, necrosis and autophagy. *Cell Biol. Int.* **2019**;43(6):582–92.

DeRosa MC, Crutchley RJ. Photosensitized singlet oxygen and its applications. *Coord. Chem. Rev.* **2002**;233–234:351–71.

Dhillon SS, Demmy TL, Yendamuri S, Loewen G, Nwogu C, Cooper M ir kt. A Phase I Study of Light Dose for Photodynamic Therapy Using 2-[1-Hexyloxyethyl]-2 Devinyl Pyropheophorbide-a for the Treatment of Non-Small Cell Carcinoma In Situ or Non-Small Cell Microinvasive Bronchogenic Carcinoma: A Dose Ranging Study. *J. Thorac. Oncol. Off. Publ. Int. Assoc. Study Lung Cancer*. **2016**;11(2):234–41.

Dillekås H, Rogers MS, Straume O. Are 90% of deaths from cancer caused by metastases? *Cancer Med.* **2019**;8(12):5574–6.

Dominici M, Le Blanc K, Mueller I, Slaper-Cortenbach I, Marini FC, Krause DS ir kt. Minimal criteria for defining multipotent mesenchymal stromal cells. The International Society for Cellular Therapy position statement. *Cytotherapy*. **2006**;8(4):315–7.

Dougherty TJ, Gomer CJ, Henderson BW, Jori G, Kessel D, Korbelik M ir kt. Photodynamic therapy. *J. Natl. Cancer Inst.* **1998**;90(12):889–905.

Durymanov MO, Rosenkranz AA, Sobolev AS. Current Approaches for Improving Intratumoral Accumulation and Distribution of Nanomedicines. *Theranostics*. **2015**;5(9):1007–20.

Ferreira LP, Gaspar VM, Mano JF. Bioinstructive microparticles for self-assembly of mesenchymal stem Cell-3D tumor spheroids. *Biomaterials*. **2018**;185:155–73.

Hmadcha A, Martin-Montalvo A, Gauthier BR, Soria B, Capilla-Gonzalez V. Therapeutic Potential of Mesenchymal Stem Cells for Cancer Therapy. *Front. Bioeng. Biotechnol.* **2020**;8.

Huang Z. A Review of Progress in Clinical Photodynamic Therapy. *Technol. Cancer Res. Treat.* **2005**;4(3):283–93.

Huang Z, Yu P, Tang J. Characterization of Triple-Negative Breast Cancer MDA-MB-231 Cell Spheroid Model. *OncoTargets Ther.* **2020**;13:5395–405.

Yao J, Li P, Li L, Yang M. Biochemistry and biomedicine of quantum dots: from biodetection to bioimaging, drug discovery, diagnostics, and therapy. *Acta Biomater.* **2018**;74:36–55.

Ye L, Hu R, Liu L, Liu J, Liu J, Chen H ir kt. Comparing Semiconductor Nanocrystal Toxicity in Pregnant Mice and Non-Human Primates. *Nanotheranostics*. **2019**;3(1):54–65.

Yong K-T, Law W-C, Hu R, Ye L, Liu L, Swihart MT ir kt. Nanotoxicity assessment of quantum dots: from cellular to primate studies. *Chem. Soc. Rev.* The Royal Society of Chemistry; **2013**;42(3):1236–50.

Yu TTL, Gupta P, Ronfard V, Vertès AA, Bayon Y. Recent Progress in European Advanced Therapy Medicinal Products and Beyond. *Front. Bioeng. Biotechnol.* **2018**;6.

Jarockyte G, Dapkute D, Karabanovas V, Daugmaudis JV, Ivanauskas F, Rotomskis R. 3D cellular spheroids as tools for understanding carboxylated quantum dot behavior in tumors. *Biochim. Biophys. Acta BBA - Gen. Subj.* **2018**;1862(4):914–23.

Kim S, Fujitsuka M, Majima T. Photochemistry of singlet oxygen sensor green. *J. Phys. Chem. B.* **2013**;117(45):13985–92.

Kundrotas G, Karabanovas V, Pleckaitis M, Juraleviciute M, Steponkiene S, Gudleviciene Z ir kt. Uptake and distribution of carboxylated quantum dots in human mesenchymal stem cells: cell growing density matters. *J. Nanobiotechnology*. **2019**;17.

Ladewig J, Koch P, Brüstle O. In vitro Migration Assays for Neural Stem Cells, Intermediate Neurogenic Progenitors and Immature Neurons. *Bio-Protoc.* **2015**;5(1):e1371–e1371.

Lee H-Y, Hong I-S. Double-edged sword of mesenchymal stem cells: Cancer-promoting versus therapeutic potential. *Cancer Sci.* **2017**;108(10):1939–46.

Levy O, Kuai R, Siren EMJ, Bhere D, Milton Y, Nissar N ir kt. Shattering barriers toward clinically meaningful MSC therapies. *Sci. Adv.* American Association for the Advancement of Science; **2020**;6(30):eaba6884.

Li J, Ezzelarab MB, Cooper DKC. Do mesenchymal stem cells function across species barriers? Relevance for xenotransplantation. *Xenotransplantation*. **2012**;19(5):273–85.

Liu C, Feng X, Wang B, Wang X, Wang C, Yu M ir kt. Bone marrow mesenchymal stem cells promote head and neck cancer progression through Periostin-mediated phosphoinositide 3-kinase/Akt/mammalian target of rapamycin. *Cancer Sci.* **2018**;109(3):688–98.

Lucky SS, Soo KC, Zhang Y. Nanoparticles in Photodynamic Therapy. *Chem. Rev.* American Chemical Society; **2015**;115(4):1990–2042.

Martynenko IV, Kuznetsova VA, Orlova AO, Kanaev PA, Maslov VG, Loudon A ir kt. Chlorin e6–ZnSe/ZnS quantum dots based system as reagent for photodynamic therapy. *Nanotechnology*. IOP Publishing; **2015**;26(5):055102.

McMillan J, Batrakova E, Gendelman HE. Cell Delivery of Therapeutic Nanoparticles. *Prog. Mol. Biol. Transl. Sci.* **2011**;104:563–601.

Melzer C, Yang Y, Hass R. Interaction of MSC with tumor cells. *Cell Commun. Signal.* **2016**;14(1):20.

Momin EN, Mohyeldin A, Zaidi HA, Vela G, Quiñones-Hinojosa A. Mesenchymal stem cells: new approaches for the treatment of neurological diseases. *Curr. Stem Cell Res. Ther.* **2010**;5(4):326–44.

Nakamizo A, Marini F, Amano T, Khan A, Studeny M, Gumin J ir kt. Human Bone Marrow–Derived Mesenchymal Stem Cells in the Treatment of Gliomas. *Cancer Res.* American Association for Cancer Research; **2005**;65(8):3307–18.

Nedeljković M, Damjanović A. Mechanisms of Chemotherapy Resistance in Triple-Negative Breast Cancer—How We Can Rise to the Challenge. *Cells*. Multidisciplinary Digital Publishing Institute; **2019**;8(9):957.

Pietilä M, Lehenkari P, Kuvaja P, Kaakinen M, Kaul SC, Wadhwa R ir kt. Mortalin antibody-conjugated quantum dot transfer from human

mesenchymal stromal cells to breast cancer cells requires cell–cell interaction. *Exp. Cell Res.* **2013**;319(18):2770–80.

Polo E, Collado M, Pelaz B, del Pino P. Advances toward More Efficient Targeted Delivery of Nanoparticles in Vivo: Understanding Interactions between Nanoparticles and Cells. *ACS Nano*. American Chemical Society; **2017**;11(3):2397–402.

Redmond RW, Kochevar IE. Spatially resolved cellular responses to singlet oxygen. *Photochem. Photobiol.* **2006**;82(5):1178–86.

Ryman-Rasmussen JP, Riviere JE, Monteiro-Riviere NA. Variables Influencing Interactions of Untargeted Quantum Dot Nanoparticles with Skin Cells and Identification of Biochemical Modulators. *Nano Lett.* American Chemical Society; **2007**;7(5):1344–8.

Rodini CO, Gonçalves da Silva PB, Assoni AF, Carvalho VM, Okamoto OK. Mesenchymal stem cells enhance tumorigenic properties of human glioblastoma through independent cell-cell communication mechanisms. *Oncotarget*. **2018**;9(37):24766–77.

Røsland GV, Svendsen A, Torsvik A, Sobala E, McCormack E, Immervoll H ir kt. Long-term cultures of bone marrow-derived human mesenchymal stem cells frequently undergo spontaneous malignant transformation. *Cancer Res.* **2009**;69(13):5331–9.

Samia ACS, Chen X, Burda C. Semiconductor Quantum Dots for Photodynamic Therapy. *J. Am. Chem. Soc.* American Chemical Society; **2003**;125(51):15736–7.

Saulite L, Dapkute D, Pleiko K, Popena I, Steponkiene S, Rotomskis R ir kt. Nano-engineered skin mesenchymal stem cells: potential vehicles for tumour-targeted quantum-dot delivery. *Beilstein J. Nanotechnol.* Beilstein-Institut; **2017**;8(1):1218–30.

Saulite L, Pleiko K, Popena I, Dapkute D, Rotomskis R, Riekstina U. Nanoparticle delivery to metastatic breast cancer cells by nanoengineered mesenchymal stem cells. *Beilstein J. Nanotechnol.* Beilstein-Institut; **2018**;9(1):321–32.

Shyamala K, Girish HC, Murgod S. Risk of tumor cell seeding through biopsy and aspiration cytology. *J. Int. Soc. Prev. Community Dent.* **2014**;4(1):5–11.

Sindhwani S, Syed AM, Ngai J, Kingston BR, Maiorino L, Rothschild J ir kt. The entry of nanoparticles into solid tumours. *Nat. Mater.* Nature Publishing Group; **2020**;19(5):566–75.

Singh B, Mitragotri S. Harnessing cells to deliver nanoparticle drugs to treat cancer. *Biotechnol. Adv.* **2020**;42:107339.

Skripka A, Dapkute D, Valanciunaite J, Karabanovas V, Rotomskis R. Impact of Quantum Dot Surface on Complex Formation with Chlorin e6 and Photodynamic Therapy. *Nanomaterials*. **2018**;9(1).

Steponkiene S, Valanciunaite J, Skripka A, Rotomskis R. Cellular Uptake and Photosensitizing Properties of Quantum Dot-Chlorin e6 Complex: In Vitro Study. *J. Biomed. Nanotechnol.* **2014**;10(4):679–86.

Sung H, Ferlay J, Siegel RL, Laversanne M, Soerjomataram I, Jemal A ir kt. Global cancer statistics 2020: GLOBOCAN estimates of incidence and mortality worldwide for 36 cancers in 185 countries. *CA. Cancer J. Clin.* **2021**;

Torsvik A, Røsland GV, Svendsen A, Molven A, Immervoll H, McCormack E ir kt. Spontaneous Malignant Transformation of Human Mesenchymal Stem Cells Reflects Cross-Contamination: Putting the Research Field on Track – Letter. *Cancer Res.* American Association for Cancer Research; **2010**;70(15):6393–6.

Triesscheijn M, Baas P, Schellens JHM, Stewart FA. Photodynamic Therapy in Oncology. *The Oncologist*. **2006**;11(9):1034–44.

Valanciunaite J, Klymchenko AS, Skripka A, Richert L, Steponkiene S, Streckyte G ir kt. A non-covalent complex of quantum dots and chlorin e6: efficient energy transfer and remarkable stability in living cells revealed by FLIM. *RSC Adv.* The Royal Society of Chemistry; **2014**;4(94):52270–8.

Wang TD, Van Dam J. Optical biopsy: A new frontier in endoscopic detection and diagnosis. *Clin. Gastroenterol. Hepatol.* **2004**;2(9):744–53.

Xiao W, Gao H. The impact of protein corona on the behavior and targeting capability of nanoparticle-based delivery system. *Int. J. Pharm.* **2018**;552(1):328–39.

Xu G, Lin G, Lin S, Wu N, Deng Y, Feng G ir kt. The Reproductive Toxicity of CdSe/ZnS Quantum Dots on the in vivo Ovarian Function and in vitro Fertilization. *Sci. Rep.* Nature Publishing Group; **2016**;6(1):37677.

REZULTATŲ VIEŠINIMAS

Žodiniai pranešimai, tiesiogiai susiję su disertacijos tema:

1. Saulīte L, **Dapkute D**, Plūduma S, Rotomskis R, Riekstiņa U. Quantum Dot Transfer from Mesenchymal Stem Cells to Breast Cancer Cells in 3D Co-Culture Model. 75th Conference of the University of Latvia. 2017 m. vasario 24, Ryga, Latvija. Tezių knyga 88 p.
2. **Dapkutė D**, Steponkienė S, Rotomskis R. Mezenchiminių ir vėžinių kamieninių ląstelių atsakas į nanodalelių poveikį. Lietuvos Nacionalinė Fizikos Konferencija 2017 (LNFK42). 2017 m. spalio 4-6, Vilnius, Lietuva. Tezių knyga 78 p.
3. Jarockytė G, **Dapkutė D**, Karabanovas V, Daugmaudis JV, Ivanauskas F, Rotomskis R. 3D sferoidinių ląstelių kultūrų pritaikymas priešvėžinių vaistų tyrimuose. Lietuvos Nacionalinė Fizikos Konferencija 2017 (LNFK42). 2017 m. spalio 4-6, Vilnius, Lietuva. Tezių knyga 94 p.
4. **Dapkute D**, Karabanovas V, Rotomskis R. Stem Cell-Based Delivery of Theranostic Nanoparticles to Cancer Cells. Baltic Biophysics Conference. 2018 m. spalio 4-5, Kaunas, Lietuva. Tezių knyga 24 p.
5. **Dapkute D**, Skripka A, Valanciunaite J, Karabanovas V, Rotomskis R. Hitchhiking Nanoparticles: Prospects of Stem Cell Use in Cancer Theranostics. Current Trends in Cancer Theranostics 2019 (CTCT-5.0). 2019 m. birželio 30-liepos 4, Trakai, Lietuva. Tezių knyga 51 p.
6. Karabanovas V, Skripka A, Jarockytė G, **Dapkutė D**, Vetrone F, Rotomskis R. Daugiafunkcės nanomedžiagos navikų teranostikai. 43-oji Lietuvos nacionalinė fizikos konferencija (LNFK43). 2019 m. spalio 3-5, Kaunas, Lietuva. Tezių knyga 34 p.
7. **Dapkute D**. Kamieninės ląstelės – ląsteliniai „Trojos arkliai“ teranostinėms nanodalelėms pernešti. 12-oji jaunųjų mokslininkų konferencija Bioateitis: gamtos ir gyvybės mokslų perspektyvos. 2019 m. gruodžio 11, Kaunas, Lietuva. Tezių knyga 14 p.
8. **Dapkute D.** Hitching a Ride: Stem Cell-Based Delivery of Theranostic Nanoparticles. 2nd Baltic Biophysics conference. 2020 m. spalio 15, virtuali konferencija. *Kviestinis pranešėjas*
9. **Dapkute D**. Hitching a ride: Mesenchymal stem cell-based delivery of nanoparticles. Lietuvos kamieninių ląstelių tyrėjų asociacijos

organizuota VI tarptautinė konferencija. 2020 m. lapkričio 20, virtuali konferencija. *Kviestinis pranešėjas*

Stendiniai pranešimai, tiesiogiai susiję su disertacijos tema:

1. **Dapkute D**, Steponkiene S, Saulite L, Riekstina U, Rotomskis R. Antibody-conjugated quantum dots and nanoparticle-loaded mesenchymal stem cells for targeting cancer stem cells. European Technology Platform on Nanomedicine (ETPN2017). 2017 m. spalio 17-19, Malaga, Ispanija. *Išvykai gautas finansavimas iš MITA*.
2. **Dapkute D**, Steponkiene S, Karabanovas V, Rotomskis R. Mesenchymal stem cell-mediated theranostic delivery system. Current Trends in Cancer Theranostics 2018 (CTCT2018). 2018 m. liepos 1-5, Trakai, Lietuva. Tezių knyga 82 p.
3. Jarockyte G, **Dapkute D**, Karabanovas V, Daugmaudis JV, Ivanauskas F, Rotomskis R. 3D cellular spheroids as tools for understanding carboxylated quantum dot behavior in tumors. Current Trends in Cancer Theranostics 2018 (CTCT2018). 2018 m. liepos 1-5, Trakai, Lietuva. Tezių knyga 88 p.
4. **Dapkute D**, Steponkiene S, Karabanovas V, Rotomskis R. Mesenchymal stem cells as delivery vehicles of photosensitizer functionalized nanoparticles: cell therapy meets nanotechnology. Nanotexnology: 15^{th} international conference on Nanosciences & Nanotechnologies/12^{th} international summer schools on Nanosciences & Nanotechnologies, Organic Electronics & Nanomedicine. 2018 m. birželio 30-liepos 7, Salonikai, Graikija. Tezių knygos 235/31 p. *Laimėta stipendija dalyvauti vasaros stovykloje/konferencijoje iš LMT.*
5. **Dapkute D**, Karabanovas V, Rotomskis R. Fotosensibilizatoriumi funkcionalizuotos nanodalelės ir kamieninės ląstelės vėžio teranostikoje. 43-oji Lietuvos nacionalinė fizikos konferencija (LNFK43). 2019 m. spalio 3-5, Kaunas, Lietuva. Tezių knyga 128 p.

Stendiniai pranešimai, tiesiogiai nesusiję su disertacijos tema:

1. Grube M , Shvirksts K, **Dapkute D**, Matulionyte M, Rotomskis R. FTIR Spectroscopy Studies of Breast Cancer Cell Response to Incubation with BSA or Au-BSA Nanoclusters. 3rd Congress of

Baltic Microbiologists 2016 (CMB2016). 2016 m. spalio 18-21, Vilnius, Lietuva. Tezių knyga 69 p.

2. **Dapkute D**, Matulionyte M, Budenaite L, Jarockyte G, Rotomskis R. Photoluminescent gold nanoclusters in cancer cells: cellular uptake, toxicity, and generation of reactive oxygen species. Current Trends in Cancer Theranostics 2017 (CTCT2017). 2017 m. birželio 25-29, Pakruojis, Lietuva. Tezių knyga 57 p.
3. Mazeika V, **Dapkute D**, Skripka A, Marin R, Vetrone F, Canton P, Rotomskis R, Karabanovas V. Biocompatible and Heavy Metal Free $CuInS_2$/ZnS Quantum Dots for Cancer Diagnostics. Open Readings 2019. 2019 m. kovo 19-22, Vilnius, Lietuva. Tezių knyga 243 p.
4. Mažeika V, **Dapkutė D**, Skripka A, Marin R, Vetrone F, Canton P, Karabanovas V. Biologiškai suderinami CuInS2/ZnS kvantiniai taškai vėžio diagnostikai. 43-oji Lietuvos nacionalinė fizikos konferencija (LNFK43). 2019 m. spalio 3-5, Kaunas, Lietuva. Tezių knyga 120 p.

Finansinė parama

Moksliniai tyrimai buvo iš dalies finansuoti Lietuvos mokslo tarybos (LMT) Lietuvos-Latvijos-Taivano (Kinijos Respublika) programa (TAP LLT 03/2014, Nr. V-273) ir L‘Oréal-UNESCO (bendradarbiaujant su Lietuvos mokslo akademija) „Moterims moksle“ programa.

Išlaidas, susijusias su dalyvavimu tarptautinėse konferencijose, iš dalies padengė LMT Parama akademinei išvykai gauti (Reg. Nr. P-DAK-18-149) (konferencija-vasaros mokykla Salonikuose, Graikijoje).

Autorė taip pat dukart paremta LMT Parama doktorantams už akademinius pasiekimus (Reg. Nr. P-DAP-18-233 ir P-DAP-19-287).

CURRICULUM VITAE

Vardas, Pavardė	Dominyka Dapkutė
Išsilavinimas/Kvalifikacija	
2006-2010	Vilniaus Užupio gimnazija
2010-2014	Vilniaus universitetas, Gamtos mokslų fakultetas. Kvalifikacija: Molekulinės biologijos bakalauras
2014-2016	Vilniaus universitetas, Gamtos mokslų fakultetas. Kvalifikacija: Molekulinės biologijos magistras
2016-2020	Vilniaus universitetas, Gyvybės mokslų centras, Biomokslų institutas. Biofizikos doktorantūra.
Darbo patirtis	
2014-2016	Inžinierė Nacionalinio vėžio instituto Biomedicininės fizikos laboratorijoje
2014-2016	Biofizikė Nacionalinio vėžio instituto Biomedicininės fizikos laboratorijoje
Nuo 2016	Jaunesnioji mokslo darbuotoja Nacionalinio vėžio instituto Biomedicininės fizikos laboratorijoje
2018-2021	Mokslinių tyrimų ir plėtros skyriaus specialistė UAB „Valentis“

Dalyvavimas moksliniuose projektuose

Bendros Lietuvos-Latvijos-Kinijos (Taivanas) mokslinių tyrimų programos projektas “Mezenchiminių kamieninių ir vėžinių kamieninių ląstelių atsakas į nanodalelių poveikį” (TAP LLT 03/2014, Nr. V-273).

Sertifikatai, apdovanojimai, stipendijos

2017 03	Lietuvos mokslų akademijos (LMA) Aukštųjų mokyklų studentų mokslinių darbų konkurso premija už darbą

	„Kvantinių taškų poveikis mezenchiminėms kamieninėms ląstelėms“.
2017-2018	„Laboratorinių (bandomųjų) gyvūnų mokslo“ kursas (trukmė – 80 val.), gautas pažymėjimas, suteikiantis teisę savarankiškai planuoti ir atlikti eksperimentus su bandomaisiais gyvūnais pagal 2010/63/ES Europos Parlamento ir Tarybos Direktyvos 23 straipsnį.
2017-2018, 2018-2019	Parama doktorantams už akademinius pasiekimus, skiriama LMT.
2018 03, 2019 03, 2019 10	Vilniaus universiteto vienkartinė tikslinė stipendija už mokslinę veiklą.
2019 11	Vilniaus universiteto Gyvybės mokslų centro vardinė stipendija už aktyvią mokslinę, mokslo populiarinimo ir organizacinę veiklą.
2020 06	„L’Oréal Baltic“ programos „Moterims moksle“ (įgyvendinama bendradarbiaujant su LMA ir Lietuvos nacionaline UNESCO komisija) laureatė.
2020 11	Geros klinikinės praktikos pagrindų mokymai Santaros klinikose (trukmė – 8 val.).

PADĖKA

Dėkoju savo darbo vadovui prof. habil. dr. Ričardui Rotomskiui už prieš 9 metus suteiktą galimybę atlikti praktiką Biomedicininės fizikos laboratorijoje. Didelis ačiū jam ir visam laboratorijos kolektyvui už įdiegtas praktines žinias, patarimus, mokslines konsultacijas ir diskusijas.

Dėkoju savo pirmųjų darbų vadovei dr. Simonai Steponkienei už pagalbą žengiant pirmuosius žingsnius šiame sudėtingame mokslininko kelyje ir už visas suteiktas galimybes tobulėti karjeros srityje.

Atskira padėka dr. Vitalijui Karabanovui už įkvėpimą ir mokslines idėjas ir Marijui Plečkaičiui už moralinį palaikymą, pagalbą atliekant tyrimus ir analizuojant rezultatus, stiliaus korekcijas bei tekstų redagavimą.

Ačiū mamai už kantrybę ir paskatinimą siekti aukštumų. Ačiū, kad neleidai pasiduoti ir motyvavai eiti pirmyn.

Aidai, ačiū už bendrą meilę mokslui, supratimą, kantrybę ir racionalų optimizmą.

Tikiu, kad visi kartu galime nuversti kalnus.

1. Saulite L, **Dapkute D**, Pleiko K, Popena I, Steponkiene S, Rotomskis R, Riekstina U. *Nano-engineered skin mesenchymal stem cells: potential vehicles for tumour-targeted quantum-dot delivery*. Beilstein Journal of Nanotechnology. 2017, 8:1218-1230. https://doi.org/10.3762/bjnano.8.123.
2. **Dapkute D**, Steponkiene S, Bulotiene D, Saulite L, Riekstina U, Rotomskis R. *Skin-derived mesenchymal stem cells as quantum dot vehicles to tumors*. International Journal of Nanomedicine. 2017, 2017:12, 8129–8142. https://doi.org/10.2147/IJN.S143367.
3. Saulite L, Pleiko K, Popena I, **Dapkute D**, Rotomskis R, Riekstina U. *Nanoparticle delivery to metastatic breast cancer cells by nanoengineered mesenchymal stem cells*. Beilstein Journal of Nanotechnology. 2018, 9:321–332. https://doi.org/10.3762/bjnano.9.32.
4. Jarockyte G, **Dapkute D**, Karabanovas V, Daugmaudis JV, Ivanauskas F, Rotomskis R. *3D cellular spheroids as tools for understanding carboxylated quantum dot behavior in tumors.* BBA General Subjects. 2018, 1862:914–923. https://doi.org/10.1016/j.bbagen.2017.12.014.
5. Skripka A, **Dapkute D**, Valanciunaite J, Karabanovas V, Rotomskis R. *Impact of Quantum Dot Surface on Complex Formation with Chlorin e6 and Photodynamic Therapy*. Nanomaterials. **2019**, 9(1), 9. https://doi.org/10.3390/nano9010009.
6. **Dapkute D**, Pleckaitis M, Bulotiene D, Daunoravicius D, Rotomskis R, Karabanovas V. *Hitchhiking nanoparticles: mesenchymal stem cell-mediated delivery of theranostic nanoparticles.* ACS Applied Materials & Interfaces. **2021** (priimtas/accepted).

Autorės indėlis: Autorė parašė antrą ir šeštą publikacijas. Pirmoji, ketvirtoji ir penktoji publikacija – kartu su bendraautoriais sudarė eksperimentų planą, atliko dalį visų eksperimentų, konsultavo bendraautorius atliekant kitas eksperimentines procedūras, rašė dalį straipsnio, dalyvavo kituose straipsnio rengimo etapuose. Autorė prisidėjo prie trečiosios publikacijos rengimo – su bendraautoriais formavo straipsnio idėją, sudarė eksperimentų planą, rašė dalį straipsnio.

Publikacijos ne disertacijos tema:

1. Matulionyte M, **Dapkute D**, Budenaite L, Jarockyte G, Rotomskis R. *Photoluminescent Gold Nanoclusters in Cancer Cells: Cellular Uptake, Toxicity, and Generation of Reactive Oxygen Species.* International Journal of Molecular Sciences **2017**, 18(2), 378. doi:10.3390/ijms18020378
2. Rinkunaite I, Simoliunas E, Alksne M, **Dapkute D**, Bukelskiene V. *Anti-inflammatory effect of different curcumin preparations on adjuvant-induced arthritis in rats*. BMC Complementary Medicine and Therapies **2021**, 21(1):39. doi:10.1186/s12906-021-03207-3.

1 publikacija / 1st publication

Nano-engineered skin mesenchymal stem cells: potential vehicles for tumour-targeted quantum-dot delivery

Saulite L, **Dapkute D**, Pleiko K, Popena I, Steponkiene S, Rotomskis R, Riekstina U.

Beilstein Journal of Nanotechnology **8**:1218-1230 (2017)

DOI: 10.3762/bjnano.8.123

BEILSTEIN JOURNAL OF NANOTECHNOLOGY

Nano-engineered skin mesenchymal stem cells: potential vehicles for tumour-targeted quantum-dot delivery

Liga Saulite*[1], Dominyka Dapkute[2,3], Karlis Pleiko[1], Ineta Popena[1], Simona Steponkiene[2], Ricardas Rotomskis[2,4] and Una Riekstina[1]

Full Research Paper

Open Access

Address:
[1]Faculty of Medicine, University of Latvia, Raina blvd. 19, LV-1586, Riga, Latvia, [2]Biomedical Physics Laboratory, National Cancer Institute, P. Baublio Street 3b, LT-08406 Vilnius, Lithuania, [3]Life Science Center, Vilnius University, Sauletekio al. 7, LT-10257, Vilnius, Lithuania and [4]Laser research center, Vilnius University, Sauletekio al. 9, corp. 3, LT-10222, Vilnius, Lithuania

Email:
Liga Saulite* - liga.saulite@lu.lv

* Corresponding author

Keywords:
endocytosis; mesenchymal stem cells; quantum dots; stem cell differentiation

Beilstein J. Nanotechnol. **2017,** *8,* 1218–1230.
doi:10.3762/bjnano.8.123

Received: 14 December 2016
Accepted: 10 May 2017
Published: 07 June 2017

This article is part of the Thematic Series "Nanomaterial-based cancer theranostics".

Guest Editor: V. Sivakov

Abstract

Nanotechnology-based drug design offers new possibilities for the use of nanoparticles in imaging and targeted therapy of tumours. Due to their tumour-homing ability, nano-engineered mesenchymal stem cells (MSCs) could be utilized as vectors to deliver diagnostic and therapeutic nanoparticles into a tumour. In the present study, uptake and functional effects of carboxyl-coated quantum dots QD655 were studied in human skin MSCs. The effect of QD on MSCs was examined using a cell viability assay, Ki67 expression analysis, and tri-lineage differentiation assay. The optimal conditions for QD uptake in MSCs were determined using flow cytometry. The QD uptake route in MSCs was examined via fluorescence imaging using endocytosis inhibitors for the micropinocytosis, phagocytosis, lipid-raft, clathrin- and caveolin-dependent endocytosis pathways. These data showed that QDs were efficiently accumulated in the cytoplasm of MSCs after incubation for 6 h. The main uptake route of QDs in skin MSCs was clathrin-mediated endocytosis. QDs were mainly localized in early endosomes after 6 h as well as in late endosomes and lysosomes after 24 h. QDs in concentrations ranging from 0.5 to 64 nM had no effect on cell viability and proliferation. The expression of MSC markers, CD73 and CD90, and hematopoietic markers, CD34 and CD45, as well as the ability to differentiate into adipocytes, chondrocytes, and osteocytes, were not altered in the presence of QDs. We observed a decrease in the QD signal from labelled MSCs over time that could partly reflect QD excretion. Altogether, these data suggest that QD-labelled MSCs could be used for targeted drug delivery studies.

Introduction

Despite remarkable advances in targeted therapies of various human malignancies, cancer is one of the leading causes of death worldwide [1]. Nanoparticles (NPs) could be linked to various drugs, thereby making them suitable for tumour imaging and targeted therapy [2]. However, the fact that NPs are quickly recognised by immune cells and cleared from the blood stream by reticuloendothelial system limits their utility as drug carriers [3]. Recent studies have shown that nano-engineered mesenchymal stem cells (MSCs) could be used as tumour-targeted therapeutic carriers, reflecting their tumour-homing capabilities [4-6].

MSCs are present in many tissues of the human body, including bone marrow, adipose tissues, skin and dental pulp. According to current understanding, MSCs are defined as adherent cells with a spindle-like morphology, expressing CD105 (SH2 or endoglin), CD73 (SH3 and SH4), CD106 (VCAM-1), CD44 (hyaluronic acid receptor), CD90 (Thy 1.1), CD29, CD146 and CD166 surface markers [7,8]. MSCs can be induced to differentiate in vitro into adipogenic, osteogenic, chondrogenic and myogenic cells. Moreover, other cell types, such as neurons, glial cells and smooth muscle cells, could be obtained from MSCs under the appropriate cell culture conditions [9,10].

Among the broad variety of investigated NPs, quantum dots (QDs) have demonstrated extensive application capabilities. High photostability and brightness, broad excitation and narrow fluorescence-emission spectra are some of the main properties required for the generation of new fluorescent nano-agents. The unique optical and electronic properties of QDs indicate their great potential in cancer diagnostics. The photoluminescence spectrum of carboxyl QD655 makes them ideal candidates for cancer theranostics as it overlaps with the optical transparency window of biological tissue [11]. Additionally, large and easily altered surfaces facilitate modifications of various NPs. These modifications increase the solubility of QDs to make QDs unnoticeable by the immune system, increase the QD half-life in the blood stream and target QDs to specific ligands or antigens [12]. Different therapeutic and recognition molecules can be attached to the surfaces of NPs and act synergistically [13,14]. QDs were also chosen for their applicability as resonant energy donors in photodynamic therapy. For example, the second-generation photosensitizer chlorin e6 has the absorption band at 654 nm and carboxyl QD655 would be excellent energy donors in such complexes. There were successful attempts to use a similar quantum dot–chlorin e6 complex in photodynamic cancer therapy [15]. Another study has shown that QDs, conjugated with antibodies against CD44, a marker of cancer stem-like cells, can be selectively engulfed by breast cancer cells [16]. Such surface modifications increase the potential of QDs for the use in targeted cancer diagnostics and therapies.

There is still doubt regarding the potential harmful effects of NPs or QDs on the differentiation capacity and self-renewal ability of adult stem cells. CdSe/ZnS QD labelling has been reported to adversely affect the osteogenesis and chondrogenesis capacities of bone marrow MSCs [17]. The impact of QD labelling on the biological properties of targeted stem cells, such as proliferation, cell cycle, and apoptosis, remains elusive. Therefore, further research on MSCs with regard to the delivery of QDs for monitoring and treating tumours is required.

Skin is the largest organ of the human body. It ensures the protection and insulation of the inner tissues [18] and also acts as a barrier against the penetration of QDs [19]. Nano-engineered skin MSCs could be used in cell-based skin cancer (SC) therapies [20,21]. MSCs loaded with anti-cancer drugs can reduce melanoma tumour growth in vivo, suggesting that these molecules are suitable vectors for therapeutic applications [22].

The aim of the present study was to analyse the accumulation, release, toxicity and functional effects of carboxyl QD655 on skin-derived MSCs to assess their potential use as vectors for the targeting of SC or other tumours.

Results

Optimal QD labelling conditions for MSCs

The concentration-dependent cytotoxicity of QDs was analysed in MSC cultures after 24 and 48 h using a colorimetric CCK-8 assay, which measures intracellular dehydrogenase activity (Figure 1). QDs did not significantly affect MSC viability after 24 or 48 h at any of the tested QD concentrations.

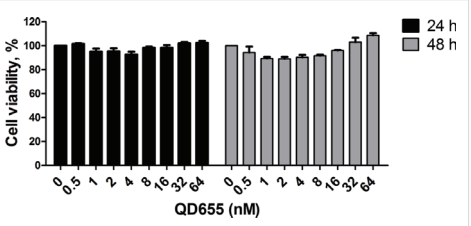

Figure 1: The concentration-dependent effect of QDs on the viability of MSCs. Viability was measured by a colorimetric assay (CCK-8) after incubation with QDs at 0.5–64 nM for 24 and 48 h.

In order to select the optimal incubation time for QD uptake in skin MSCs, cells were incubated with 16 nM QDs for time periods ranging from 15 min to 48 h (Figure 2a). The QD

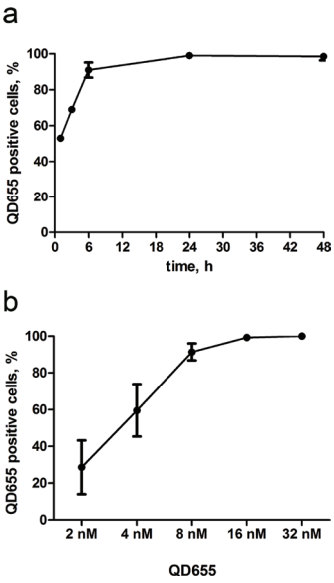

Figure 2: Evaluation of the optimal QD uptake conditions in skin MSCs. Time-dependent (a) and concentration-dependent (b) uptake dynamics in MSCs using flow cytometry analysis. The percentage of QD655-positive cells was obtained from the analysis of flow-cytometry histogram data.

uptake kinetics was calculated based on changes in fluorescence intensity. The plateau phase was reached after 24 h of incubation, consistent with observations in other cell lines [23]. The optimal incubation time for QD uptake was 6 h, after which up to 95% of the cells had incorporated QDs. Thus, a 6 h incubation time was used in all experiments, unless otherwise stated.

The optimal QD concentration for the uptake experiments was determined using serial dilutions of QDs from 2 up to 32 nM (Figure 2, b). The QD-positive cell number exponentially increased, and saturation was obtained at 16 nM, when cells were 99% QD-positive. Therefore, a 16 nM QD concentration was selected for further experiments, unless otherwise stated.

To determine whether MSCs release QDs in the environment after uptake, the supernatant was removed from cells after primary QD labelling. After rigorous rinsing, fresh complete or serum-free medium was applied to the QD-labelled cells. Next, the QD fluorescence intensity was determined in cells at 24 and 48 h after primary labelling. We observed a 30% decrease of the QD signal in cells propagated in complete medium and a 40% decrease of the QD signal under serum-free conditions after 24 h of incubation (Figure 3a). After 48 h, the number of QD-positive cells decreased even further in serum-free cultivated cells (Figure 3a). Supernatant from primarily QD-labelled MSCs was transferred to fresh MSCs for secondary labelling experiments. After 24 h, 3% of the cells in complete medium had taken up QDs, whereas under serum-free conditions, 7% of MSCs had taken up QDs in the secondary labelling experiments (Figure 3b). After 48 h QD uptake was detectable in approximately 1.5% of cells cultivated either in complete or serum-free medium (Figure 3b).

To determine the effect of cell division on the decrease of the QD signal, QD-labelled MSCs were propagated in complete and serum-free medium. Ki67 expression was clearly inhibited in cells cultivated in serum-free medium, which did not proliferate after 24 and 48 h, thereby excluding the probability of QD transfer to daughter cells (Figure 3c). Inhibition of proliferation was additionally confirmed by analysing the cell number in the respective medium (data not shown). The addition of QDs did not change the expression of Ki67 (data not shown).

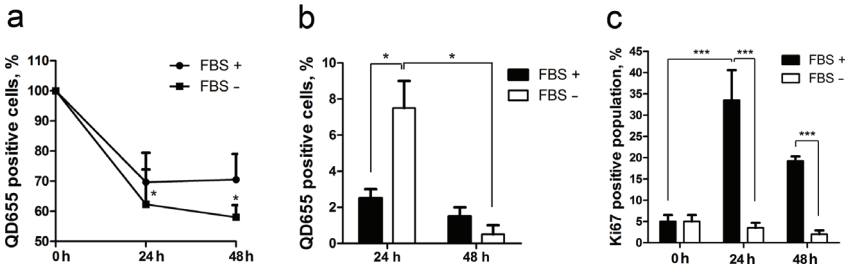

Figure 3: The release of QDs from MSCs. (a) QD loss in complete medium (FBS +) and serum-free medium (FBS −) after primary QD labelling (0 h) and 24 and 48 h after labelling. The statistical significance is shown in comparison to 0 h. (b) Secondary QD labelling of MSCs by supernatants from primarily labelled MSCs. (c) The comparison of Ki67 expression in complete and serum-free medium after labelling (0 h) and after 24 h and 48 h of cultivation; *p-value < 0.05, ***p-value < 0.001.

QD effect on immunophenotype, proliferation and differentiation of MSCs

The skin MSC population used in the present study was over 95% positive for MSC markers CD73 and CD90, whereas hematopoietic markers CD45 and CD34 were not expressed (Figure 4a). To estimate the effect of QDs on the MSC immunophenotype, expression of CD73 and CD90 was analysed after incubation with QDs for 48 h. Although CD105 is often used as a MSC marker together with CD73 and CD90, this marker was excluded from the analysis because of the fluorescence channel overlap with QDs (APC label, FL4). The data showed that QDs did not change the expression of CD73, CD90, CD34 and CD45 in MSCs (Figure 4a).

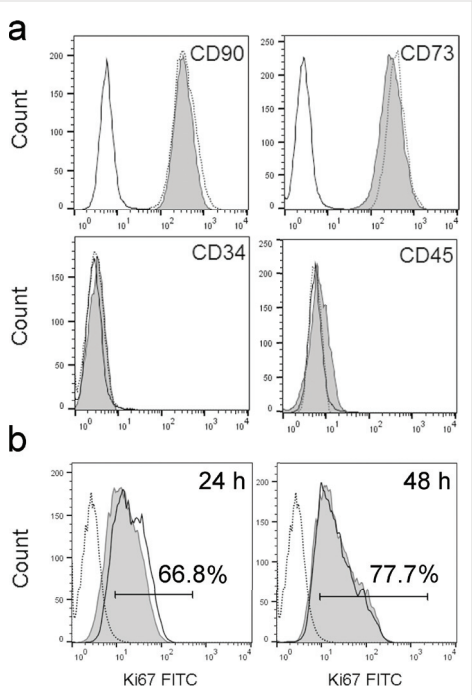

Figure 4: Representative data on the impact of QDs on immunophenotype and proliferation of MSCs. (a) Characterization of MSC markers CD90, CD73 and hematopoietic markers CD34 and CD45 in MSCs. Open histogram: unlabelled cells, dotted-line histogram: MSCs without QDs, grey histogram: QD-labelled MSCs. (b) Ki67 expression in MSCs after 24 h and 48 h of incubation with 16 nM QDs. Open histogram: unlabelled cells, dotted-line histogram: isotype control, grey histogram: QD-labelled cells.

The effect of QDs on proliferation was analysed based on Ki67 expression (Figure 4b). After incubation for 24 h, 67% of unlabelled and QD-labelled MSCs expressed the Ki67 marker. After 48 h, the Ki67-positive population increased to 78% in both cell populations. QDs did not show any effect on the proliferation of MSCs.

The differentiation of MSCs into adipocytes, chondrocytes and osteocytes was not affected by the presence of QDs (Figure 5). Quantification assays for Alcian Blue staining and Alizarin Red S staining confirmed that QDs did not influence chondrogenesis and osteogenesis of skin MSCs (Figure 6).

Analysis of the uptake pathway of QDs

MSCs were pre-treated with endocytosis inhibitors and subsequently labelled with QDs. The effect of serum proteins on the efficiency of QD uptake was analysed based on the comparison of QD uptake in complete and serum-free media (Figure 7). The effect of endocytosis inhibitors differed between complete and serum-free medium. In complete medium, a tendency of decreased QD uptake was observed using chlorpromazine (CPZ), an inhibitor of clathrin-mediated endocytosis (Figure 7a, c). In serum-free medium, QD uptake was significantly inhibited by CPZ and nystatin, an inhibitor of caveolin/lipid raft-mediated endocytosis (Figure 7b,d). In serum-free medium, the cells internalized more QDs according to the fluorescence intensity analysis (Figure 7c,d).

The intracellular localization of QDs after uptake was observed in BacMam 2.0-transfected MSCs. Excessive QD accumulation was initiated between 1 and 6 h. After 6 h, most of the QDs were localized in early endosomes (Figure 8) in both the cell periphery and perinuclear area. After 6 h, almost no QDs were localized in mature endosomes (data not shown). After 24 and 48 h, QD-containing early endosomes matured into late endosomes and lysosomes.

Discussion

Human MSCs have been widely investigated for their potential use in various therapeutic applications, due to their plasticity and migration ability. It has been proposed that MSC migration towards injury and inflammation sites could be used to deliver diagnostic and therapeutic nano-agents [24]. Studies on melanoma [25], prostate cancer [26], breast cancer [6] and lung cancer [27] have shown the ability of MSCs to home to cancer sites in vivo. In the tumour microenvironment, MSCs play a role in the formation of the tumour stroma and support cancer metastasis [28]. Lourenco et al. showed that MSC migration towards cancer cells is induced by MIF–CXCR4 chemotaxis [29]. Moreover, in close proximity of the tumour, cancer-associated fibroblast formation is induced by the release of vesicles containing miRNA from cancer cells. This leads to melanoma growth and invasion [30]. Therefore, skin-derived MSCs could serve as an appropriate model to study the stem cell (SC)

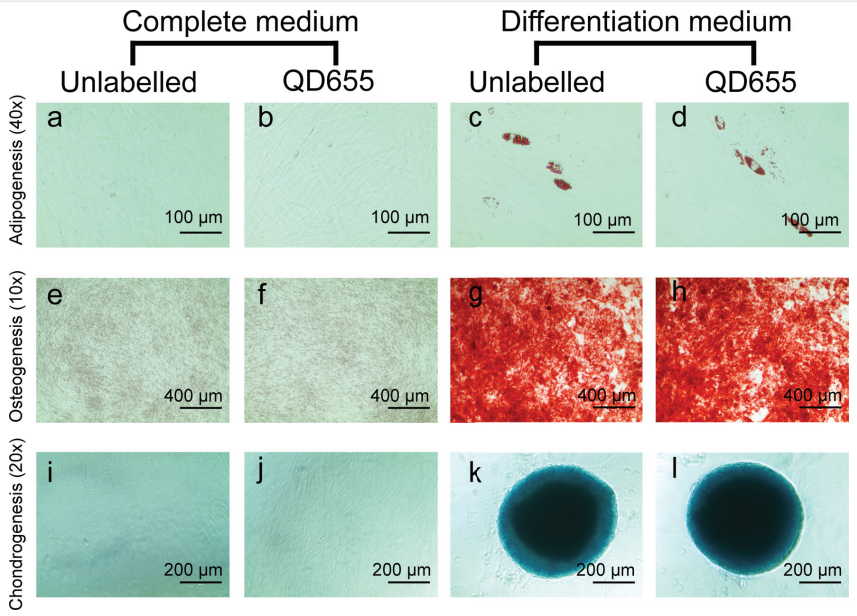

Figure 5: Differentiation of MSCs into adipocytes, chondrocytes and osteocytes. Oil Red O staining of cells in complete medium without (a) or with QD labelling (b); cells in adipogenesis medium without (c) or with QD labelling (d). Alizarin Red S staining on cells in complete medium in the absence or presence of QDs (e, f); cells in osteogenesis differentiation medium in the absence or presence of QDs (g, h). Alcian Blue staining on cells in complete medium (i, j) and chondrogenesis differentiation medium (k, l) in the absence or presence of QDs.

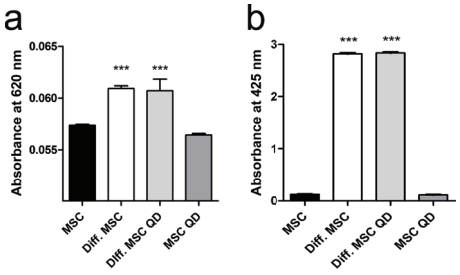

Figure 6: Quantification of osteogenesis and chondrogenesis in MSCs. Absorbance of Alizarin Red S (a) and Alcian Blue (b) extraction from MSC differentiation. Diff. MSC: differentiated MSCs, diff. MSC QD: differentiated MSCs labelled with QDs. Significance compared between differentiated and undifferentiated samples; ***p-value < 0.001.

tumour microenvironment and design SC-targeted therapeutics. In the present study, we addressed whether QD-loaded skin MSCs could serve as vectors to deliver NPs to cancer sites. To answer this question, the biological response of skin MSCs to QDs was investigated.

The results showed that QDs do not induce changes in immunophenotype, proliferation and viability of skin MSCs, indicating that QDs are biocompatible with MSCs. These results are consistent with those of studies on bone marrow mesenchymal stem cells and mouse embryonic stem cells, which show similar effects after QD labelling [31,32]. We observed variations in Ki67 expression in skin MSCs, regardless of QD addition, which might reflect the differences in donor age and passage number [33]. In the present study, we observed that QD labelling did not interfere with skin MSC differentiation into osteocytes, chondrocytes and adipocytes, and moreover, QDs did not induce spontaneous differentiation. Similarly, Shah et al. reported that carboxyl QDs do not alter the differentiation potential of human bone marrow stem cells [31]. Thus, QD-labelled MSCs are potentially safe to use in long-term tumour imaging and cell tracking experiments. Although there is a great deal of concern about the potential hazards of QDs containing heavy metals, the toxicity of QDs is a topic of controversy. The toxicity and ecotoxicity of QDs is studied at various levels of biological organization, from cell monolayers to primates and even ecosystems [34,35]. The potential toxicological effects of QDs are usually based on the release of free cadmium (Cd) [36]. However, QD shell and surface coatings

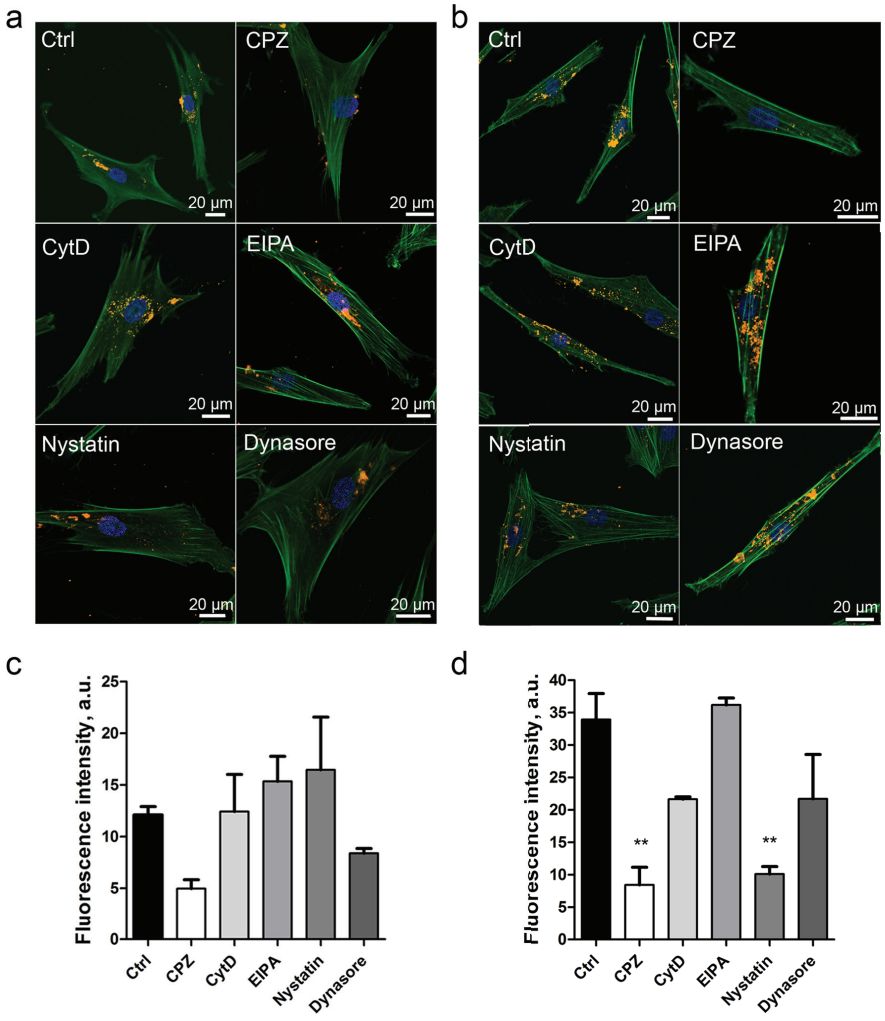

Figure 7: QD endocytic pathway in MSCs. QD uptake pathway in MSCs labelled with QDs in complete medium (a) or in serum-free medium (b). Uptake pathways were blocked using the endocytosis inhibitors CPZ, CytD, EIPA, nystatin and dynasore. Three overlaid channels represent Hoechst (blue), Phalloidin Alexa Fluor488 (green), carboxyl QD655 (yellow). Representative data are shown. QD fluorescence signal was quantified in complete (c) and in serum-free medium (d) cultivated MSCs. Statistical significance shown for the respective sample in comparison to control (Ctrl) sample; **p-value < 0.01.

protect the core, which contains toxic inorganic semiconductor materials. Unless coatings are damaged, QDs are mainly non-toxic [37]. Recently, Yaghini et al., by using non-photolytic visible wavelength excitation, have shown the formation of superoxide anion radicals by photoexcited CdSe/ZnS QDs [38]. Thus, the QDs may induce phototoxic reactions in labelled cells, which could be a desirable event in targeted tumour therapy.

The optimal uptake conditions for NPs could depend on the particle size, surface modifications, protein corona, and recipient cell line. Previous studies have suggested the incubation of

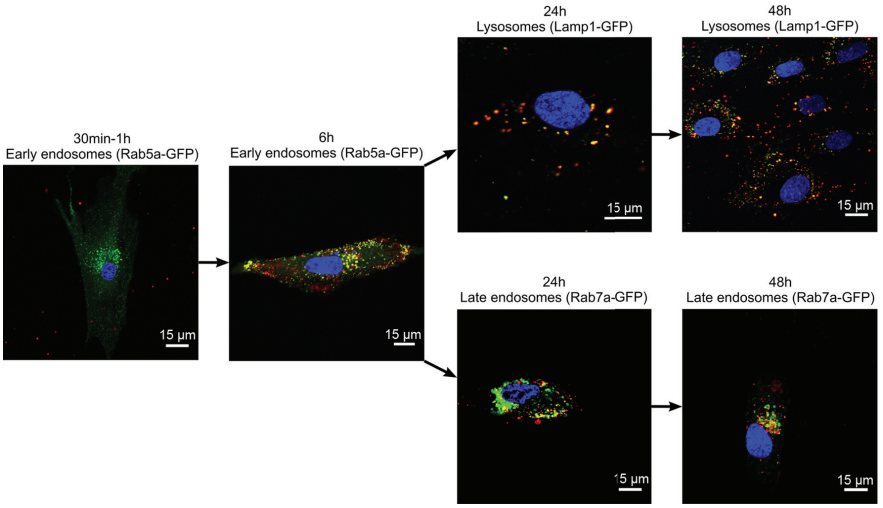

Figure 8: QD co-localization with endosomal compartments. Three overlaid channels represent the nucleus (blue), carboxyl QD655 (red) and Rab5a-GFP (early endosomes), Lamp1-GFP (lysosomes) or Rab7a-GFP (late endosomes) (green). Yellow colour demonstrates co-localization. Representative data are shown.

NIH3T3 mouse fibroblasts with 16 nM QDs for 6 h as the optimal conditions for cellular uptake experiments [39]. Given the lack of standardized NP uptake conditions in MSCs, we adjusted the protocol for QD uptake in human skin MSCs. The results showed that a 6 h incubation with 8 or 16 nM QDs is optimal for QD accumulation in more than 95% of the MSC population (Figure 2). Notably, a 1 h incubation with 5 nM and 20 nM QDs has previously been reported as sufficient for the labelling of rat bone marrow MSCs [40]. However, optimization of the NP incubation time and concentration is necessary in each individual experimental setting.

The uptake pathway of NPs varies depending on the cell and particle type. One of the factors affecting uptake is the protein corona that forms around NPs in serum-containing medium. Protein aggregates decrease gold NP uptake depending on size and cell type [41]. In the present study, we analysed the QD uptake pathways under both serum-containing and serum-free conditions. Selected inhibitors for the major uptake pathways were applied to cells prior to QD incubation. In serum-containing medium, decreased QD uptake in MSCs was observed after treatment with CPZ (Figure 7a,c). CPZ is an inhibitor of clathrin-mediated endocytosis through the anchoring of the clathrin and adaptor protein 2 (AP2) complex to endosomes, thereby preventing the assembly of coated pits at the inner plasma membrane [42]. In serum-free medium, QD uptake was decreased by CPZ and nystatin (Figure 7b,d). nystatin is an inhibitor of caveolin/lipid raft-mediated endocytosis, which disassembles caveloae and cholesterol in the membrane, but does not interfere with clathrin-mediated endocytosis [43]. Zhang et al. and Xiao et al. showed that dendritic cells and breast epithelial cells uptake carboxyl QDs via the clathrin-mediated pathway [44,45]. By contrast, experiments in HEK cells showed the uptake of carboxyl QDs through caveolin/lipid raft-mediated endocytosis; although it has been reported that caveolin-mediated endocytosis is the dominating uptake route in endothelial cells, smooth muscle cells and adipocytes [44,46]. Damalakiene et al. demonstrated that QDs possessing a protein corona are differently recognized by NIH3T3 cells and internalized by different pathways [23], consistent with the data from the present study. Interestingly, MSCs showed more effective internalization of QDs under serum-free conditions, as the protein corona interferes with QD uptake in skin MSCs. The composition of the protein corona could either enhance or decrease the cellular uptake of polystyrene-based NPs, depending on nanoparticle functionalization [47]. We have showed that NP uptake in skin MSCs is an active process and does not occur passively. For the development of cell-based tumour-targeted therapies, elucidation of the endocytic pathway is very important, because it may have an effect on the fate of QDs and/or QD-linked drugs within the cell. For example, after QD uptake by clathrin-mediated endocytosis, the QDs subsequently could be transferred to lysosomes for degradation or, depending on their surface coating, recycled to the cell surface [48]. On the contrary, QDs

taken up by caveolae-dependent endocytosis could bypass lysosomes and avoid lysosomal degradation [48]. Taken together, the accumulated experimental evidence suggests that the QD uptake pathway depends on the cell type, the formation of a protein corona and added functional groups on the NPs.

Intracellular localization of QDs in endosomes and lysosomes has been reported to be a common pathway following NP uptake through which particles are brought for lysosomal degradation [46,49]. We observed internalization of QDs in early endosomes after 6 h of incubation, followed by re-localization to late endosomes/lysosomes after 24 and 48 h of incubation (Figure 8). Cell division, excretion and degradation are the main mechanisms reported for QD signal elimination over time [50,51]. It has been implicated that the elimination rate depends on the particle size. Smaller NPs lead to faster elimination [50-52]. In the present study, we observed that the transfer of QDs to daughter cells during cell division is not the main mechanism involved in QD signal reduction in skin MSCs. Similar observations have been reported in the study of mouse embryonic stem cells, where QD loss was still detected after the inhibition of cell proliferation, suggesting that QDs might be excreted from cells [50]. Indeed, we demonstrated that MSCs could be repetitively labelled by the removal of supernatants from QD-loaded MSCs, confirming the presence of released QDs in the supernatant. After secondary labelling, the number of QD-positive MSCs was two times higher in serum-free medium compared to complete medium, likely indicating that the protein corona interferes with the QD uptake. Many types of stem cells have membrane transporters for the elimination of toxic reagents [53]. The induction of ABC transporter P-glycoprotein increases the elimination of QDs from HEK and HepG2 cells, while its inhibition demonstrated an opposite effect. The elimination rate was higher in HEK cells, because of the stem cell phenotype [54]. Expression of P-glycoprotein has also been reported in MSCs [4]. However, other data in mouse embryonic and kidney stem cells indicate that QD depletion likely occurs during cell division and that no excretion mechanisms could be observed [32]. Taken together, these data indicate that QD elimination mechanisms may be cell-type dependent. The results from skin MSCs demonstrated that the depletion of the QD signal over time could be explained by QD degradation and excretion. The fact that NPs are released from MSCs is important because of the intended use of MSCs as NP delivery vectors. We propose that cancer cell and MSC co-culture model could be used to demonstrate the applicability of QD-labelled MSCs for cancer theranostics. For example, Pietila et al. have demonstrated that direct cell–cell contact is required for QD–mortalin antibody transfer from nano-engineered MSCs to the breast cancer cell line MDA-MB-231 in vitro [55]. Alternatively, QDs or MSCs loaded with QD–drug conjugates could be used in melanoma xenograft models in vivo as was shown in a study by Studeny et al. where IFN-β-MSCs co-injected with a human melanoma cell line suppressed tumour growth in nude mice [25].

Altogether, we propose several reasons why QD-labelled skin MSCs could serve as a promising NP delivery vector. First, QD labelling would enable MSC tracking and visualization of the tumour microenvironment. Next, the cells in the tumour would take up the released QDs and then the formation of ROS could be induced through photoactivation, leading to cancer cell apoptosis. Last but not least, the secretion of sTNFR1 by skin MSCs could downregulate the pro-tumourigenic inflammatory responses [56-58].

Conclusion

Herein, we showed that carboxyl-coated QDs are biocompatible with skin MSCs. The proliferation, immunophenotype and differentiation potential of MSCs was not affected by QD accumulation in the cells. In the presence of serum, QDs were internalized in MSCs through clathrin-mediated endocytosis, whereas in the absence of serum, QD uptake occurs through the clathrin and caveolin/lipid raft-mediated endocytosis pathways. The loss of QD signal over time may possibly be explained by the excretion of QDs from MSCs, which could favour the use of MSCs as drug delivery vectors. These data validate the potential use of skin MSCs as NP delivery vectors for tumour-targeted therapies.

Experimental

Mesenchymal stem cell culture

Human skin samples were obtained from post-surgery materials with authorized approval from Research Ethics Committee, Institute of Experimental and Clinical Medicine, University of Latvia (issued 04.06.2014). Dermal MSC cultures were obtained as described elsewhere [59]. In brief, skin specimens were washed with cold phosphate-buffered saline (PBS), cut into 4–6 mm^2 pieces and incubated in 0.6 U/mL dispase (Roche, Switzerland) for 1–3 h at 37 °C to remove the epidermis. Dermis was minced manually before enzymatic digestion with 0.62 Wunsch U/mL Liberase Blendzyme 1 (Roche, Switzerland) for 30 min at 37 °C, then dissociated by vigorous pipetting and passed through a 70 μm cell strainer, followed by centrifugation at 400*g* for 5 min. The pellets were suspended in cultivation medium containing DMEM/F12 (3:1 v/v) supplemented with 10% of FBS and antibiotics (100 U/mL penicillin, 100 μg/mL streptomycin) (all from Sigma-Aldrich, USA). Cell suspensions were transferred into 25 cm^2 tissue culture flasks and grown until reaching 80% confluence in a humidified chamber at 37 °C with 5% CO_2. Cells were trypsinized with 0.25% trypsin–EDTA solution (Sigma-Aldrich,

USA). Cells at passages 2 to 5 were then frozen at −80 °C for long-term storage in a cell bank. All experiments were performed in compliance with the relevant laws and institutional guidelines. In this study five independent donor skin MSC cultures from passage 4 to passage 8 were used.

MSC surface marker analysis

Phenotyping of cell surface markers was performed by flow cytometry. The cells were stained with CD34-PE and CD45-FITC (all from BD Biosciences, USA), CD90-FITC (Dako, USA), CD73 PE (Abcam, USA) and isotype controls IgG1-FITC (Dako, USA), IgG1-PE (BD Biosciences, USA), and IgG2A-APC (BD Biosciences, USA). Flow cytometry data were acquired using a Guava EasyCyte 8HT flow cytometer and analysed using ExpressPro software (Merck Millipore, USA) comparing unlabelled, marker-labelled and isotype control populations in FL-1, FL-2 and FL-4 channels.

Quantum dots

Qdot® 655 ITK™ non-targeted carboxyl-coated quantum dots were purchased from Thermo Fisher Scientific, USA. QDs are composed of a CdSe core with a ZnS shell that are coated with amphiphilic polymers and functionalized with carboxylate. The QDs have an emission maximum at 655 nm. Xu et al. measured the hydrodynamic diameter of the nanoparticles to be 14.55 ± 4.157 nm and a zeta potential of −35.1 mV [60]. The stock solution is 8 µM in 50 mM borate, pH 9.0. Further preparations of the QD solution are described in each methodological part separately.

QD uptake dynamics using flow cytometry

To estimate the optimal QD concentration for uptake experiments, MSCs were seeded at a density of 5×10^4 cells per well in a 12-well tissue culture polystyrene plate and labelled with QDs at various concentrations in the range of 0.5 to 64 nM for 6 h in complete or serum-free medium. To determine the accumulation dynamics, 8 nM or 16 nM QDs were applied to MSCs and incubated for 0.5, 1, 3, 6, 24 and 48 h in complete medium. The cells were subsequently harvested by trypsinization, centrifuged at 250*g* for 5 min and resuspended in 200 µL of PBS. The samples were acquired on a Guava EasyCyte 8HT flow cytometer and analysed using ExpressPro software (Merck Millipore, USA) in channel FL4, comparing unlabelled and labelled cell populations.

Cell-viability assay

The impact of carboxyl-coated QD655 on the viability of MSCs was analysed using the Cell Counting Kit 8 (CCK-8) (Sigma-Aldrich, USA). A total of 5×10^3 cells per well were seeded onto 96-well plates in 100 µL of complete medium. The next day, QDs were added in serial dilutions at a twofold dilution in complete medium. The range of the tested QD concentrations ranged from 0.5–64 nM with twofold dilution. The cells were incubated with QDs for 24 and 48 h. QD untreated cells were used as a control, and the viability was defined as 100%. After incubation, 10 µL of CCK-8 reagent was added to each well and incubated for 2 h at 37 °C in 5% CO_2 at 90% humidity. The change in the medium colour corresponds to the amount of dye produced in the sample and is directly proportional to the number of viable cells. The optical density was measured using a spectrophotometer Bio-Tek *ELx808* (BioTek Instruments, USA) at a wavelength of 450 nm. The background signal of QDs from all of the tested concentrations was subtracted from the respective samples. Data were analysed in Microsoft Excel and GraphPad Prism software.

QD release assay

A total of 1×10^5 MSCs were first labelled with 16 nM QDs for 6 h in complete medium. After the primary labelling, the cell-culture supernatant was aspirated, the cells were rigorously rinsed and fresh complete or serum-free medium was added. The number of QD-positive cells was assessed using flow cytometry after 24 and 48 h. The supernatant of the primarily QD-labelled cells was collected at 24 and 48 h and subsequently applied to unlabelled cells for secondary labelling. After 24 h of incubation, the secondarily labelled cells were analysed using flow cytometry to evaluate the uptake of QD. To analyse the effect of proliferation on QD loss from the cells, QD labelled MSCs were propagated either in complete or serum-free medium and assessed for Ki67 expression (as described in method “MSC proliferation assay”) and QD signal using flow cytometry.

MSC proliferation assay

The effect of QD accumulation on the proliferation of MSCs was evaluated after 24 and 48 h of incubation using the FITC Mouse Anti-Ki67 Set according to the manufacturer’s instructions (BD Bioscience, USA). MSCs were seeded at a density of 5×10^4 cells per well onto 12-well plates in complete medium and allowed to adhere overnight. The medium was subsequently aspirated, and the wells were rinsed once with serum-free medium. The cells were serum-starved for 24 h to synchronize the cell cycle. Next, 16 nM of QDs in complete medium were added, and the cells were incubated for 24 or 48 h. Control wells contained cells in complete medium only. Subsequently, the cells were harvested by trypsinization, washed in PBS and centrifuged for 5 min at 250*g*. The cell pellet was fixed by suspending in 1 mL of 70% ice-cold ethanol. The samples were incubated at −20 °C for at least 2 h. The cells were subsequently washed twice with 9 mL of 1% FBS in PBS at 250*g* for 7 min. Cell pellets were resuspended in 100 µL of PBS, and 10 µL of FITC mouse anti-Ki-67 antibody and isotype control

IgG1-FITC were added to the cell suspension, mixed gently and incubated at room temperature for 30 min in the dark. After incubation, the cells were washed with 1 mL of PBS and centrifuged for 5 min at 300*g*. The pellet was suspended in 200 µL of PBS. Nonlabelled cells were used as a control to set the base line of Ki67 expression in MSCs. The isotype control was used to set the Ki67 negative population. The samples were analysed in channel FL-1 using flow cytometry.

Mesenchymal stem cell tri-lineage differentiation

MSCs were cultivated in complete medium up to 80% confluence. Differentiation into osteogenic, adipogenic and chondrogenic lineages was performed using StemPro Adipogenesis, Chondrogenesis, and Osteogenesis kits according to the manufacturer's instructions (all from ThermoFisher Scientific, USA). Briefly, for osteogenic differentiation, cells were seeded at a density of $1 \times 10^4/cm^2$ onto 24-well plates. Osteogenic differentiation medium was added; the medium was changed every three days over a period of 21 days. Spontaneous osteodifferentiation control samples were propagated in complete medium for 21 days. Adipogenic differentiation was performed after cultivating 1.82×10^4 cells in 24-well plates using adipogenic differentiation medium. The medium was changed every three days for 21 days. Spontaneous adipodifferentiation control samples were propagated in complete medium for 21 days. For the chondrogenic differentiation assay, 5 µL of a cell suspension with a density of 1.6×10^7 cells/mL in complete medium was seeded onto 96-well plates and incubated for 2 h under high-humidity conditions at 37 °C and 5% CO_2. Chondrogenic differentiation medium was added, and the medium was changed every three days for 14 days. Spontaneous chondrodifferentiation control samples were propagated in complete medium for 14 days.

Samples were incubated with 8 nM QDs in complete medium for 3 h before starting the differentiation assay. The QD concentration and incubation time were adjusted for the differentiation assay. After incubation with QDs, the medium was discarded, cells were washed with PBS and the relevant differentiation medium was added.

Evaluation of mesenchymal differentiation

Osteogenic differentiation was evaluated using Alizarin Red S staining. The cells were washed with 1 mL of PBS and fixed with 4% paraformaldehyde (PFA) at room temperature for 30 min. After fixation, the cells were washed two times with distilled water and stained with a 2% Alizarin Red S solution in water (pH adjusted to 4.2 with a 0.1% solution of NH_4OH) for 45 min at room temperature in the dark. Then, the stained cells were washed four times with 1 mL of distilled water and imaged using EVOS XL microscope (Invitrogen, USA). Samples stained with Alizarin Red S were extracted for quantitative measurements of osteogenic differentiation using 300 µL of 5% perchloric acid and gentle agitation for 10 min at room temperature. Subsequently 100 µL was transferred to a 96-well plate, and the absorbance was measured at 425 nm using an Infinite 200 PRO plate reader and i-control software (Tecan Trading AG, Switzerland).

Adipogenic differentiation was evaluated using Oil Red O staining. Cells were washed with PBS and fixed with 4% formaldehyde for 30 min at room temperature. After fixation, cells were washed with distilled water. Prior to staining, cells were incubated for 5 min at room temperature with 60% isopropanol and subsequently stained with 180 mg/L Oil Red O solution in isopropanol/water (3:2, v/v) for 15 min at room temperature. After staining, the cells were washed four to five times with distilled water and imaged.

Chondrogenic differentiation was evaluated using Alcian Blue staining. Cells were washed once with PBS and fixed with 4% PFA for 30 min at room temperature. After fixation, cells were washed with PBS and stained with a 1% Alcian Blue staining solution in 0.1 M HCl overnight at room temperature. Stained cells were washed three times with 0.1 M HCl and imaged in water.

Quantification of the Alcian Blue stain was achieved by solubilizing the stain in 50 µL of 6 M guanidine hydrochloride (Sigma-Aldrich, USA) overnight at room temperature. Absorbance was measured at 620 nm directly in a 96-well plate using an Infinite 200 PRO plate reader and i-control software.

Confocal microscopy

For confocal microscopy analysis, 1×10^4 cells per well were seeded on 8-well chamber slides (Nunc, Sigma-Aldrich, USA) in complete medium and left to adhere overnight at 37 °C, 5% CO2 and more than 90% humidity. 16 nM QDs diluted in complete medium were added, and samples were incubated from 15 min to 24 h. Control wells contained nonlabelled cells. After incubation, the medium was aspirated and each well was rinsed with 2 mL of PBS. Then, fixation with 4% PFA in PBS (w/v) for 20 min at room temperature was performed. Wells were washed three times with 0.5 mL of washing buffer containing 1% BSA (Sigma-Aldrich, USA) in PBS for 5 min each. Permeabilization and blocking was performed with 0.3% Triton X-100 (Sigma-Aldrich, USA) and 1% BSA in PBS for 45 min at room temperature. The cytoskeleton of cells was subsequently stained with methanolic Alexa Fluor488 Phalloidin (Thermo Fisher Scientific, USA) diluted 1:100 in washing buffer and incubated for 30 min at room temperature in the

dark. The samples were subsequently washed three times and counterstained with a Hoechst 33342 trihydrochloride, trihydrate (10 mg/mL) solution (Thermo Fisher Scientific, USA) diluted 1:1000 in washing buffer for 5 min at room temperature in the dark. Samples were rinsed once with PBS, mounted with ProLong Gold anti-fade mounting medium (Thermo Fisher Scientific, USA) and incubated overnight at room temperature in the dark. Samples were analysed using a Nikon eclipse Ti microscope equipped with a Nikon C2 confocal system. A Nikon S Plan Fluor ELWD 40×/0.60 objective was used. For Alexa Fluor488 Phalloidin, 488 nm was used for excitation, but for Hoechst and QD655, 405 nm lasers were used for excitation. To detect fluorescence for Hoechst - 447/60 nm, Alexa Fluor488 Phalloidin - 525/50 nm and QD655 - 561 LP band pass filters were used (Nikon, Japan). Each channel was recorded separately to avoid spectral overlap. The images were analysed using Nis-Elements C 4.13 software (Nikon, Japan).

Endocytosis inhibitor assay

To analyse the pathway of QD uptake in MSCs, five endocytosis inhibitors were selected: the clathrin pathway inhibitor chlorpromazine (CPZ), phagocytosis inhibitor cytohalasin D (CytD), macropinocytosis inhibitor ethylisopropyl amiloride (EIPA) (Cayman Chemical, USA), caveolin/lipid raft-mediated endocytosis inhibitor nystatin and caveolin-dependent endocytosis inhibitor dynasore (all from Sigma-Aldrich, USA, unless otherwise stated). The optimal inhibitor concentration was selected using the CCK-8 viability assay. Briefly, 5×10^3 cells per well were seeded on a 96-well plate in 100 µL of complete medium. The next day, endocytosis inhibitors were added in serial dilutions with a twofold dilution factor. The range of the tested inhibitor concentrations was from 1.25–160 µM. The cells were incubated with inhibitors for 24 h. After incubation, 10 µL of CCK-8 reagent was added to each well and incubated for 2 h at 37 °C in 5% CO_2 at 90% humidity. The optical density was recorded on a Bio-Tek *ELx808* instrument at 450 nm (BioTek Instruments, USA).

MSCs were seeded onto 8-well chamber slides with 2×10^4 cells per well in 0.5 mL of complete medium and incubated for 1 h with the respective inhibitors at the following concentrations: 40 µM CPZ, 2 µM CytD, 5 µM EIPA, 80 µM nystatin and 80 µM dynasore, at 37 °C, 5% CO_2 and 95% humidity. The medium was aspirated from the wells, and 16 nM QDs were added to samples in complete or serum-free medium and incubated for 6 h. The medium was aspirated and samples were rinsed with 2 mL of PBS. Control wells contained nonlabelled cells. The samples were subsequently stained with methanolic Phalloidin Alexa Fluor488 (Thermo Fisher Scientific, USA) as previously described and analysed using confocal microscopy.

Quantification of the QD fluorescent signal was achieved using Nis-Elements C 4.13 software. Single cell borders were defined according to the Phalloidin Alexa488 staining. The mean fluorescence was measured in the middle z-section of the cell in the red channel only. As a control, the background mean fluorescence from different parts of the image was measured. The QD fluorescence intensity of single cells was calculated by subtracting the background mean intensity from the single-cell mean intensity average.

Transfection assay

Analogous to the description in [61], transient transfection of MSCs was performed using Cell Light® Reagent-GFP, BacMam 2.0 (Thermo Fisher Scientific, USA) according to the manufacturer's recommendations. Briefly, MSCs were seeded at a density of 1.5×10^4 cells per well onto 12-well plates in complete growth medium. After the cells attached, BacMam 2.0 reagent was added at a concentration of 80 particles per cell (PPC). Cell Light® Early endosomes-GFP, BacMam 2.0 was used to label early endosomes (Rab5a-GFP expression), Cell Light® Late endosomes-GFP, BacMam 2.0 was used to label late endosomes (Rab7a-GFP expression), and Cell Light® Lysosomes-GFP, and BacMam 2.0 was used to label lysosomes (Lamp1-GFP expression). The cells were transfected for 72 h.

QD localization study

Transfected MSCs were trypsinized and seeded onto 8-well chambered coverslips (Nunc, Thermo Fisher Scientific, USA) at a density of 3×10^4 cells per well in medium to adhere overnight, and 16 nM of QDs diluted in complete growth medium were added, followed by incubation for 30 min and 1, 6, 24 and 48 h. After incubation, the medium was aspirated and each well was rinsed with PBS. To label nuclei, Hoechst 33342 (Sigma-Aldrich) was diluted in a complete growth medium to a concentration of 25 µg/mL and added to the wells, and the cells were immediately imaged with a laser scanning confocal microscope (Nikon Eclipse TE2000-S, C1 Plus (Nikon, Japan)) using an oil-immersion 60× NA1.4 objective (Plan Apo VC (Nikon, Japan)). A diode laser (404 nm) was used for Hoechst, an argon ion laser (488 nm) for GFP, and a helium–neon laser (543 nm) for QDs. The images were captured with the EZ-C1 v3.90 image analysis software (Nikon, Japan) and further processed using EZ-C1 Bronze v3.80 (Nikon, Japan) and ImageJ 1.48 (National Institute of Health, USA) software.

Statistical analysis

Statistical analysis was performed using GraphPad Prism Software (Graph Pad Inc., USA). The data are expressed as the representative results or the means of at least three independent experiments +/- standard error of the mean. Statistical significance was analysed using one-way ANOVA. Significance

was represented as *p-value < 0.05, **p-value < 0.01, ***p-value < 0.001.

Acknowledgements

This work was supported by Taiwan-Lithuania-Latvia mutual research collaboration fund grant (LV-LT-TW-/2016/6).

References

1. Ferlay, J.; Soerjomataram, I.; Dikshit, R.; Eser, S.; Mathers, C.; Rebelo, M.; Parkin, D. M.; Forman, D.; Bray, F. *Int. J. Cancer* **2015,** *136,* E359–E386. doi:10.1002/ijc.29210
2. Markman, J. L.; Rekechenetskiy, A.; Holler, E.; Ljubimova, J. Y. *Adv. Drug Delivery Rev.* **2013,** *65,* 1866–1879. doi:10.1016/j.addr.2013.09.019
3. Gao, Z.; Zhang, L.; Hu, J.; Sun, Y. *Nanomedicine* **2013,** *9,* 174–184. doi:10.1016/j.nano.2012.06.003
4. Sadhukha, T.; O'Brien, T. D.; Prabha, S. *J. Controlled Release* **2014,** *196,* 243–251. doi:10.1016/j.jconrel.2014.10.015
5. Usha, L.; Rao, G.; Christopherson, K., II; Xu, X. L. *PLoS One* **2013,** *8,* e67895. doi:10.1371/journal.pone.0067895
6. Kidd, S.; Spaeth, E.; Dembinski, J. L.; Dietrich, M.; Watson, K.; Klopp, A.; Battula, V. L.; Weil, M.; Andreeff, M.; Marini, F. C. *Stem Cells (Durham, NC, U. S.)* **2009,** *27,* 2614–2623. doi:10.1002/stem.187
7. Dominici, M.; Le Blanc, K.; Mueller, I.; Slaper-Cortenbach, I.; Marini, F. C.; Krause, D. S.; Deans, R. J.; Keating, A.; Prockop, D. J.; Horwitz, E. M. *Cytotherapy* **2006,** *8,* 315–317. doi:10.1080/14653240600855905
8. Maleki, M.; Ghanbarvand, F.; Reza Behvarz, M.; Ejtemaei, M.; Ghadirkhomi, E. *Int. J. Stem Cells* **2014,** *7,* 118–126. doi:10.15283/ijsc.2014.7.2.118
9. Toma, J. G.; McKenzie, I. A.; Bagli, D.; Miller, F. D. *Stem Cells (Durham, NC, U. S.)* **2005,** *23,* 727–737. doi:10.1634/stemcells.2004-0134
10. Parfejevs, V.; Gavare, M.; Cappiello, L.; Grube, M.; Muceniece, R.; Riekstina, U. *Spectroscopy (N. Y., NY, U. S.)* **2012,** *27,* 315–320. doi:10.1155/2012/286542
11. Smith, A. M.; Mancini, M. C.; Nie, S. *Nat. Nanotechnol.* **2009,** *4,* 710–711. doi:10.1038/nnano.2009.326
12. Sperling, R. A.; Parak, W. J. *Philos. Trans. R. Soc. London, Ser. A* **2010,** *368,* 1333–1383. doi:10.1098/rsta.2009.0273
13. Yong, Y.; Cheng, X.; Bao, T.; Zu, M.; Yan, L.; Yin, W.; Ge, C.; Wang, D.; Gu, Z.; Zhao, Y. *ACS Nano* **2015,** *9,* 12451–12463. doi:10.1021/acsnano.5b05825
14. Ruan, J.; Song, H.; Qian, Q.; Li, C.; Wang, K.; Bao, C.; Cui, D. *Biomaterials* **2012,** *33,* 7093–7102. doi:10.1016/j.biomaterials.2012.06.053
15. Steponkiene, S.; Valanciunaite, J.; Skripka, A.; Rotomskis, R. *J. Biomed. Nanotechnol.* **2014,** *10,* 679–686. doi:10.1166/jbn.2014.1738
16. Steponkiene, S.; Dapkute, D.; Riekstina, U.; Rotomskis, R. *J. Nanomed. Nanotechnol.* **2015,** *6,* 341. doi:10.4172/2157-7439.1000341
17. Hsieh, S.-C.; Wang, F.-F.; Lin, C.-S.; Chen, Y.-J.; Hung, S.-C.; Wang, Y.-J. *Biomaterials* **2006,** *27,* 1656–1664. doi:10.1016/j.biomaterials.2005.09.004
18. Bouwstra, J. A.; Ponec, M. *Biochim. Biophys. Acta* **2006,** *1758,* 2080–2095. doi:10.1016/j.bbamem.2006.06.021
19. Rotomskis, R. Quantum dot migration through natural barriers and distribution in the skin. In *Nanoscience in Dermatology;* Hamblin, M. R.; Avci, P.; Prow, T. W., Eds.; Elsevier: Amsterdam, Netherlands, 2016; pp 307–321. doi:10.1016/B978-0-12-802926-8.00024-0
20. Ahn, J.; Lee, H.; Seo, K.; Kang, S.; Ra, J.; Youn, H. *PLoS One* **2013,** *8,* e74897. doi:10.1371/journal.pone.0074897
21. Ramdasi, S.; Sarang, S.; Viswanathan, C. *Int. J. Hematol. Oncol. Stem Cell Res.* **2015,** *9,* 2.
22. Pessina, A.; Bonomi, A.; Coccè, V.; Invernici, G.; Navone, S.; Cavicchini, L.; Sisto, F.; Ferrari, M.; Viganò, L.; Locatelli, A.; Ciusani, E.; Cappelletti, G.; Cartelli, D.; Arnaldo, C.; Parati, E.; Marfia, G.; Pallini, R.; Falchetti, M. L.; Alessandri, G. *PLoS One* **2011,** *6,* e28321. doi:10.1371/journal.pone.0028321
23. Damalakiene, L.; Karabanovas, V.; Bagdonas, S.; Valius, M.; Rotomskis, R. *Int. J. Nanomed.* **2013,** 555–568. doi:10.2147/IJN.S39658
24. Rustad, K. C.; Gurtner, G. C. *Adv. Wound Care* **2012,** *1,* 147–152. doi:10.1089/wound.2011.0314
25. Studeny, M.; Marini, F. C.; Champlin, R. E.; Zompetta, C.; Fidler, I. J.; Andreeff, M. *Cancer Res.* **2002,** *62,* 13.
26. Brennen, W. N.; Chen, S. L.; Denmeade, S. R.; Isaacs, J. T. *Oncotarget* **2013,** *4,* 106–117.
27. Loebinger, M. R.; Kyrtatos, P. G.; Turmaine, M.; Price, A. N.; Pankhurst, Q.; Lythgoe, M. F.; Janes, S. M. *Cancer Res.* **2009,** *69,* 8862–8867. doi:10.1158/0008-5472.CAN-09-1912
28. Correa, D.; Somoza, R. A.; Lin, P.; Schiemann, W. P.; Caplan, A. I. *Int. J. Cancer* **2016,** *138,* 417–427. doi:10.1002/ijc.29709
29. Lourenco, S.; Teixeira, V. H.; Kalber, T.; Jose, R. J.; Floto, R. A.; Janes, S. M. *J. Immunol.* **2015,** *194,* 3463–3474. doi:10.4049/jimmunol.1402097
30. Dror, S.; Sander, L.; Schwartz, H.; Sheinboim, D.; Barzilai, A.; Dishon, Y.; Apcher, S.; Golan, T.; Greenberger, S.; Barshack, I.; Malcov, H.; Zilberberg, A.; Levin, L.; Nessling, M.; Friedmann, Y.; Igras, V.; Barzilay, O.; Vaknine, H.; Brenner, R.; Zinger, A.; Schroeder, A.; Gonen, P.; Khaled, M.; Erez, N.; Hoheisel, J. D.; Levy, C. *Nat. Cell Biol.* **2016,** *18,* 1006–1017. doi:10.1038/ncb3399
31. Shah, B. S.; Clark, P. A.; Moioli, E. K.; Stroscio, M. A.; Mao, J. J. *Nano Lett.* **2007,** *7,* 3071–3079. doi:10.1021/nl071547f
32. Rak-Raszewska, A.; Marcello, M.; Kenny, S.; Edgar, D.; Sée, V.; Murray, P. *PLoS One* **2012,** *7,* e32650. doi:10.1371/journal.pone.0032650
33. Candini, O.; Spano, C.; Murgia, A.; Grisendi, G.; Veronesi, E.; Piccinno, M. S.; Ferracin, M.; Negrini, M.; Giacobbi, F.; Bambi, F.; Horwitz, E. M.; Conte, P.; Paolucci, P.; Dominici, M. *Stem Cells (Durham, NC, U. S.)* **2015,** *33,* 939–950. doi:10.1002/stem.1897
34. Yong, K.-T.; Law, W.-C.; Hu, R.; Ye, L.; Liu, L.; Swihart, M. T.; Prasad, P. N. *Chem. Soc. Rev.* **2013,** *42,* 1236–1250. doi:10.1039/c2cs35392j
35. Rocha, T. L.; Mestre, N. C.; Sabóia-Morais, S. M.; Bebianno, M. J. *Environ. Int.* **2017,** *98,* 1–17. doi:10.1016/j.envint.2016.09.021
36. Chen, N.; He, Y.; Su, Y.; Li, X.; Huang, Q.; Wang, H.; Zhang, X.; Tai, R.; Fan, C. *Biomaterials* **2012,** *33,* 1238–1244. doi:10.1016/j.biomaterials.2011.10.070
37. Walling, M. A.; Novak, J. A.; Shepard, J. R. E. *Int. J. Mol. Sci.* **2009,** *10,* 441–491. doi:10.3390/ijms10020441
38. Yaghini, E.; Pirker, K. F.; Kay, C. W. M.; Seifalian, A. M.; MacRobert, A. J. *Small* **2014,** *10,* 5106–5115. doi:10.1002/smll.201401209

39. Karabanovas, V.; Zitkus, Z.; Kuciauskas, D.; Rotomskis, R.; Valius, M. *J. Biomed. Nanotechnol.* **2014,** *10,* 775–786. doi:10.1166/jbn.2014.1770
40. Muller-Borer, B. J.; Collins, M. C.; Gunst, P. R.; Cascio, W. E.; Kypson, A. P. J. *NanoBiotechnology* **2007,** 9. doi:10.1186/1477-3155-5-9
41. Cheng, X.; Tian, X.; Wu, A.; Li, J.; Tian, J.; Chong, Y.; Chai, Z.; Zhao, Y.; Chen, C.; Ge, C. *ACS Appl. Mater. Interfaces* **2015,** *7,* 20568–20575. doi:10.1021/acsami.5b04290
42. Wang, L. H.; Rothberg, K. G.; Anderson, R. G. *J. Cell Biol.* **1993,** *123,* 1107. doi:10.1083/jcb.123.5.1107
43. Zhu, X.-D.; Zhuang, Y.; Ben, J.-J.; Qian, L.-L.; Huang, H.-P.; Bai, H.; Sha, J.-H.; He, Z.-G.; Chen, Q. *J. Biol. Chem.* **2011,** *286,* 8231–8239. doi:10.1074/jbc.M110.145888
44. Xiao, Y.; Forry, S. P.; Gao, X.; Holbrook, R. D.; Telford, W. G.; Tona, A. *J. Nanobiotechnol.* **2010,** *8,* 13. doi:10.1186/1477-3155-8-13
45. Zhang, L. W.; Bäumer, W.; Monteiro-Riviere, N. A. *Nanomedicine (London, U. K.)* **2011,** *6,* 777–791. doi:10.2217/nnm.11.73
46. Zhang, L. W.; Monteiro-Riviere, N. A. *Toxicol. Sci.* **2009,** *110,* 138–155. doi:10.1093/toxsci/kfp087
47. Ritz, S.; Schöttler, S.; Kotman, N.; Baier, G.; Musyanovych, A.; Kuharev, J.; Landfester, K.; Schild, H.; Jahn, O.; Tenzer, S.; Mailänder, V. *Biomacromolecules* **2015,** *16,* 1311–1321. doi:10.1021/acs.biomac.5b00108
48. Kou, L.; Sun, J.; Zhai, Y.; He, Z. *Asian J. Pharm. Sci. (Amsterdam, Neth.)* **2013,** *8,* 1–10. doi:10.1016/j.ajps.2013.07.001
49. Huang, D.-M.; Hung, Y.; Ko, B.-S.; Hsu, S.-C.; Chen, W.-H.; Chien, C.-L.; Tsai, C.-P.; Kuo, C.-T.; Kang, J.-C.; Yang, C.-S.; Mou, C.-Y.; Chen, Y.-C. *FASEB J.* **2005,** *19,* 2014–2016. doi:10.1096/fj.05-4288fje
50. Pi, Q. M.; Zhang, W. J.; Zhou, G. D.; Liu, W.; Cao, Y. *BMC Biotechnol.* **2010,** *10,* 36. doi:10.1186/1472-6750-10-36
51. Oh, N.; Park, J. H. *Int. J. Nanomed.* **2014,** *9* (Suppl. 1), 51–63. doi:10.2147/IJN.S26592
52. Peng, L.; He, M.; Chen, B.; Wu, Q.; Zhang, Z.; Pang, D.; Zhu, Y.; Hu, B. *Biomaterials* **2013,** *34,* 9545–9558. doi:10.1016/j.biomaterials.2013.08.038
53. Sarkadi, B.; Özvegy-Laczka, C.; Német, K.; Váradi, A. *FEBS Lett.* **2004,** *567,* 116–120. doi:10.1016/j.febslet.2004.03.123
54. Al-Hajaj, N. A.; Moquin, A.; Neibert, K. D.; Soliman, G. M.; Winnik, F. M.; Maysinger, D. *ACS Nano* **2011,** *5,* 4909–4918. doi:10.1021/nn201009w
55. Pietilä, M.; Lehenkari, P.; Kuvaja, P.; Kaakinen, M.; Kaul, S. C.; Wadhwa, R.; Uemura, T. *Exp. Cell Res.* **2013,** *319,* 2770–2780. doi:10.1016/j.yexcr.2013.07.023
56. Ke, F.; Zhang, L.; Liu, Z.; Yan, S.; Xu, Z.; Bai, J.; Zhu, H.; Lou, F.; Cai, W.; Sun, Y.; Gao, Y.; Wang, H.; Wang, H. *Stem Cells Transl. Med.* **2016,** *5,* 301–313. doi:10.5966/sctm.2015-0179
57. Shi, Y.; Du, L.; Lin, L.; Wang, Y. *Nat. Rev. Drug Discovery* **2017,** *16,* 35–52. doi:10.1038/nrd.2016.193
58. Balkwill, F. *Nat. Rev. Cancer* **2009,** *9,* 361–371. doi:10.1038/nrc2628
59. Riekstina, U.; Muceniece, R.; Cakstina, I.; Muiznieks, I.; Ancans, J. *Cytotechnology* **2008,** *58,* 153. doi:10.1007/s10616-009-9183-2
60. Xu, G.; Lin, G.; Lin, S.; Wu, N.; Deng, Y.; Feng, G.; Chen, Q.; Qu, J.; Chen, D.; Chen, S.; Niu, H.; Mei, S.; Yong, K.-T.; Wang, X. *Sci. Rep.* **2016,** *6,* No. 37677. doi:10.1038/srep37677
61. Matulionyte, M.; Dapkute, D.; Budenaite, L.; Jarockyte, G.; Rotomskis, R. *Int. J. Mol. Sci.* **2017,** *18,* No. 378. doi:10.3390/ijms18020378

2 publikacija / 2nd publication

Skin-derived mesenchymal stem cells as quantum dot vehicles to tumors

Dapkute D, Steponkiene S, Bulotiene D, Saulite L, Riekstina U, Rotomskis R.

International Journal of Nanomedicine **12**:8129–8142 (2017)

DOI: 10.2147/IJN.S143367

International Journal of Nanomedicine

Dovepress
open access to scientific and medical research

Open Access Full Text Article

ORIGINAL RESEARCH

Skin-derived mesenchymal stem cells as quantum dot vehicles to tumors

This article was published in the following Dove Press journal:
International Journal of Nanomedicine
6 November 2017
Number of times this article has been viewed

Dominyka Dapkute[1,2]
Simona Steponkiene[1]
Danute Bulotiene[1]
Liga Saulite[3]
Una Riekstina[3]
Ricardas Rotomskis[1,4]

[1]Biomedical Physics Laboratory, National Cancer Institute, Vilnius, Lithuania; [2]Institute of Biosciences, Vilnius University, Vilnius, Lithuania; [3]Faculty of Medicine, University of Latvia, Riga, Latvia; [4]Biophotonics Group of Laser Research Center, Faculty of Physics, Vilnius University, Vilnius, Lithuania

Purpose: Cell-mediated delivery of nanoparticles is emerging as a new method of cancer diagnostics and treatment. Due to their inherent regenerative properties, adult mesenchymal stem cells (MSCs) are naturally attracted to wounds and sites of inflammation, as well as tumors. Such characteristics enable MSCs to be used in cellular hitchhiking of nanoparticles. In this study, MSCs extracted from the skin connective tissue were investigated as transporters of semiconductor nanocrystals quantum dots (QDs).

Materials and methods: Cytotoxicity of carboxylated CdSe/ZnS QDs was assessed by lactate dehydrogenase cell viability assay. Quantitative uptake of QDs was determined by flow cytometry; their intracellular localization was evaluated by confocal microscopy. In vitro tumor-tropic migration of skin-derived MSCs was verified by Transwell migration assay. For in vivo migration studies of QD-loaded MSCs, human breast tumor-bearing immunodeficient mice were used.

Results: QDs were found to be nontoxic to MSCs in concentrations no more than 16 nM. The uptake studies showed a rapid QD endocytosis followed by saturating effects after 6 h of incubation and intracellular localization in the perinuclear region. In vitro migration of MSCs toward MDA-MB-231 breast cancer cells and their conditioned medium was up to nine times greater than the migration toward noncancerous breast epithelial cells MCF-10A. In vivo, systemically administered QD-labeled MSCs were mainly located in the tumor and metastatic tissues, evading most healthy organs with the exception being blood clearance organs (spleen, kidneys, liver).

Conclusion: Skin-derived MSCs demonstrate applicability in cell-mediated delivery of nanoparticles. The findings presented in this study promise further development of a cell therapy and nanotechnology-based tool for early cancer diagnostics and therapy.

Keywords: mesenchymal stem cells, tumor tropism, quantum dots, nanoparticles, tumor-specific delivery, immunodeficient mice

Introduction

Despite advances made in cancer therapy, it is generally accepted that conventional treatment methods are not sufficient to permanently eliminate cancer and cancer stem-like cells.[1] Nanotechnology emerged as one of the most promising solutions; however, nanoparticles themselves lack specificity to tumors, and thus, cell-based therapies were proposed. Out of all potential human cell sources, human mesenchymal stem cells (MSCs) were introduced as the most promising. MSCs do not evoke ethical controversy, have no tissue compatibility issues, and possess low tumorigenicity risk.[2,3] MSCs are non-hematopoietic spindle-shaped fibroblast-like cells derived from the mesoderm.[4] MSCs possess self-renewal and immunomodulatory properties, are capable of transdifferentiation, and participate in wound healing, bone regeneration, angiogenesis, and homeostasis.[5–7] Due to these characteristics, MSCs

Correspondence: Ricardas Rotomskis
Biomedical Physics Laboratory, National Cancer Institute, P. Baublio 3b, LT-08406, Vilnius, Lithuania
Tel +370 5 219 0903
Email ricardas.rotomskis@nvi.lt

http://dx.doi.org/10.2147/IJN.S143367

hold great promise in the treatment of wounds, degenerative diseases, and other pathologies.[8] Cancer cells secrete various chemokines similar to the ones produced in the lesion sites;[9] therefore, tumors are sometimes called wounds that do not heal.[10] MSCs have chemokine receptors[11] and a tendency to migrate through the chemokine gradient toward the tumor.[12,13] Owing to these tumor-tropic properties, MSCs could be used to transport therapeutic molecules directly to cancerous tissues. MSC-mediated transportation of different signaling molecules (interleukins, interferons, chemokines),[14,15] genetically modified viruses,[16] gene therapy components,[17] chemotherapeutic drugs and prodrugs[18,19] are already topics of research. There are also successful studies investigating the use of MSCs in transportation of nanoparticles – one of the main achievements was the delivery of optically active nanoparticles via MSCs across the blood–brain barrier and homing to glioblastomas.[20,21] Knowledge about MSC tumor-tropic properties and their potential to perform tumor-directed delivery of nanoparticles opens the way to novel therapy.

Of the wide variety of nanoparticles investigated, quantum dots (QDs) have perhaps the most extensive applications. QDs exhibit unique photophysical properties. Some of the most desired characteristics of QDs are broad excitation and a narrow photoluminescence (PL) emission spectra.[22] Together with the quantum confinement effect, which implements the size-dependent PL emission of QDs, such spectral characteristics enable the use of several QDs with different wavelengths in a single experiment and the construction of nanocrystals that fluoresce in a tissue optical window.[23,24] QDs are also characterized by their brightness and high photostability.[22] These optical properties permit QDs to be used in long-term tissue imaging and in vivo cell tracking. QDs have already been employed to track MSCs in regenerative or cancer therapies due to their superior in vitro cell tracking capability compared to commercial cell trackers.[25] The large surface area of nanoparticles allows the attachment of multiple biologically active molecules, such as proteins, drugs, photosensitizers, and/or antibodies.[24] Thus, QDs could combine a cell-imaging probe and a tumor-targeting agent in one platform.

Most researchers use bone marrow[19,26–28] or adipose tissue-derived[18,29,30] MSCs. In this study, we used human dermal MSCs. The successful application of dermal MSCs for the delivery of nanoparticles would be highly advantageous because of the high tissue accessibility and tractability.[31] MSCs are abundant in skin tissues and can be obtained with minimally invasive procedures. In addition, after some surgeries, the skin tissue is considered a surgical waste and, therefore, could be used for a cost-effective appliance in cancer treatment. Post-surgery material gathered after liposuction,[32] amputations,[33] or surgical debridement[34] has already been suggested as a source of MSCs.

We used Invitrogen Qdot® 625 ITK™ Carboxyl QDs to investigate the effect of nanoparticles on MSC migration in vitro and in vivo. Here, we identified the optimal nontoxic concentration of QDs, internalization dynamics of QDs into MSCs, nanoparticle intracellular localization, and most importantly, the QD-loaded MSC ability to migrate toward cancer cells in vitro and in vivo. Altogether, the results presented in this article show the promising potential of MSCs to be used as nanoparticle carriers to the tumors.

Materials and methods

Materials

Qdot 625 ITK nontargeted carboxyl-coated QDs used in the study were purchased from Thermo Fisher Scientific (Waltham, MA, USA). QDs consisted of CdSe/ZnS core/shell and were coated by carboxylic acid–functionalized polyethylene glycol (PEG) lipids, and had a strong emission in the red region with the emission peak at 625 nm. Atomic force microscopy and dynamic light scattering data showed mean nanoparticle size to be ~14.5 nm (Figure 1).

Mouse anti-human monoclonal antibodies were the following: CD44 conjugated with Alexa Fluor® 488 (BioLegend, San Diego, CA, USA), CD90 conjugated with fluorescein isothiocyanate (FITC) (Dako Denmark A/S, Glostrup, Denmark), CD73 conjugated with phycoerythrin (PE; BD Biosciences, San Jose, CA, USA), CD105 conjugated with allophycocyanin (APC) (R&D Systems, Minneapolis, MN, USA), CD45

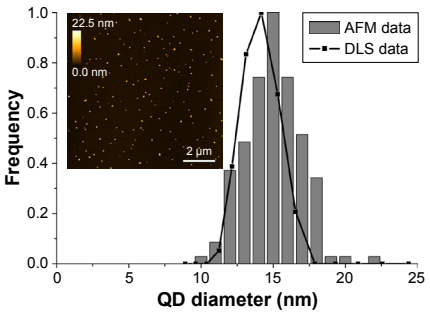

Figure 1 Analysis of QD size measured using AFM and DLS, and representative AFM micrograph of QDs dispersed on freshly cleaved mica surface.
Notes: The hydrodynamic diameter was measured using a DLS device Zeta Plus PALS (Brookhaven Inc., Holtsville, NY, USA). AFM Innova (Veeco Inc., Plainview, NY, USA) was used for QD imaging in the tapping mode using silicon nitride probes.
Abbreviations: AFM, atomic force microscopy; DLS, dynamic light scattering; QDs, quantum dots.

conjugated with FITC, CD34 conjugated with PE, CD14 conjugated with APC, CD184 (CXCR4) conjugated with PE (all four from BD Biosciences). The lactate dehydrogenase (LDH) cytotoxicity detection kit CytoTox 96® was purchased from Promega (Madison, WI, USA).

Primary cell cultures and cell lines

Primary human skin MSCs used for this study were supplied by a frozen primary cell bank established from cultivated dermis-derived adherent cells, isolated from post-surgery materials as described earlier.[35] MSCs were used in accordance with authorized approval from the Institute of Experimental and Clinical Medicine Ethics committee, University of Latvia (issued on 04.06.2014). Skin MSCs were grown in DMEM with F12 Nutrient mixture (DMEM/F12, 3:1 v/v; Thermo Fisher Scientific) supplemented with 10% of fetal bovine serum (FBS; Sigma-Aldrich, St Louis, MO, USA) and 1% antibiotics (100 U/mL penicillin, 100 µg/mL streptomycin; Biochrom, Berlin, Germany). MSCs used in the experiments were between passages 4 and 8. To ensure the consistency of the results and prevent donor-dependent variations, MSCs from a single donor were used in all the experiments, if not stated otherwise.

Human breast cancer cell line MDA-MB-231 (ATCC HTB-26™) and human mammary epithelial cell line MCF-10A (ATCC CRL-10317™) were obtained from the American Type Culture Collection (ATCC, Manassas, VA, USA). MDA-MB-231 cells were cultured in DMEM (Thermo Fisher Scientific) supplemented with 10% FBS and 1% antibiotics. MCF-10A cells were cultured in HuMEC Basal Serum-Free Medium supplemented with 1% HuMEC supplement, 0.4% bovine pituitary extract (all from Thermo Fisher Scientific), and 1% antibiotics.

Cells were cultured and passaged in 25–75 cm² cell culture flasks with up to 90% confluence with complete cell culture medium. Cells were grown in a humidified chamber at 37°C with 5% CO_2.

Immunostaining of MSCs

MSCs were characterized by the criteria set by the International Society of Cellular Therapy.[36] Immunophenotype of MSCs was detected by staining 1×10^5 cells using antibodies against mesenchymal markers CD90, CD73, CD105, and hematopoiesis markers CD45, CD34, CD14, according to the manufacturer's instructions. Additionally, cells were stained with CD184 to detect the amount of CXCR4 on the membrane of MSCs. Stained and washed cells were analyzed with a flow cytometer.

Optimization and quantification of QD internalization

Maximum nontoxic QD concentration was determined using standard LDH cytotoxicity assay. MSCs were seeded into 96-well plates at a density of 5×10^3 cells per well in 100 µL of complete medium. After 24 h, the growth medium was supplemented with increasing concentrations of QDs varying from 0.8 to 80 nM. Cells were incubated with QDs for 24 and 48 h. A few wells were chosen as a positive control. Positive control cells were lysed with lysis buffer. After incubation, CytoTox 96 reagent was added to the wells. After 30 min, the stop solution terminated the reaction and the absorbance at 490 nm was measured using Infinite 200 PRO (Tecan, Männedorf, Switzerland). Toxicity was determined by the following formula:

$$\text{Toxicity, \%} = 100 \times \frac{\text{OD}_{490} \text{ of the cells with QDs}}{\text{OD}_{490} \text{ of lysed cells}}$$

where OD is optical density.

Quantitative accumulation of QDs was performed seeding MSCs into six-well plates at a density of 1×10^5 cells per well in 2 mL of complete medium. After 24 h, QDs were added to the culture medium to a final concentration of 16 nM. The incubation was carried out from 1 min to 48 h. After the appropriate incubation time, the monolayer of the cells was washed three times with PBS (Biochrom), trypsinized, and centrifuged (200× *g* for 5 min). The cells were resuspended in 100 µL PBS and analyzed with a flow cytometer.

Intracellular localization

MSCs were seeded in eight-well chamber slides (Nunc Lab-Tek II; Thermo Fisher Scientific) at a density of 3×10^3 cells per well in 400 µL of complete medium. After 24 h, the QDs were diluted in the complete growth medium to a concentration of 16 nM and poured over the cells. The cells were incubated for various time points ranging from 15 min to 48 h. After incubation, the cells were washed a few times with Dulbecco's PBS (Thermo Fisher Scientific) to prevent cell detachment. Cells were fixed with 4% paraformaldehyde (Sigma-Aldrich) for 15 min, permeabilized with 0.2% Triton X-100 (Sigma-Aldrich) for 4 min, and blocked with 1% bovine serum albumin (Sigma-Aldrich) for 20 min. Cells were incubated with 15 U/mL Alexa Fluor 488 Phalloidin (Thermo Fisher Scientific) for 30 min to label actin filaments. Nuclei were stained with 25 µg/mL Hoechst 33258 (Sigma-Aldrich) for 30 min. Slides were mounted with Qdot Mounting media (Thermo Fisher Scientific).

In vitro migration

The tropism of MSCs to tumor cells was determined using Transwell® Permeable Support inserts (Corning Inc., Corning, NY, USA). MDA-MB-231 and MCF-10A (1×10^5 cells/well) cells were seeded onto lower wells of 24-well plates in 600 µL of a serum-free medium. The remaining wells contained MDA-MB-231–conditioned medium (filtered [0.22 µm filter] serum-free medium in which MDA-MB-231 cancer cells had been cultured for 24 h), MSC growth medium supplemented with 20% FBS (positive control), or serum-free medium (negative control). After 24 h, QD-loaded and unlabeled MSCs were resuspended in 100 µL of serum-free medium and placed onto polycarbonate membrane inserts with 8 µm pores (3×10^4 cells/insert). MSC-containing inserts were positioned in the lower wells. MSCs were allowed to migrate through the pores for 24 h under standard cultivation conditions (37°C with 5% CO_2). Nonmigratory cells were wiped away from the inside of the insert using a wet cotton bud. Migratory cells were fixed with 4% paraformaldehyde for 15 min and stained with 25 µg/mL Hoechst overnight. The migrated MSCs were examined under the confocal microscope. Results were evaluated by directly counting the number of migrated cells in at least five fields. The data were normalized according to the MSC migration toward positive control, which represented 100% migration. Results are presented as a mean ± SD. To determine whether in vitro cell migration depends on the donor, MSC migration toward MDA-MB-231 cells, FBS-supplemented and FBS-free medium was tested with, overall, three different donors.

Animals and tumor model

Experiments were performed on 6-week-old female CB17 SCID mice (Taconic Biosciences, Lille Skensved, Denmark). Mice were maintained at a constant temperature (22°C±1°C), relative humidity 55%±10%, and a photoperiod (12 h light/dark cycle). Animals were acclimatized for 7 days before each experiment. The animals were provided with autoclaved rodent chow (Diet 4RF25; Mucedola, Milan, Italy) and purified water ad libitum. Animal experiments were approved by the Animal Care and Use Committee of the State Food and Veterinary Service (approval No G2-29), and all procedures were in accordance with the guidelines for animal research set out in the European Union Directive 2010/63/EU and national regulations. Mice were inoculated with 2×10^6 MDA-MB-231 cells in a volume of 200 µL growth medium into adipose tissue around the nipple using 23G needles. The tumor volume was estimated by measuring three orthogonal diameters (L [length], W [width], H [height]) with calipers; the volume (V) was calculated as follows: $V = (L \times W \times H) \times 0.523$. The migration studies were performed when the tumor size reached 300 mm^3, generally 50–60 days after inoculation. At least five mice were used in the experimental groups.

In vivo migration

After the tumors were formed, 5×10^5 QD-loaded MSCs were injected subcutaneously (in 200 µL growth medium) ~5 mm below the tumor with 23G needles. Control mice were injected with a sterile saline solution. The mice were left for 24 h or 7 days in standard conditions. After the appropriate time, mice were sacrificed and tumor, peritoneum from MSC injection site, lungs, kidneys, brain, heart, spleen, liver, and metastases (if found) were taken. The organs were either cut into slices with cryomicrotome (10 µm slice thickness) or homogenized and analyzed with flow cytometer. Slices were analyzed with confocal microscope to get fluorescent images and later stained with hematoxylin and eosin to get respective histologic images. For the flow cytometric analysis, the organs were minced and digested with 0.25% trypsin/EDTA (Biochrom) for 30 min with continuous shaking at 37°C. After enzymatic dissociation, the suspension was rigorously pipetted with a cut pipette tip. The digested tissues were passed through 70 µm filters to obtain a single cell suspension, mixed with 10% FBS/PBS solution, and centrifuged at $400\times g$ for 5 min. The cells were resuspended in PBS and counted. Then, 1×10^6 cells were stained with anti-CD44 antibody for 30 min, washed, and analyzed with a flow cytometer.

Flow cytometry

Flow cytometric analyses were performed using Accuri C6 (Accuri Cytometers, Inc., Ann Arbor, MI, USA) or Guava EasyCyte (Merck Millipore, Billerica, MA, USA) flow cytometers. A minimum of 10,000 viable cells were acquired. The data were analyzed with FlowJo (Tree Star, Inc., Ashland, OR, USA) and Accuri C6 software (Accuri Cytometers, Inc.).

Laser scanning confocal microscopy

Samples were examined under the Nikon Eclipse TE2000-U microscope (Nikon, Yokohama, Japan) with the confocal laser scanning system C1si (capable of 32-bit spectral imaging). Imaging was performed by scanning with the beam of diode laser (404 nm) for Hoechst, argon ion laser (488 nm) for Alexa Fluor 488, and helium–neon laser (543 nm) for QDs using oil immersion 60× NA 1.4 objective (Plan Apo VC; Nikon). Three different band pass filters were used – 450/35 for Hoechst, 515/30 for Alexa Fluor 488, and 605/75 for QDs. Image processing was performed using EZ-C1 Bronze

version 3.80 (Nikon) and ImageJ 1.48 (National Institute of Health, Bethesda, MD, USA) software.

Statistical analysis

Data are shown as the representative result or as the mean of at least three independent experiments ± SD. Statistical analyses were performed using the two-tailed Student's *t*-test; differences were considered significant at $p \leq 0.05$, and *p*-values are shown in figures where needed.

Results

Characterization of MSCs

The cells isolated from donor skin tissue were plastic adherent and had fibroblast-like spindle-shaped morphology (Figure 2A). The ability of the cells to differentiate into adipocytes, osteocytes, and chondrocytes was evaluated earlier.[37,38] The cultured cells were >95% positive for the expression of mesenchymal markers CD90, CD73, and CD105, and displayed no expression (≤0.5%) of hematopoietic markers CD45, CD34, and CD14 (Figure 2B). According to the criteria defined by the International Society for Cellular Therapy,[36] cells used in this study were considered to be MSCs.

Optimization and quantification of QD internalization

For MSCs to be used as nanoparticle vehicles, the optimal conditions for maximum QD loading must be established.

To evaluate the possible cytotoxic effect of nanoparticles and determine the maximum tolerated QD concentration, standard LDH cytotoxicity assay was used. Using various concentrations of nanoparticles and different incubation time points, we detected that 16 nM was the maximum QD concentration that did not cause any cytotoxicity to MSCs even after 48 h of treatment (Figure 3A). Higher concentrations of QDs caused only minor toxicity (1.7%–5%). Hence, 16 nM concentration was used in the following experiments. The negative value seen in Figure 3A is due to the increased metabolic activity of MSCs after incubation with nanoparticles, because the assay measures LDH activity in the cells. This shows the stimulating effect of nanoparticles on growth and proliferation of MSCs. Such an effect was also noticed by other authors.[39–42]

To optimize the uptake of nanoparticles, the effect of the incubation time was assessed and a quantitative accumulation curve was acquired (Figure 3B). The curve corresponded to the standard S-shaped sigmoid QD accumulation curve (lag, growth, and saturation stages).[43] For the first hour, the QD PL signal was low; after an hour, the PL signal sharply increased until 6 h at which time the transitional phase was reached. Since the results showed that incubation for 6 h is sufficient to obtain the early saturation phase of accumulation, 6 h incubation time point was chosen as the optimal QD incubation time (Figure 3B).

Intracellular localization

Using laser scanning confocal microscope, the uptake and intracellular localization of QDs was detected (Figure 4). The attachment of QDs to the cell membrane was rapid and occurred as early as 15 min incubation (Figure 4, insert a), and was followed by the endocytosis of nanoparticles. The uptake was first detected after 1 h and increased gradually

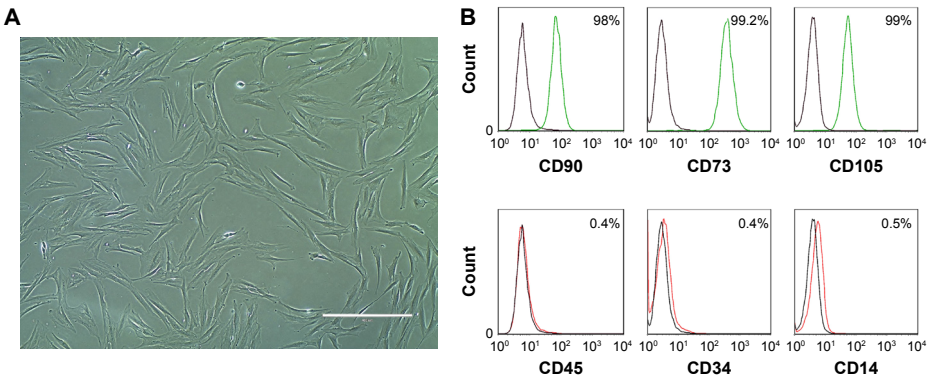

Figure 2 (**A**) Morphology of isolated dermal MSCs. Magnification 10×, scale bar 400 μm. (**B**) Immunophenotype of MSCs.
Notes: Black curve, control; green, mesenchymal markers; red, hematopoiesis markers. Percentage shows positive events.
Abbreviation: MSCs, mesenchymal stem cells.

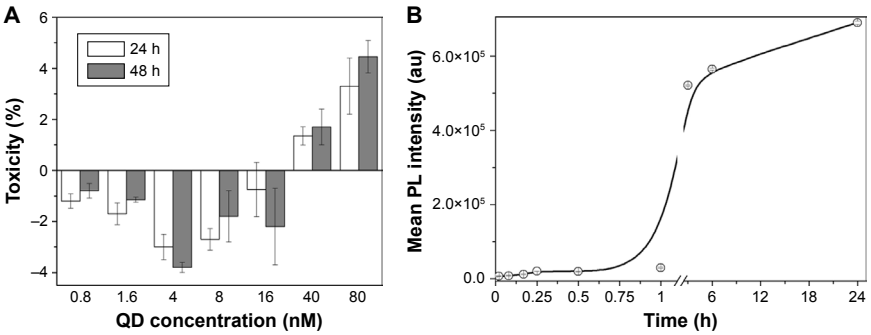

Figure 3 (**A**) QD cytotoxicity to MSCs. (**B**) Dynamics of QD uptake by MSCs.
Note: Error bars represent the SD.
Abbreviations: MSCs, mesenchymal stem cells; PL, photoluminescence; QDs, quantum dots.

with the incubation time. QDs were localized inside the vesicles, demonstrating that endocytosis was their entry pathway (Figure 4, insert b) – our previous study on QD microinjection, mimicking passive diffusion of nanoparticles, demonstrated that after microinjection or membrane damage, the QDs were uniformly dispersed in the cytoplasm of the cells and did not form any vesicular structures, proving endocytosis is responsible for vesicle formation.[43]

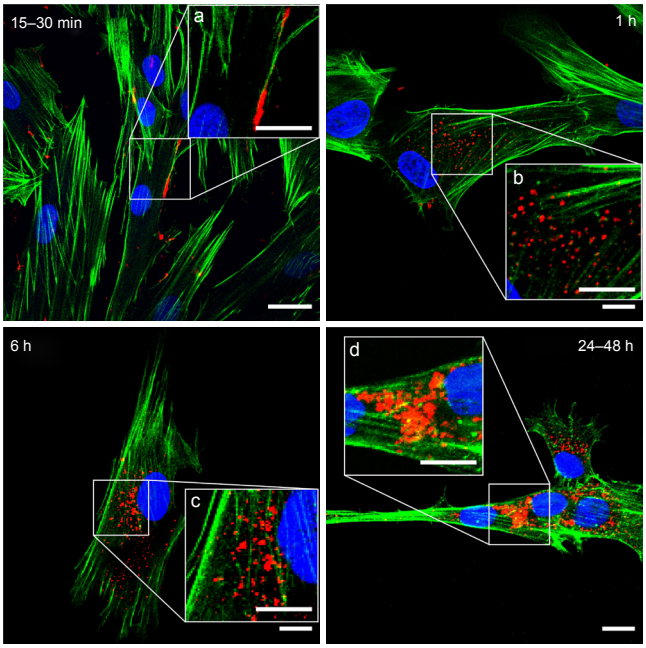

Figure 4 Confocal micrographs showing intracellular localization of QDs in MSCs.
Notes: Blue, nuclei (Hoechst); green, actin (Alexa Fluor 488® Phalloidin); red, QDs. Magnification 60×, scale bar 15 μm. White squares (a–d) mark the zoomed parts shown in the inserts. Inserts scale bar 10 μm.
Abbreviations: MSCs, mesenchymal stem cells; QDs, quantum dots.

After 6 h, all MSCs had incorporated QDs and the endocytic vesicles with nanoparticles inside were spread all over the cytoplasm. After 24 h, the vesicles with QDs merged into multivesicular body-like structures that localized mostly in the perinuclear region (Figure 4, insert d). Along with the intracellular localization, the size of the vesicles containing QDs also changed over time (Figure 4, inserts). QDs were not detected in the nuclei.

In vitro migration

Several studies[44–46] demonstrate the tendency of MSCs to migrate to the sites of the tumor. Therefore, to investigate whether skin MSCs possess the same properties, we simulated the migration of MSCs toward cancer cells (MDA-MB-231) and noncancerous breast epithelial cells (MCF-10A) using Transwell migration assay. During the assay, all the cells were incubated in serum-free medium to prevent nonspecific chemotactic movement toward the serum.

The excessive migration toward positive control (growth medium supplemented with 20% serum) showed that even after the prolonged ex vivo cultivation, MSCs retained their migratory capabilities (Figure 5A, B). The migration toward MDA-MB-231 cancer cells was thirty times greater than the random undirected cell migration toward serum-free medium (negative control), as shown in Figure 5C. In order to verify that MSCs do not migrate toward all types of cells including healthy tissue, cell migration toward nonmalignant breast tissue epithelial cells MCF-10A was tested. The results demonstrate that the migration toward healthy breast tissue cells was the same as an undirected MSC migration (<2%). The migration toward MDA-MB-231–conditioned medium (~33%) proved that cancer cells secrete soluble molecules stimulating MSC migration (Figure 5C). Furthermore, the impact of nanoparticles on the migration of MSCs was evaluated when comparing the migration of QD-loaded and unlabeled MSCs. QDs did not reduce the MSCs' ability to migrate, as there were no statistically significant differences between nanoparticle-labeled and unlabeled MSCs (Figure 5A–C).

To detect whether in vitro migration of MSCs depends on the donor, we tested the migration of MSCs extracted from three different donor skin tissues (Figure 6). The results showed no differences in migration toward positive and negative controls between different donor cells. Yet, some differences arose in migration toward cancer cells – one out of three donor MSCs displayed higher in vitro migration both with and without QDs.

In vivo migration

In vitro migration experiment showed that MSCs have a predisposition to migrate specifically to cancer cells while avoiding healthy cells (Figure 5); thus, the in vivo experiment with human breast tumor-bearing immunodeficient mice was performed. Confocal micrographs of tumor and

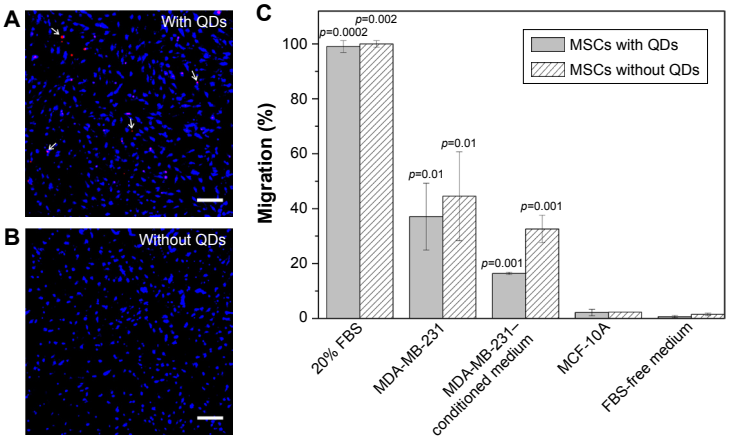

Figure 5 In vitro migration of MSCs.

Notes: MSCs (**A**) with QDs and (**B**) without QDs migrated through 8 μm pores toward a growth medium supplemented with 20% FBS. White arrows in (**A**) show some of the QDs. Cells were stained with Hoechst (nucleus stain); red, QDs. Magnification 10×, scale bar 200 μm. (**C**) MSC in vitro migration toward various chemoattractants. Error bars represent the SDs. Data were normalized according to the migration toward 20% FBS (positive control). *p*-values show significant differences compared to the negative control (FBS-free medium).

Abbreviations: FBS, fetal bovine serum; MSCs, mesenchymal stem cells; QDs, quantum dots.

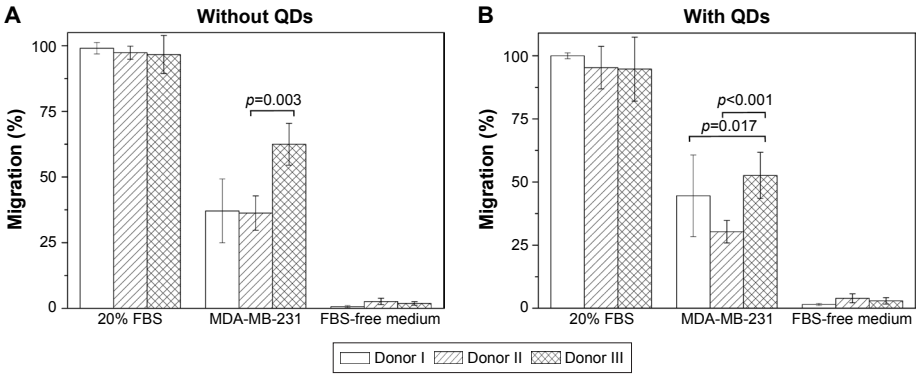

Figure 6 In vitro migration of MSCs extracted from three different donors.
Notes: (**A**) Migration of unlabeled MSCs. (**B**) Migration of QD-loaded MSCs. Data were normalized according to the migration toward 20% FBS (positive control). Error bars represent the SDs.
Abbreviations: FBS, fetal bovine serum; MSCs, mesenchymal stem cells; QDs, quantum dots.

metastasis cryosections showed red QD PL (Figure 7A and D). Interestingly, QD-labeled MSCs were distributed throughout the entire tumor (Figure 7A–C), while in the metastatic tissue, most QDs were detected in cells of different morphology (Figure 7D–F).

In parallel, tissue homogenates were analyzed with a flow cytometer. To accurately evaluate QD-positive cells, homogenized samples were stained with anti-human CD44 antibody that binds only to cancer cells and MSCs. It was discovered that up to 19% of tumor cells were QD-positive cells (Figure 8A). During the tumor formation period, several mice developed spontaneous metastases due to rapid tumor growth. It was a good chance to investigate the accumulation of MSCs at the metastasis site. Up to almost 7% of the cells constituting the metastases were identified as QD positive (Figure 8B). A comprehensive flow cytometric analysis was

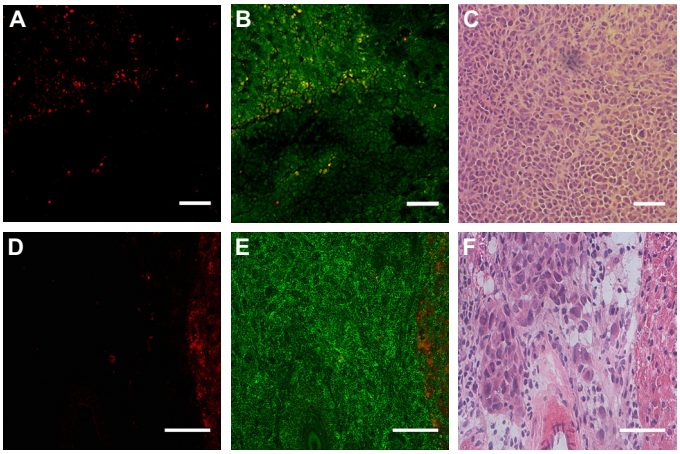

Figure 7 Micrographs showing QD-loaded MSCs in (**A**–**C**) tumor and (**D**–**F**) metastatic tissues. (**A**, **D**) PL, (**B**, **E**) PL and autofluorescence, (**C**, **F**) respective morphologic images (H&E staining).
Note: Scale bar 50 μm.
Abbreviations: H&E, hematoxylin and eosin; MSCs, mesenchymal stem cells; PL, photoluminescence; QDs, quantum dots.

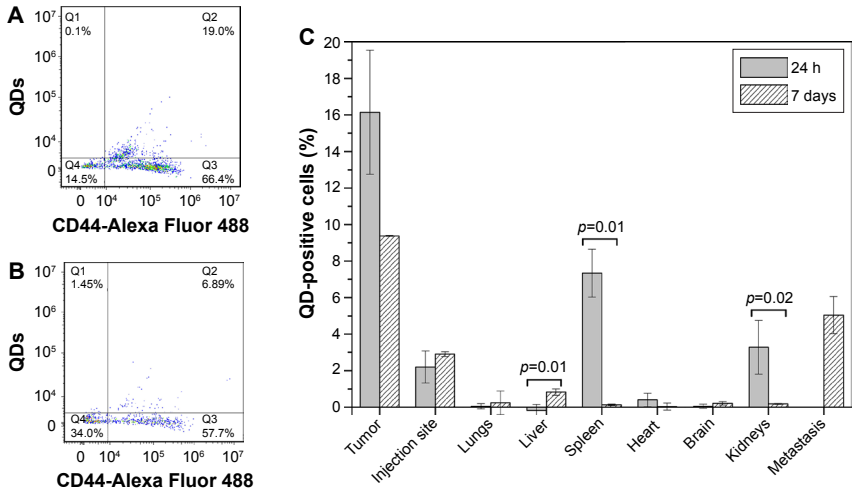

Figure 8 In vivo migration of QD-loaded MSCs.
Notes: (**A**) Flow cytometry dot plot showing tumor homogenate stained with anti-CD44. (**B**) Flow cytometry dot plot showing metastasis homogenate stained with anti-CD44. Q3 quadrant shows human cancer cells, Q4 shows mouse cells, Q2 shows QD-loaded MSCs. (**C**) QD-positive cells found in the respective tissues. *p*-values show significant differences between 24 h and 7 days.
Abbreviations: MSCs, mesenchymal stem cells; QDs, quantum dots.

carried out with healthy mice organs as well. Set side by side, it became obvious that the largest number of QD-positive cells was detected in the tumor. However, after a week, the amount of tumor-residing QD-labeled cells decreased approximately two times (Figure 8C). Twenty-four hours after the injection of MSCs, a statistically significant amount of QD-loaded MSCs was detected in the spleen and kidneys. After 7 days, the amount of QD-positive cells decreased and of all healthy mice organs, they were detected mainly in the liver. The highest accumulation of MSCs in mice organs was in the body parts responsible for filtration and clearance of blood and lymph (liver, spleen, kidneys), which indicates that after 7 days MSCs redistributed into the liver or were cleared from the mice (Figure 8C). The amount of MSCs found in the MSC injection site remained similar throughout the experiment.

Discussion

Nanoparticles might become a preferential choice in the future instead of conventional cancer treatment. Due to exceptional physical, chemical, and optical characteristics, nanoparticles are ideal candidates for early cancer diagnostics and great benefits are anticipated for cancer therapy. Although it is claimed that nanoparticles should accumulate specifically inside the tumor due to the enhanced permeability and retention effect,[47] passive accumulation lacks specificity to tumors.[48] As a result, functionalization of nanoparticles using various targeting molecules – ligands, peptides, antibodies, and so on – became a natural choice. There were attempts to use antibody-conjugated QDs for cancer cell imaging and tracking.[49,50] We previously showed that the antibody–QD complex not only recognizes its specific antigen, but also is engulfed inside the cells, while antibodies conjugated with commonly used organic fluorophore FITC remained on the cell membrane.[50] Although these results show promising potential of antibody–nanoparticle complexes to be used in both diagnostics and therapy, the success of such therapy is limited due to lack of tumor-specific antigens.[51] Ergo, nanoparticle transportation using cells that are naturally attracted to tumors emerged as a potential treatment method. MSCs have natural stealth properties and are able to cross biologic barriers.[52,53] Thus, MSCs hold a tremendous potential for being employed in anticancer therapy as drug delivery vehicles. In addition, nanoparticle-labeled MSC homing to cancerous tissue would add great benefit to visualization of tumors and/or metastases and their response to treatment.

In this study, we analyzed the toxicity, accumulation patterns, and both in vitro and in vivo migration of QD-loaded

dermal MSCs. We have shown that commercially available QDs are nontoxic to MSCs (Figure 3A), are efficiently and rapidly taken up by the cells (Figure 3B), and are localized in endocytic vesicles in the perinuclear region (Figure 4). Despite studies showing nanoparticle anchoring to the outer cell membrane,[54,55] QD internalization by MSCs is more common.[56–58] Nanoparticle uptake and localization inside the cytoplasm is more advantageous as it leaves the cell membrane unaltered since the nanoparticles do not block cellular receptors. Internalization can also protect QDs from interacting with healthy tissue in vivo and from the unpredictable detachment during cargo transportation.[59] QDs did not penetrate into the nucleus of MSCs (Figure 4), hence minimizing the potential genotoxicity caused by the binding of nanoparticles to DNA.[60]

Most importantly, our results showed that MSCs, extracted from the skin connective tissue, were able to migrate toward cancer cells in vitro and in vivo (Figures 5–8). The migration capability toward cancerous tissue is a prerequisite for MSCs to be used in targeting tumor cells. We successfully simulated directional migration of MSCs toward human breast cancer cells and their conditioned medium in vitro. Our results complement the evidence that MSCs tend to migrate toward cancer cells,[13,18] cancer cell-conditioned medium,[61] and growth medium, supplemented with recombinant proteins found in cancer cell-conditioned medium,[62] verifying that cancer cells secrete molecules promoting MSC migration. The key molecules inducing MSC migration toward tumors supposedly are vascular endothelial growth factor,[63] fibroblast growth factor 2,[64] stromal cell derived factor 1 (SDF-1),[65] chemokine (C-C motif) ligand 2, also known as monocyte chemotactic protein-1,[66] and macrophage migration inhibitory factor.[13] MSC migration is suppressed by antibodies against chemokine (C-X-C motif) receptor 4 (CXCR4)[67] or by receptor antagonists,[13] proving SDF-1/CXCR4 to be the main axis mediating MSC migration to cancerous tissue.[51] Our research shows that in comparison to the chemotaxis toward highly potent chemoattractant (growth medium supplemented with 20% serum), the migration induced by cancer cells was mediocre (Figures 5C and 6). However, this may be related to the fact that the conditions under which MSCs are cultured in vitro are different from the ones found in their natural in vivo niches.[68] Therefore, longer ex vivo cultivation leads to the reduced expression of receptors responsible for cell migration toward malignant cells (eg, CXCR4).[69] The receptor for SDF-1 – CXCR4 – is found on both the cancer cell membrane as well as MSCs; thus, it participates in tumor metastasis if overexpressed in cancer cells[70] or partakes in MSC migration toward the tumor if found on MSCs.[71] To detect the level of CXCR4 in skin MSCs, we performed additional flow cytometric analysis on MSCs using anti-CXCR4 monoclonal antibody. The study revealed that our cultured MSCs have only 4%±2.1% CXCR4-positive cells (Figure S1). Shen et al also found 4.1% CXCR4 expression in umbilical cord MSCs,[72] while Shi et al found an almost negative CXCR4 cell surface expression in fetal bone marrow MSCs; whereas, upon cytokine stimulation, the amount of CXCR4 increased to 55.7%.[73] The poor expression of CXCR4 might be the reason for weak MSC migration to cancer cells both in vitro and in vivo and should be increased before in vivo manipulation. Hypoxia,[74] cellular modifications,[75] and preincubation with cytokines, for example, interleukin-6 or hepatocyte growth factor,[76] are several strategies enhancing the migration of MSCs. Additionally, MSC migration potential might be donor dependent. Figure 6 shows that MSC migration depends slightly on the donor – one donor's MSCs possessed higher than usual migration toward cancer cells and such an effect must be taken into account before choosing a donor as it would lead to better outcome of the potential therapy.

Another important factor for low MSC engraftment is the retaining properties of QDs. QD excretion from MSCs is a topic of controversy. Although it has been noted that QDs might leak from intact stem cells,[56,58,77] it was also reported that QD-labeled cells retain bright QD PL for a few weeks and do not transfer nanoparticles to adjacent cells and host tissues.[25,78,79] Such disagreements might be explained by different QD surface charges, as positively charged nanoparticles were used in most studies that showed QD leakage from cells,[56,77] while negatively charged nanoparticles were retained inside the cells better.[78,79] Our previous in vitro studies showed that QD PL decreases by 30% after the first 24 h most probably due to some degradation in lysosomes and does not change after additional 24 hours.[38]

Our in vitro migration study showed that incubation with QDs did not diminish cell migration, showing the biocompatibility of the nanoparticles used (Figures 5 and 6). These results are in agreement with previous studies using MSCs and nanoparticles.[80,81]

In vivo migration results with SCID mice revealed that most MSCs were located in tumor tissue in comparison to healthy organs and MSC injection site. The highest number of MSCs was detected in the tumor 24 h postinjection, suggesting that short periods are sufficient and most suitable for MSCs to reach the tumor. We observed minor engraftment of subcutaneously administered MSCs in organs comprising

the mononuclear phagocyte system – liver, spleen, kidneys (Figure 8C). Previous studies also have shown localization of exogenously administered MSCs in the aforementioned tissues.[82] No distribution of MSCs was detected in other healthy organs, including heart, brain, lungs. Although MSC entrapment in the lungs is quite common due to the large size of the cells (20–24 μm) and the small lung capillaries of diameter 10–15 μm,[83] we detected only a slight engraftment of MSCs in the lungs. Our findings concerning poor distribution of exogenously administered MSCs in healthy tissues are in agreement with earlier reports.[84–86] This property adds to the benefits of MSC application in tumor-tropic therapy, while avoiding multiorgan toxicity.

The role of MSCs in cancer development is a topic of controversy. Although we did find encouraging data that QD-loaded MSCs migrate toward breast tumor in vivo, it must be taken into account that MSCs could act as pro-tumorigenic due to paracrine stimulation that promotes metastases, angiogenesis, immune system suppression, expansion of cancer stem cells,[87–89] as well as tumor suppressor agents through the inhibition of migration, suppression of cell cycle, and apoptosis induction.[90–92] Thus, to prevent therapy-induced tumor progression, QDs ought to act as theranostic agents, combining diagnostics due to PL and therapeutics due to the attachment of anticancer agents, for example, photosensitizers. Such complexes have been already designed and tested as effective tools for pancreatic cancer.[93]

Although we chose breast cancer as a tumor model, recent studies show the applicability of MSC-based therapy for the treatment of tumors of various locations, for example, ovarian,[94] liver,[46] lung,[95] and so on. A considerable amount of research has been done on glioma models, as MSCs are able to cross the blood–brain barrier and localize in intracranial neoplasms.[20,53,62]

Adipose tissue- or bone marrow-derived MSCs are most commonly used in tumor-tropic cell therapy researches. To our knowledge, we are the first ones to use skin connective tissue MSCs for tumor-tropic nanoparticle delivery. Using skin MSCs for the delivery of anticancer agents would be advantageous, since the skin tissue composes the widest area and has the easiest accessibility in the human body.

Conclusion

In this study, we tested the ability of skin-derived MSCs to be used as cellular nanoparticle vehicles and evaluated their tumor-tropic migration toward breast cancer cells in vitro and in vivo. We demonstrated that skin connective tissue MSCs are able to selectively deliver QDs to human tumor xenograft models. To our knowledge, this is the first time that skin MSCs have been used in tumor-tropic in vitro and in vivo studies. We suggest that QD-loaded skin MSCs could be a useful tool to target cancer cells. However, further studies are necessary.

Acknowledgments

This study was supported by the Lithuanian-Latvian-Taiwanese joint project Grant No TAP LLT 03/2014 and State Research program 'Improvement of early cancer diagnostics' approved by the Ministry of Education and Science of Lithuania (No V-273). We are very grateful to Vilius Poderys for measuring QD size distribution using atomic force microscopy and dynamic light scattering.

Disclosure

The authors report no conflicts of interest in this work.

References

1. Pattabiraman DR, Weinberg RA. Tackling the cancer stem cells-what challenges do they pose? *Nat Rev Drug Discov*. 2014;13(7):497–512.
2. Wei X, Yang X, Han ZP, Qu FF, Shao L, Shi YF. Mesenchymal stem cells: a new trend for cell therapy. *Acta Pharmacol Sin*. 2013;34(6):747–754.
3. Barkholt L, Flory E, Jekerle V, et al. Risk of tumorigenicity in mesenchymal stromal cell-based therapies-bridging scientific observations and regulatory viewpoints. *Cytotherapy*. 2013;15(7):753–759.
4. Ren G, Chen X, Dong F, et al. Concise review: mesenchymal stem cells and translational medicine: emerging issues. *Stem Cell Transl Med*. 2012;1(1):51–58.
5. Williams AR, Hare JM. Mesenchymal stem cells biology, pathophysiology, translational findings, and therapeutic implications for cardiac disease. *Circ Res*. 2011;109(8):923–940.
6. Rojas M, Gupta N, Majka SM. Mesenchymal Stem Cells: Complex Players in Lung Repair and Injury. In: Hayat MA, ed. *Stem Cells and Cancer Stem Cells, Volume 7: Therapeutic Applications in Disease and Injury*. Dordrecht: Springer Netherlands; 2012:145–154.
7. Wang S, Hu F, Li J, et al. Design of electrospun nanofibrous mats for osteogenic differentiation of mesenchymal stem cells. *Nanomedicine*. Epub 2017 May 26.
8. Uccelli A, Moretta L, Pistoia V. Mesenchymal stem cells in health and disease. *Nat Rev Immunol*. 2008;8(9):726–736.
9. Arwert EN, Hoste E, Watt FM. Epithelial stem cells, wound healing and cancer. *Nat Rev Cancer*. 2012;12(3):170–180.
10. Dvorak HF. Tumors: wounds that do not heal-redux. *Cancer Immunol Res*. 2015;3(1):1–11.
11. Jung Y, Kim JK, Shiozawa Y, et al. Recruitment of mesenchymal stem cells into prostate tumours promotes metastasis. *Nat Commun*. 2013;4:1795.
12. Hocking AM. The role of chemokines in mesenchymal stem cell homing to wounds. *Adv Wound Care (New Rochelle)*. 2015;4(11):623–630.
13. Lourenco S, Teixeira VH, Kalber T, Jose RJ, Floto RA, Janes SM. Macrophage migration inhibitory factor-CXCR4 is the dominant chemotactic axis in human mesenchymal stem cell recruitment to tumors. *J Immunol*. 2015;194(7):3463–3474.
14. Xin H, Kanehira M, Mizuguchi H, et al. Targeted delivery of CX3CL1 to multiple lung tumors by mesenchymal stem cells. *Stem cells*. 2007;25(7):1618–1626.
15. Kosztowski T, Zaidi HA, Quinones-Hinojosa A. Applications of neural and mesenchymal stem cells in the treatment of gliomas. *Expert Rev Anticancer Ther*. 2009;9(5):597–612.

16. Suzuki T, Kawamura K, Li Q, et al. Mesenchymal stem cells are efficiently transduced with adenoviruses bearing type 35-derived fibers and the transduced cells with the IL-28A gene produces cytotoxicity to lung carcinoma cells co-cultured. *BMC Cancer*. 2014;14:713.
17. Zhang TY, Huang B, Yuan ZY, Hu YL, Tabata Y, Gao JQ. Gene recombinant bone marrow mesenchymal stem cells as a tumor-targeted suicide gene delivery vehicle in pulmonary metastasis therapy using non-viral transfection. *Nanomedicine*. 2014;10(1):257–267.
18. Kucerova L, Altanerova V, Matuskova M, Tyciakova S, Altaner C. Adipose tissue-derived human mesenchymal stem cells mediated prodrug cancer gene therapy. *Cancer Res*. 2007;67(13):6304–6313.
19. Zhang X, Yao S, Liu C, Jiang Y. Tumor tropic delivery of doxorubicin-polymer conjugates using mesenchymal stem cells for glioma therapy. *Biomaterials*. 2015;39:269–281.
20. Roger M, Clavreul A, Venier-Julienne MC, et al. Mesenchymal stem cells as cellular vehicles for delivery of nanoparticles to brain tumors. *Biomaterials*. 2010;31(32):8393–8401.
21. Huang X, Zhang F, Wang H, et al. Mesenchymal stem cell-based cell engineering with multifunctional mesoporous silica nanoparticles for tumor delivery. *Biomaterials*. 2013;34(7):1772–1780.
22. Zrazhevskiy P, Gao X. Quantum dot imaging platform for single-cell molecular profiling. *Nat Commun*. 2013;4:1619.
23. Maestro LM, Ramirez-Hernandez JE, Bogdan N, et al. Deep tissue bioimaging using two-photon excited CdTe fluorescent quantum dots working within the biological window. *Nanoscale*. 2012;4(1):298–302.
24. Wegner KD, Hildebrandt N. Quantum dots: bright and versatile in vitro and in vivo fluorescence imaging biosensors. *Chem Soc Rev*. 2015;44(14):4792–4834.
25. Rak-Raszewska A, Marcello M, Kenny S, Edgar D, Sée V, Murray P. Quantum dots do not affect the behaviour of mouse embryonic stem cells and kidney stem cells and are suitable for short-term tracking. *PLoS One*. 2012;7(3):e32650.
26. Ho IA, Toh HC, Ng WH, et al. Human bone marrow-derived mesenchymal stem cells suppress human glioma growth through inhibition of angiogenesis. *Stem Cells*. 2013;31(1):146–155.
27. Kidd S, Spaeth E, Dembinski JL, et al. Direct evidence of mesenchymal stem cell tropism for tumor and wounding microenvironments using in vivo bioluminescent imaging. *Stem Cells*. 2009;27(10):2614–2623.
28. Ghaedi M, Soleimani M, Taghvaie NM, et al. Mesenchymal stem cells as vehicles for targeted delivery of anti-angiogenic protein to solid tumors. *J Gene Med*. 2011;13(3):171–180.
29. Ding D, Mao D, Li K, et al. Precise and long-term tracking of adipose-derived stem cells and their regenerative capacity via superb bright and stable organic nanodots. *ACS Nano*. 2014;8(12):12620–12631.
30. Pendleton C, Li Q, Chesler DA, Yuan K, Guerrero-Cazares H, Quinones-Hinojosa A. Mesenchymal stem cells derived from adipose tissue vs bone marrow: in vitro comparison of their tropism towards gliomas. *PLoS One*. 2013;8(3):e58198.
31. Potdar PD, Prasannan P. Differentiation of human dermal mesenchymal stem cells into cardiomyocytes by treatment with 5-azacytidine: concept for regenerative therapy in myocardial infarction. *ISRN Stem Cells*. 2013;2013:9.
32. Mahmoudifar N, Doran PM. Mesenchymal Stem Cells Derived from Human Adipose Tissue. In: Doran MP, ed. *Cartilage Tissue Engineering: Methods and Protocols*. New York, NY: Springer New York; 2015:53–64.
33. Brückner S, Tautenhahn HM, Winkler S, et al. Isolation and hepatocyte differentiation of mesenchymal stem cells from porcine bone marrow "surgical waste" as a novel MSC source. *Transplant Proc*. 2013;45(5):2056–2058.
34. Jackson WM, Aragon AB, Djouad F, et al. Mesenchymal progenitor cells derived from traumatized human muscle. *J Tissue Eng Regen Med*. 2009;3(2):129–138.
35. Riekstina U, Cakstina I, Parfejevs V, et al. Embryonic stem cell marker expression pattern in human mesenchymal stem cells derived from bone marrow, adipose tissue, heart and dermis. *Stem Cell Rev*. 2009;5(4):378–386.
36. Dominici M, Le Blanc K, Mueller I, et al. Minimal criteria for defining multipotent mesenchymal stromal cells. The International Society for Cellular Therapy position statement. *Cytotherapy*. 2006;8(4):315–317.
37. Riekstina U, Parfejevs V, Muceniece R, Cakstina I, Boroduskis M, Ancans J. FGF-2 Effect on the Self-Renewal of Human Dermal Stem Cell Population in vitro. *Medicine*. 2009;7502009:117–128.
38. Saulite L, Dapkute D, Pleiko K, et al. Nano-engineered skin mesenchymal stem cells: potential vehicles for tumour-targeted quantum-dot delivery. *Beilstein J Nanotechnol*. 2017;8:1218–1230.
39. Chellappa M, Anjaneyulu U, Manivasagam G, Vijayalakshmi U. Preparation and evaluation of the cytotoxic nature of TiO(2) nanoparticles by direct contact method. *Int J Nanomedicine*. 2015;10(Suppl 1):31–41.
40. Chung TH, Wu SH, Yao M, et al. The effect of surface charge on the uptake and biological function of mesoporous silica nanoparticles in 3T3-L1 cells and human mesenchymal stem cells. *Biomaterials*. 2007;28(19):2959–2966.
41. Huang DM, Hung Y, Ko BS, et al. Highly efficient cellular labeling of mesoporous nanoparticles in human mesenchymal stem cells: implication for stem cell tracking. *FASEB J*. 2005;19(14):2014–2016.
42. Lu CW, Hung Y, Hsiao JK, et al. Bifunctional magnetic silica nanoparticles for highly efficient human stem cell labeling. *Nano Lett*. 2007;7(1):149–154.
43. Damalakiene L, Karabanovas V, Bagdonas S, Valius M, Rotomskis R. Intracellular distribution of nontargeted quantum dots after natural uptake and microinjection. *Int J Nanomedicine*. 2013;8:555–568.
44. Song C, Li G. CXCR4 and matrix metalloproteinase-2 are involved in mesenchymal stromal cell homing and engraftment to tumors. *Cytotherapy*. 2011;13(5):549–561.
45. Shah K. Mesenchymal stem cells engineered for cancer therapy. *Adv Drug Deliv Rev*. 2012;64(8):739–748.
46. Gao Y, Zhou Z, Lu S, et al. Chemokine CCL15 mediates migration of human bone marrow-derived mesenchymal stem cells toward hepatocellular carcinoma. *Stem Cells*. 2016;34(4):1112–1122.
47. Nakamura H, Jun F, Maeda H. Development of next-generation macromolecular drugs based on the EPR effect: challenges and pitfalls. *Expert Opin Drug Deliv*. 2015;12(1):53–64.
48. Durymanov MO, Rosenkranz AA, Sobolev AS. Current approaches for improving intratumoral accumulation and distribution of nanomedicines. *Theranostics*. 2015;5(9):1007–1020.
49. Pang L, Cui H, Liu Y, Zhong W. Anti-VEGF antibody conjugated CdHgTe quantum dots as a fluorescent probe for imaging in living mouse. *J Lumin*. 2016;173:274–278.
50. Steponkiene S, Dapkute D, Riekstina U, Rotomskis R. Accumulation and distribution of non-targeted and Anti-CD44-conjugated quantum dots in distinct phenotypes of breast cancer. *J Nanomed Nanotechnol*. 2015;6(6):1000341.
51. Dragu DL, Necula LG, Bleotu C, Diaconu CC, Chivu-Economescu M. Therapies targeting cancer stem cells: current trends and future challenges. *World J Stem Cells*. 2015;7(9):1185–1201.
52. Schmidt A, Ladage D, Steingen C, et al. Mesenchymal stem cells transmigrate over the endothelial barrier. *Eur J Cell Biol*. 2006;85(11):1179–1188.
53. Liu L, Eckert MA, Riazifar H, Kang DK, Agalliu D, Zhao W. From blood to the brain: can systemically transplanted mesenchymal stem cells cross the blood-brain barrier? *Stem Cells Int*. 2013;2013:435093.
54. Li L, Guan Y, Liu H, et al. Silica nanorattle-doxorubicin-anchored mesenchymal stem cells for tumor-tropic therapy. *ACS Nano*. 2011;5(9):7462–7470.
55. Cheng H, Kastrup CJ, Ramanathan R, et al. Nanoparticulate cellular patches for cell-mediated tumoritropic delivery. *ACS Nano*. 2010;4(2):625–631.
56. Ranjbarvaziri S, Kiani S, Akhlaghi A, Vosough A, Baharvand H, Aghdami N. Quantum dot labeling using positive charged peptides in human hematopoetic and mesenchymal stem cells. *Biomaterials*. 2011;32(22):5195–5205.

57. Muller-Borer BJ, Collins MC, Gunst PR, Cascio WE, Kypson AP. Quantum dot labeling of mesenchymal stem cells. *J Nanobiotechnology*. 2007;5:9.
58. Pietilä M, Lehenkari P, Kuvaja P, et al. Mortalin antibody-conjugated quantum dot transfer from human mesenchymal stromal cells to breast cancer cells requires cell–cell interaction. *Exp Cell Res*. 2013;319(18):2770–2780.
59. Anselmo AC, Mitragotri S. Cell-mediated delivery of nanoparticles: taking advantage of circulatory cells to target nanoparticles. *J Control Release*. 2014;190:531–541.
60. Fröhlich E. The role of surface charge in cellular uptake and cytotoxicity of medical nanoparticles. *Int J Nanomedicine*. 2012;7:5577–5591.
61. Barcellos-de-Souza P, Comito G, Pons-Segura C, et al. Mesenchymal stem cells are recruited and activated into carcinoma-associated fibroblasts by prostate ancer microenvironment-derived TGF-β1. *Stem Cells*. 2016;34(10):2536–2547.
62. Nakamizo A, Marini F, Amano T, et al. Human bone marrow-derived mesenchymal stem cells in the treatment of gliomas. *Cancer Res*. 2005;65(8):3307–3318.
63. Niu CS, Dong YF, Gao G. Vascular endothelial growth factor/platelet-derived growth factor receptor pathway is involved in bone marrow mesenchymal stem cell differentiation and directional migration toward gliomas. *Neural Regen Res*. 2010;5(13):993–998.
64. Ritter E, Perry A, Yu J, Wang T, Tang L, Bieberich E. Breast cancer cell-derived fibroblast growth factor 2 and vascular endothelial growth factor are chemoattractants for bone marrow stromal stem cells. *Ann Surg*. 2008;247(2):310–314.
65. Sun Z, Wang S, Zhao RC. The roles of mesenchymal stem cells in tumor inflammatory microenvironment. *J Hematol Oncol*. 2014;7(1):14.
66. Dwyer RM, Potter-Beirne SM, Harrington KA, et al. Monocyte chemotactic protein-1 secreted by primary breast tumors stimulates migration of mesenchymal stem cells. *Clin Cancer Res*. 2007;13(17):5020–5027.
67. Ehtesham M, Yuan X, Kabos P, et al. Glioma tropic neural stem cells consist of astrocytic precursors and their migratory capacity is mediated by CXCR4. *Neoplasia*. 2004;6(3):287–293.
68. Karp JM, Leng Teo GS. Mesenchymal stem cell homing: the devil is in the details. *Cell Stem Cell*. 2009;4(3):206–216.
69. Marquez-Curtis LA, Janowska-Wieczorek A. Enhancing the migration ability of mesenchymal stromal cells by targeting the SDF-1/CXCR4 Axis. *Biomed Res Int*. 2013;2013:561098.
70. Dillenburg-Pilla P, Patel V, Mikelis CM, et al. SDF-1/CXCL12 induces directional cell migration and spontaneous metastasis via a CXCR4/G alpha i/mTORC1 axis. *FASEB J*. 2015;29(3):1056–1068.
71. Park SA, Ryu CH, Kim SM, et al. CXCR4-transfected human umbilical cord blood-derived mesenchymal stem cells exhibit enhanced migratory capacity toward gliomas. *Int J Oncol*. 2011;38(1):97–103.
72. Shen C, Lie P, Miao T, et al. Conditioned medium from umbilical cord mesenchymal stem cells induces migration and angiogenesis. *Mol Med Rep*. 2015;12(1):20–30.
73. Shi M, Li J, Liao L, et al. Regulation of CXCR4 expression in human mesenchymal stem cells by cytokine treatment: role in homing efficiency in NOD/SCID mice. *Haematologica*. 2007;92(7):897–904.
74. Feng Y, Zhu M, Dangelmajer S, et al. Hypoxia-cultured human adipose-derived mesenchymal stem cells are non-oncogenic and have enhanced viability, motility, and tropism to brain cancer. *Cell Death Dis*. 2015;6:e1797.
75. Kean TJ, Lin P, Caplan AI, Dennis JE. MSCs: delivery routes and engraftment, cell-targeting strategies, and immune modulation. *Stem Cells Int*. 2013;2013:732742.
76. Sohni A, Verfaillie CM. Mesenchymal stem cells migration homing and tracking. *Stem Cells Int*. 2013;2013:130763.
77. Pi QM, Zhang WJ, Zhou GD, Liu W, Cao Y. Degradation or excretion of quantum dots in mouse embryonic stem cells. *BMC Biotechnol*. 2010;10:36.
78. Rosen AB, Kelly DJ, Schuldt AJ, et al. Finding fluorescent needles in the cardiac haystack: tracking human mesenchymal stem cells labeled with quantum dots for quantitative in vivo three-dimensional fluorescence analysis. *Stem Cells*. 2007;25(8):2128–2138.
79. Slotkin JR, Chakrabarti L, Dai HN, et al. In vivo quantum dot labeling of mammalian stem and progenitor cells. *Dev Dyn*. 2007;236(12):3393–3401.
80. Paris JL, de la Torre P, Manzano M, Victoria Cabanas M, Flores AI, Vallet-Regi M. Decidua-derived mesenchymal stem cells as carriers of mesoporous silica nanoparticles. In vitro and in vivo evaluation on mammary tumors. *Acta Biomater*. 2016;33:275–282.
81. Sadhukha T, O'Brien TD, Prabha S. Nano-engineered mesenchymal stem cells as targeted therapeutic carriers. *J Control Release*. 2014;196:243–251.
82. Kraitchman DL, Tatsumi M, Gilson WD, et al. Dynamic imaging of allogeneic mesenchymal stem cells trafficking to myocardial infarction. *Circulation*. 2005;112(10):1451–1461.
83. Gao J, Dennis JE, Muzic RF, Lundberg M, Caplan AI. The dynamic in vivo distribution of bone marrow-derived mesenchymal stem cells after infusion. *Cells Tissues Organs*. 2001;169(1):12–20.
84. Ren C, Kumar S, Chanda D, et al. Cancer gene therapy using mesenchymal stem cells expressing interferon-β in a mouse prostate cancer lung metastasis model. *Gene Ther*. 2008;15(21):1446–1453.
85. Mouiseddine M, Francois S, Semont A, et al. Human mesenchymal stem cells home specifically to radiation-injured tissues in a non-obese diabetes/severe combined immunodeficiency mouse model. *Br J Radiol*. 2007;80(Spec No 1):S49–S55.
86. Yun JW, Ahn JH, Kwon E, et al. Human umbilical cord-derived mesenchymal stem cells in acute liver injury: Hepatoprotective efficacy, subchronic toxicity, tumorigenicity, and biodistribution. *Regul Toxicol Pharmacol*. 2016;81:437–447.
87. Karnoub AE, Dash AB, Vo AP, et al. Mesenchymal stem cells within tumour stroma promote breast cancer metastasis. *Nature*. 2007;449(7162):557–563.
88. Huang WH, Chang MC, Tsai KS, Hung MC, Chen HL, Hung SC. Mesenchymal stem cells promote growth and angiogenesis of tumors in mice. *Oncogene*. 2013;32(37):4343–4354.
89. Luo J, Ok Lee S, Liang L, et al. Infiltrating bone marrow mesenchymal stem cells increase prostate cancer stem cell population and metastatic ability via secreting cytokines to suppress androgen receptor signaling. *Oncogene*. 2014;33(21):2768–2778.
90. Clarke MR, Imhoff FM, Baird SK. Mesenchymal stem cells inhibit breast cancer cell migration and invasion through secretion of tissue inhibitor of metalloproteinase-1 and -2. *Mol Carcinog*. 2015;54(10):1214–1219.
91. Sun B, Roh KH, Park JR, et al. Therapeutic potential of mesenchymal stromal cells in a mouse breast cancer metastasis model. *Cytotherapy*. 2009;11(3):289–298.
92. Zhu Y, Sun Z, Han Q, et al. Human mesenchymal stem cells inhibit cancer cell proliferation by secreting DKK-1. *Leukemia*. 2009;23(5):925–933.
93. Steponkiene S, Valanciunaite J, Skripka A, Rotomskis R. Cellular uptake and photosensitizing properties of quantum dot-chlorin e6 complex: in vitro study. *J Biomed Nanotechnol*. 2014;10(4):679–686.
94. Dembinski JL, Wilson SM, Spaeth EL, et al. Tumor stroma engraftment of gene-modified mesenchymal stem cells as anti-tumor therapy against ovarian cancer. *Cytotherapy*. 2013;15(1):20–32.
95. Kolluri KK, Laurent GJ, Janes SM. Mesenchymal stem cells as vectors for lung cancer therapy. *Respiration*. 2013;85(6):443–451.

Supplementary material

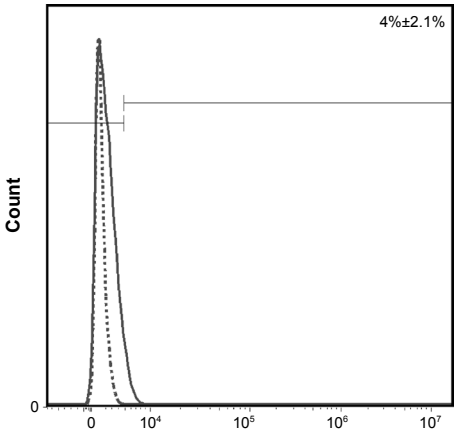

Figure S1 Flow cytometry histogram showing the amount of CXCR4 on the surface of skin-derived MSCs.
Notes: Dotted line, negative control; solid line, CXCR4-PE labeled MSCs. Percentage shows positive events.
Abbreviations: CXCR4, chemokine (C-X-C motif) receptor 4; MSCs, mesenchymal stem cells; PE, phycoerythrin.

3 publikacija / 3rd publication

Nanoparticle delivery to metastatic breast cancer cells by nanoengineered mesenchymal stem cells

Saulite L, Pleiko K, Popena I, **Dapkute D**, Rotomskis R, Riekstina U.

Beilstein Journal of Nanotechnology **9**:321-332 (2018)

DOI: 10.3762/bjnano.9.32

BEILSTEIN JOURNAL OF NANOTECHNOLOGY

Nanoparticle delivery to metastatic breast cancer cells by nanoengineered mesenchymal stem cells

Liga Saulite[*1], Karlis Pleiko[1], Ineta Popena[1], Dominyka Dapkute[2,3], Ricardas Rotomskis[2,4] and Una Riekstina[1]

Full Research Paper

Open Access

Address:
[1]Faculty of Medicine, University of Latvia, Raina Blvd. 19, LV-1586 Riga, Latvia, [2]Biomedical Physics Laboratory, National Cancer Institute, P. Baublio Street 3b, LT-08406 Vilnius, Lithuania, [3]Life Science Center, Vilnius University, Sauletekio Ave. 7, LT-10257 Vilnius, Lithuania, and [4]Laser Research Centre, Vilnius University, Sauletekio al. 9, corp. 3, LT-10222 Vilnius, Lithuania

Email:
Liga Saulite[*] - liga.saulite@lu.lv

* Corresponding author

Keywords:
cancer; mesenchymal stem cells; quantum dots; spheroids; 3D cell culture

Beilstein J. Nanotechnol. **2018,** *9,* 321–332.
doi:10.3762/bjnano.9.32

Received: 19 June 2017
Accepted: 02 January 2018
Published: 29 January 2018

Associate Editor: M. Stenzel

Abstract

We created a 3D cell co-culture model by combining nanoengineered mesenchymal stem cells (MSCs) with the metastatic breast cancer cell line MDA-MD-231 and primary breast cancer cell line MCF7 to explore the transfer of quantum dots (QDs) to cancer cells. First, the optimal conditions for high-content QD loading in MSCs were established. Then, QD uptake in breast cancer cells was assessed after 24 h in a 3D co-culture with nanoengineered MSCs. We found that incubation of MSCs with QDs in a serum-free medium provided the best accumulation results. It was found that 24 h post-labelling QDs were eliminated from MSCs. Our results demonstrate that breast cancer cells efficiently uptake QDs that are released from nanoengineered MSCs in a 3D co-culture. Moreover, the uptake is considerably enhanced in metastatic MDA-MB-231 cells compared with MCF7 primary breast cancer cells. Our findings suggest that nanoengineered MSCs could serve as a vehicle for targeted drug delivery to metastatic cancer.

Introduction

The recent progress in the development of nanoscale agents opens up new perspectives for targeted drug delivery in cancer diagnostics, imaging and therapy. However, once administered into the body, nanoparticles (NPs) are rapidly phagocytosed by the macrophages and sequestered in the liver, spleen, and lymph nodes [1,2]. To overcome this hurdle, targeted drug delivery using nanoengineered cells with cancer homing capability has emerged as an alternative approach. Based on the characteristic tumour tropism, integration in tumour stroma and their immune privileged nature, mesenchymal stem cells (MSCs) can be used as a delivery vehicle for therapeutic and imaging agents, such as drug-conjugated NPs [3,4]. MSCs are adult stem cells that can

be isolated from various organs, including brain, liver, kidney, lung, bone marrow, muscle, thymus, skin, adipose tissue, umbilical cord and placenta [5]. MSCs express CD105 (SH2 or endoglin), CD73 (SH3 and SH4), CD106 (VCAM-1), CD44 (hyaluronic acid receptor), CD90 (Thy 1.1), CD29, CD146 and CD166 surface markers and can be induced to differentiate in vitro into diverse lineages of mesodermal origin, such as adipogenic, osteogenic and chondrogenic cells [6].

MSC-based therapies are being increasingly investigated for their promising potential in cancer diagnostics and treatment [5,7,8]. In vivo studies have demonstrated that MSCs can effectively deliver nanorattle-encapsulated doxorubicin to U251 glioma cells and induce cancer cell apoptosis [9]. Moreover, MSCs carrying poly(lactic-*co*-glycolic acid) (PLGA) NPs linked with paclitaxel selectively accumulate in an orthotopic A549 lung tumour model [2]. It has been reported that IFN-beta secreting MSCs could integrate into A375SM melanoma tumours to inhibit the growth of cancer cells [10]. Bioluminescent imaging has demonstrated the MSC tumour homing ability in an in vivo xenogeneic breast carcinoma and ovarian tumour model [11]. Lourenco et al. demonstrated that the tumour homing capability in MSCs is induced by MIF–CXCR4 chemotaxis and downstream activation of the MAPK pathway [12]. QD-loaded MSCs have shown to migrate towards tumours and metastases in human breast tumour bearing mice [13].

It is generally accepted that 3D cell cultures are more similar to the composition of tumour microenvironment in vivo compared with 2D cell cultures [14-16]. Moreover, in vitro 3D cultures could fill the gap between 2D in vitro testing and in vivo animal models [17,18]. Spheroid-based 3D models are widely used to test cancer cell growth/proliferation, invasion, angiogenesis, and immune interactions and have been employed in drug screening and the development of new therapies [15,16]. Generally, a nonadherent surface coating (i.e., polyHEMA), hanging-drop assay or microfluidic devices are used to induce spheroid formation [16,19-21].

In the current study, we established a 3D co-culture model using QD-labelled MSCs to verify nanoparticle transfer between stromal and cancer cells in close spatial proximity. QDs are semiconductor nanocrystals with improved light emission, signal brightness, and resistance to photobleaching, thus making them a suitable imaging agent for the modelling of nanoparticle transfer [22].

The aim of the study was to demonstrate that nanoengineered MSCs can serve as a delivery vehicle to target breast cancer cells in a 3D co-culture model.

Results

Optimal quantum dot labelling conditions in mesenchymal stem cells

The flow cytometry data revealed that MSCs incubated in serum-free conditions accumulated more QDs compared with cells incubated in complete medium. At a QD concentration of 2 nM, 100% of the cells were labelled with QDs in serum-free medium, whereas a 100% positive cell population was achieved after incubation with 16 nM QDs in complete medium (Figure 1A). Fluorescence intensity analysis revealed that the QDs accumulated in the cells in a concentration-dependent manner. MSCs incubated with QDs diluted in the serum-free medium accumulated 100-fold more QDs compared with the complete medium (Figure 1B). Under serum-free conditions, QD uptake saturation was achieved at 16 nM, whereas no saturation was achieved in cells incubated with QDs in complete medium even at a concentration of 32 nM (Figure 1B).

Next, we analysed the MSC viability in response to intracellular QD accumulation. Incubation time points were selected at 24 h and 48 h to identify the QD-induced cytotoxic effects. We did not observe any cytotoxic effect on MSC viability when the QDs were applied in complete medium (Figure 1C). On the contrary, due to the 100-fold increase in the QD accumulation ratio under serum-free conditions, the QD toxicity was observed after 24 h of incubation with 32 nM and 64 nM QD by 30% and 50%, respectively (Figure 1D). Interestingly, the cytotoxic effect was not observed after 48 h of incubation with QDs, which could be explained by the reduction of intracellular QD concentration due to cell division. Thus, we chose a QD concentration of 16 nM as the optimal concentration for the labelling of cells in complete medium, whereas 8 nM was optimal for cell labelling in serum-free medium.

Mesenchymal stem cell 3D culture model

MSC aggregation could be observed 3–6 h after seeding on poly(2-hydroxethyl methacrylate) (polyHEMA)-coated plates. 24 h later, the cells formed compact and dense floating spheroids of 100 μm in diameter (Figure 2A,B). The diameter of the spheroids further increased after 48 and 72 h (Figure 2A,B). Z-scan measurements revealed that live cells were present throughout the spheroid structure after 24 h of incubation (Supporting Information File 1, Figure S2).

CD90 was used as a selective marker for MSCs because it is not expressed in MCF7 and MDA-MB-231 cells [23]. To ensure the stability of the selective marker, the expression of CD90 in 3D MSC culture was monitored over time. After 24 h in spheroid culture, 97% of MSCs remained CD90 positive, which was similar to 2D culture [24]. However, after 48 h, 72 h and 96 h prop-

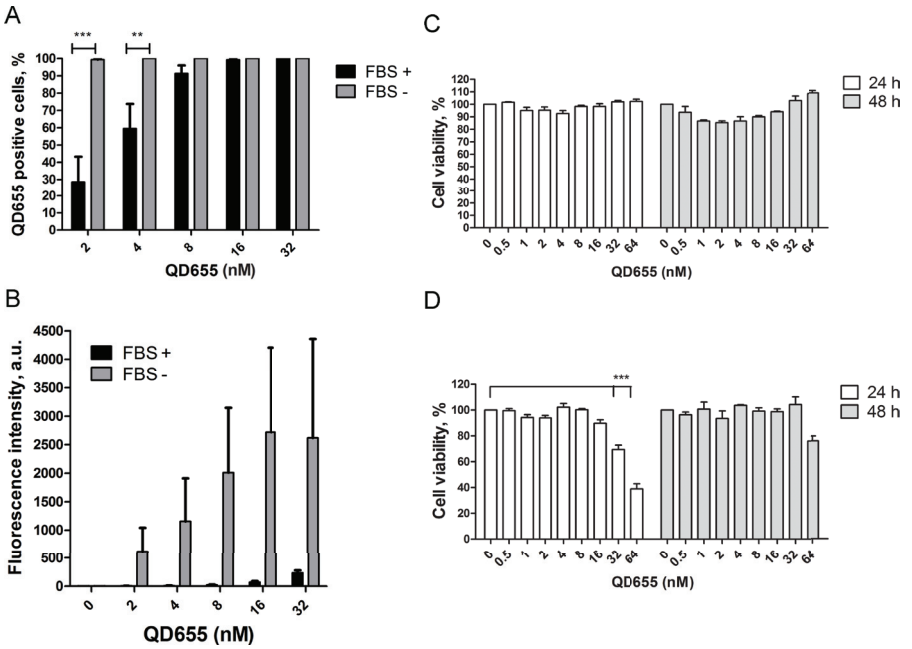

Figure 1: Characterisation of the optimal quantum dot (QD) incubation conditions in mesenchymal stem cells (MSCs). QD uptake after 6 h of incubation in MSCs cultivated in complete or serum-free medium expressed as the percentage of QD-positive cells (A) and the QD accumulation intensity (B). The impact of QDs on MSC viability after labelling in complete (C) and serum-free (D) medium following incubation for 24 h and 48 h. ***p*-value < 0.01, ****p*-value < 0.001.

agation on polyHEMA coatings, CD90 expression was reduced to 92%, 81% and 88%, respectively (Figure 2C). Therefore, we chose 24 h as the optimal incubation time for 3D cell co-culture experiments to ensure the selectivity of the CD90 marker towards MSCs.

Quantum dot signal stability in mesenchymal stem cell spheroids

Next, we sought to determine the stability of the QD label in MSC spheroids. QD release was estimated in MSCs that were labelled with QDs in complete or serum-free medium in 2D culture and seeded on polyHEMA coatings to form spheroids. After 24 h, only 56% of MSCs that were labelled with QDs in complete medium and formed 3D structures had retained the QD signal. Following 48 h and 72 h of incubation, the number of QD-labelled MSCs in 3D culture decreased further to 33% and 35%, respectively (Figure 3A). The rapid reduction in the QD signal after 24 h was confirmed by fluorescence intensity analysis (Figure 3B). On the contrary, 100% of MSCs that were labelled in serum-free conditions remained QD positive until 72 h of incubation (Figure 3C). Despite the fact that 100% of the MSC population was QD positive in serum-free medium until 72 h, we observed a 5.5-fold/5-fold decrease in the fluorescence intensity, respectively, indicating that QD elimination occurs (Figure 3D). As mentioned previously, a significantly increased intracellular accumulation of QDs was observed in serum-free medium (Figure 1A,B), and the QD elimination effect was subsequently more pronounced (Figure 3D). Thus, we chose to label MSCs with QDs in serum-free medium to ensure the highest load of intracellular QDs for further 3D co-culture experiments.

Quantum dot uptake in breast cancer cell 2D and 3D monocultures

MCF7 and MDA-MB-231 cells formed loose, floating aggregates in 3D culture conditions (Figure 4A). MCF7 and MDA-MB-231 cells were labelled with 8 nM QDs in 2D and 3D culture to evaluate the differences in uptake efficiency under both conditions. We observed that MCF7 cells exhibited increased QD internalisation efficiency in standard culture conditions (2D) compared with 3D culture (Figure 4B). To the contrary, MDA-MB-231 internalised 6-fold more QDs in 3D culture

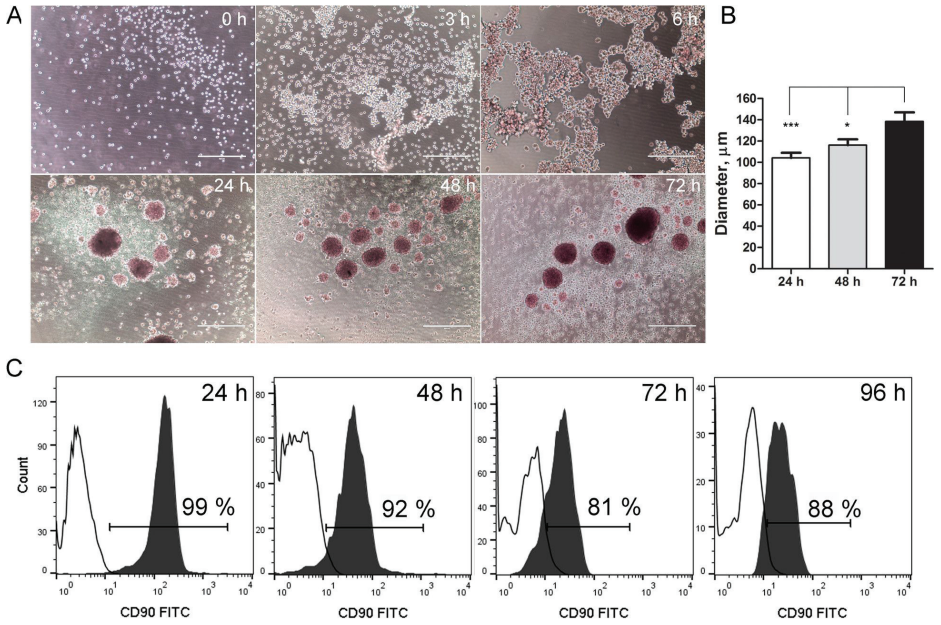

Figure 2: Characterisation of mesenchymal stem cells (MSCs) in 3D culture conditions. (A) MSC spheroid formation on polyHEMA coating. Scale bar – 400 µm. (B) The change in the diameter of MSC spheroids in 3D culture over time. (C) The dynamics of CD90 expression in 3D cultivated MSCs. **p*-value < 0.05, ****p*-value < 0.001.

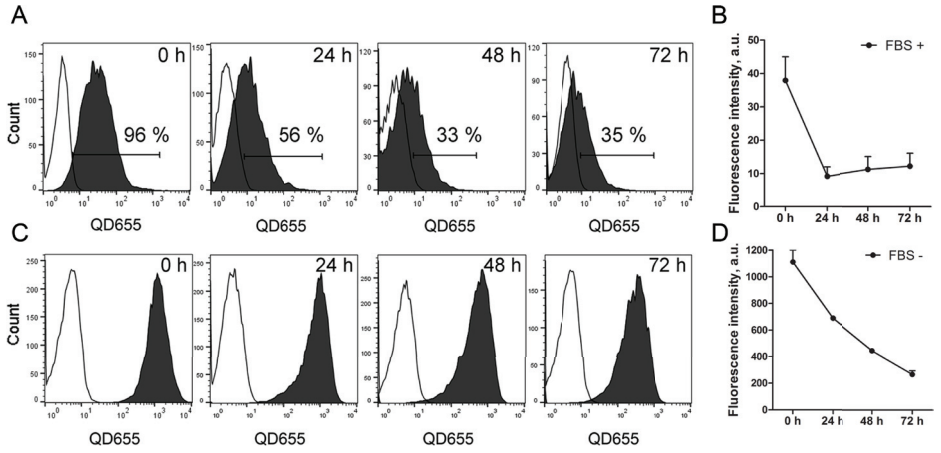

Figure 3: The dynamics of quantum dot (QD) signal in mesenchymal stem cells (MSCs) 3D culture. Representative data of MSC QD signal analysis in 3D culture after labelling in complete (A) or serum-free medium (C). The changes of the QD fluorescence signal intensity in the 3D MSC population after labelling in complete (B) and in serum-free (D) medium.

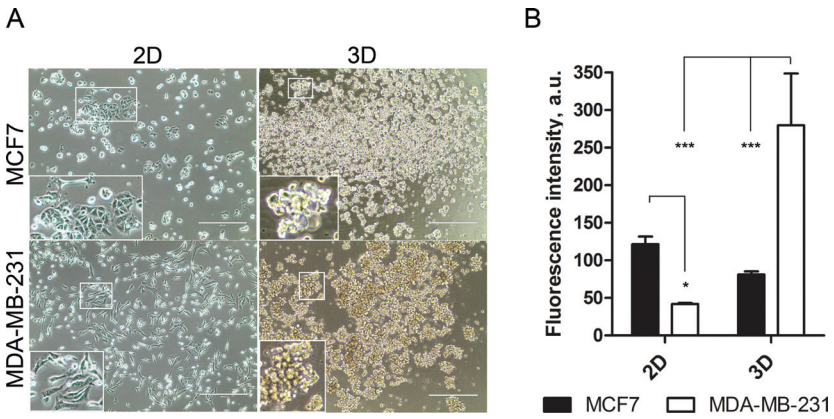

Figure 4: Comparison of MCF7 and MDA-MB-231 properties in 2D and 3D culture conditions. (A) The morphology of MCF7 and MDA-MB-231 cells in 2D and 3D culture. Scale bar – 400 μm. (B) Quantum dot (QD) uptake efficiency in MCF7 and MDA-MB-231 cells in 2D and 3D culture expressed as the intracellular QD fluorescence intensity. **p*-value < 0.05, ****p*-value < 0.001.

compared with 2D (Figure 4B). Such discrepancy in uptake efficacy might be associated with different endocytosis pathways. MCF7 cells internalised QDs through phagocytosis and clathrin/caveolae-dependent endocytosis, whereas the clathrin/caveolae-dependent pathway dominated in MDA-MB-231 cells in monocultures (Supporting Information File 1, Figure S2).

Cell viability in 3D culture

Cells in a 3D culture formed floating and dense spheroids. Therefore, we sought to analyse the effect of the 3D culture conditions on cell viability (Figure 5). MSC and breast cancer cell populations were distinguished by CD90 expression, thus allowing viability estimations in each cell type separately. Cell viability in 2D culture was greater than 95% (data not shown). MSCs cultivated in 3D monocultures were fully viable after 24 h; nevertheless, a distinct decrease in viability of 26% was observed after 48 h (Figure 5A). MCF7 and MDA-MB-231 cell viability was not changed after 24 h. However, after 48 h, the viability of MCF7 cells was reduced by 31% (Figure 5A). The viability of MDA-MB-231 cells remained unchanged after 24 h and 48 h in 3D culture (Figure 5A). In 3D co-culture, MSC/MCF7 viability after 24 h decreased by 9%, of which 2% accounted for MSCs and 7% for MCF7. In MSC/MDA-MB-231 co-culture, 11% of cells were dead, of which 6% were MSCs and 5% were MDA-MB-231 after 24 h of cultivation. The cell survival rate in co-culture decreased after 48 h of propagation. The viability of cells in MSC/MCF7 co-culture decreased by 23% (10% MSCs and 13% MCF7), whereas the

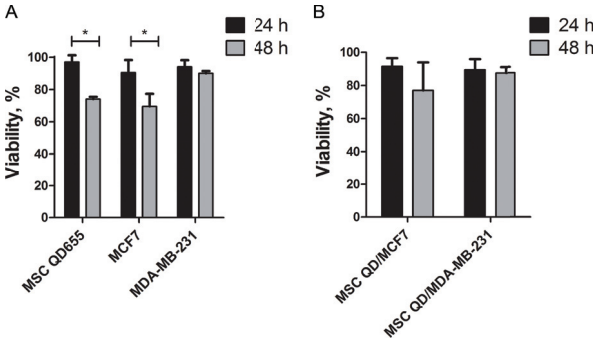

Figure 5: The viability of mesenchymal stem cells (MSCs), MCF7 and MDA-MB-231 cells in spheroids. The viability of cells was analysed in 3D monocultures (A) and 3D co-cultures (B) after 24 h and 48 h of cultivation on polyHEMA coatings. **p*-value < 0.05.

number of dead cells was 13% (6% MSCs and 7% MDA-MB-231) in MSC/MDA-MB-231 co-culture after 48 h. Viability was considered as another reason to select the 24 h incubation in 3D co-culture as the optimal time point for the study.

Quantum dot transfer from mesenchymal stem cells to cancer cells in 3D co-culture

The foremost aim of our study was to obtain experimental proof that nanoengineered MSCs could convey the QDs to the cancer cells in 3D co-culture conditions (Figure 6). Indeed, our data clearly demonstrate that after 24 h in 3D co-culture, 18% of MCF7 cells (Figure 6F) and 31% of MDA-MB-231 cells (Figure 6G) had internalised QDs as noted by the appearance of single QD label-positive cells in the lower right quadrant of the dot plot. Importantly, 96% of the QD-loaded MSC population was CD90 positive in 3D monoculture (Figure 6C). As expected, MCF7 (Figure 6D) and MDA-MB-231 cells (Figure 6E) were CD90 negative in 3D monocultures. The QD transfer from

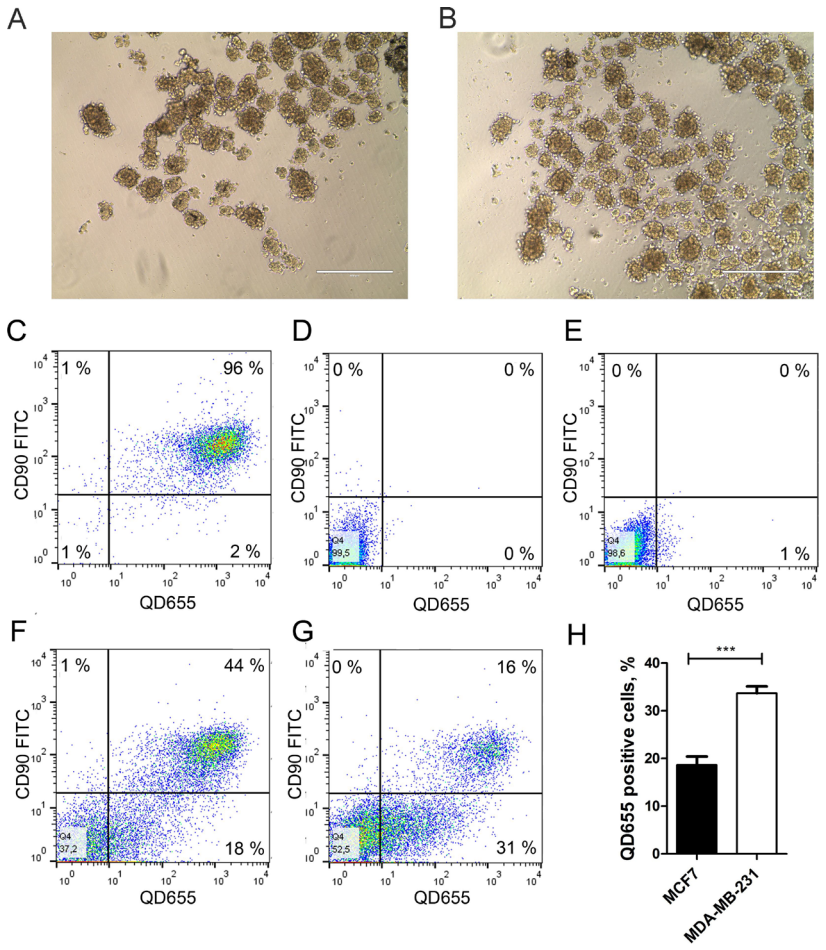

Figure 6: Quantum dot (QD) uptake in MCF7 and MDA-MB-231 cells in 3D co-culture. (A) Morphology of MSC/MCF7 and (B) MSC/MDA-MB-231 spheroids after 24 h of co-culture. Scale bar – 400 µm. (C) QD-loaded mesenchymal stem cells (MSCs), (D) MCF7 and (E) MDA-MB-231 cells were stained with CD90 to distinguish MSCs and cancer cell populations. Lower right quadrant in the dot plot shows the single QD positive population (QD-labelled cancer cells) in MSC/MCF7 (F) and MSC/MDA-MB-231 (G) 3D co-cultures. Representative data shown. (H) QD transfer efficiency from MSCs to cancer cells illustrated by the percentage of QD-positive/CD90-negative cells (n = 3). ***p-value < 0.001.

MSCs to cancer cells was also visualised by fluorescence imaging where CD90-negative/QD-positive cells represented cancer cells that have taken up the QDs released from MSCs during 3D co-culture (Figure 7). The proof of principle was additionally confirmed using cancer-cell-associated marker epithelial cell adhesion molecule (EpCAM) in nanoengineered MSC and MCF7 co-culture. Similarly to the previous data obtained with CD90 as a selective marker in the co-culture model, the QD transfer efficiency from nanoengineered MSCs to MCF7 cells was on average 18% (see Supporting Information File 1, Figure S3).

Discussion

MSCs and the cancer cell 3D co-culture model described in this study simulate tumour microenvironment conditions in vivo and allow the evaluation of nanoparticle transfer between different cell types. The most important finding in the current 3D co-culture model is that intercellular QD delivery occurs between nanoengineered MSCs and breast cancer cells. The transcellular crosstalk between stromal cells and breast cancer cells has been studied previously in MSC/MDA-MB-231 co-cultures using the hanging drop method [25]. Pietila et al. demonstrated that cell–cell interaction is required for mortalin-conjugated QD655 transfer from MSCs to cancer cells, whereas no QD transfer occurred in a trans-well 2D system lacking cell contact [25]. The direct intercellular transfer of mortalin–QD655 between MSCs and breast cancer cells occurred through the formation of nanotubes or cell–cell fusion [26-28]. Similarly, it has been previously reported that QDs are actively transported between cardiac myocytes using membrane nanotubes [29]. In our study, we demonstrate that MSCs efficiently uptake QDs in serum-free conditions and then excrete the QDs, which then accumulate in MDA-MB-231 and MCF7 breast cancer cell lines in the 3D co-culture (Figure 3C,D). Noteworthy is that the permeability glycoprotein (P-glycoprotein)-mediated excretion of QDs from stem cells has been reported in other studies [30-32]. In our co-culture model, QDs are likely lost from MSCs via P-glycoprotein excretion. In 3D co-culture, MSCs and cancer cells are in close spatial proximity (Figure 6A,B), thus facilitating the uptake of MSC-excreted QDs by cancer cells. Our data demonstrate that phagocytosis and clathrin/caveolae-dependent endocytosis are the major QD uptake pathways in MCF7 cells, whereas the clathrin/caveolae-dependent pathway dominated in MDA-MB-231 cells in monocultures (see Supporting Information File 1, Figure S1). These findings are consistent with previous studies that demonstrated clathrin-dependent endocytosis, micropinocytosis and caveolae-mediated endocytosis as the main routes for NP

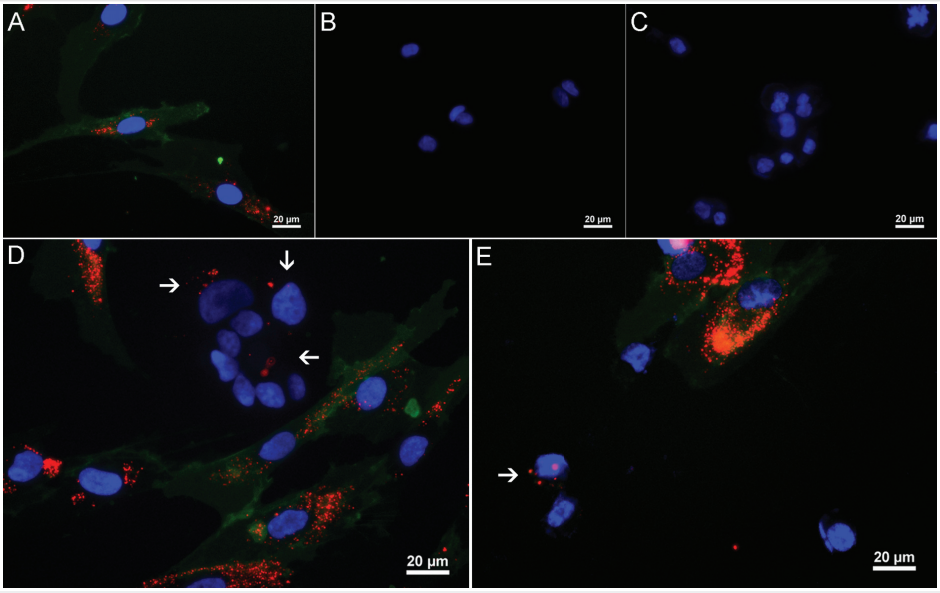

Figure 7: Fluorescence imaging of quantum dot (QD) intracellular accumulation in MCF7 and MDA-MB-231 cells during 3D co-culture. Nanoengineered MSCs (A), MCF7 (B) and MDA-MB-231 (C) cells were stained with CD90 FITC to distinguish cell populations. Single QD-positive/CD90-negative cells observed in MSC/MCF7 (D) and MSC/MDA-MB-231 (E) co-cultures. White arrows indicate cancer cells with internalised QDs. Blue – Hoechst, green – CD90 FITC, red – QDs. Scale bar – 20 µm.

uptake in MCF7 and MDA-MB-231 cells [33-35]. Nevertheless, we were not able to analyse the uptake pathway in 3D conditions likely due to poor inhibitor penetrance into the spheroids.

In general, 3D cultures are extensively studied given their potential to mimic cellular interactions and signal transduction occurring in in vivo conditions [14]. Briefly, 3D cell culture formation occurs on natural compounds, such as chitosan and hyaluronic acid, or synthetic agents, such as polyHEMA and poly(vinyl alcohol) (PVA) [14,36]. PolyHEMA has been widely used to induce spheroid formation in cancer cells and cells from healthy tissue [37,38]. Notably, the cell morphology and even phenotype changes in 3D culture comparing to the conventional 2D culture. We observed a decrease in the expression of CD90 following 48 h propagation in 3D conditions, which could be explained by a cell reaction to the change of the microenvironment or cell differentiation [39,40]. Similar effects were observed in bone marrow MSCs where CD29, CD44, CD73, CD90, and CD105 expression decreased after 7 days in 3D culture. To the contrary, haematopoietic marker CD34 and CD45 expression was increased [41]. CD90 is one of the key markers used for MSC characterisation [24]. In our hands Hoechst, 3,3'-dioctadecyloxacarbocyanine perchlorate (DiO), calcein, PKH67 and baculovirus gene transfer into mammalian cells (BacMam) transfection lacked cell type- selective specificity (data not shown). Thus, we used CD90 as a selective marker for MSCs because it is not expressed on MCF7 and MDA-MB-231 cells [23]. Additionally, we used EpCAM as a selective marker for breast cancer cells. It has been reported that the MSC marker expression profile can be changed in a co-culture with cancer cells and vice versa [28,42]. Slight CD90 expression can be induced in cancer cells after 48–72 h [28]. Similarly, cancer cell markers such as EpCAM can be induced in MSCs after 72 h of co-culture with breast cancer cells [42]. However, such marker induction has not been reported after 24 h of co-culture. Therefore, 24 h serve as a suitable co-culture time to analyse the QD transfer from MSCs to cancer cells. EpCAM expression was detected only in MCF7 cells and not in MDA-MB-231 cells, therefore the proof of principle of QD transfer from nanoengineered MSCs to breast cancer cells was demonstrated using MCF7 cells only (Supporting Information File 1, Figures S3 and S4).

Cell viability in spheroids is another critical issue that could affect the outcome of the co-culture experiment. In our study, we did not observe the formation of necrotic cells after 24 h (Supporting Information File 1, Figure S2), and cell viability was not affected (Figure 5). The size of the spheroids increased each day; therefore, a slight decrease in viability began after 48 h (Figure 5). The ability of the cells to survive in a 3D environment might be cell source dependent. For example, umbilical cord MSCs did not form necrotic zones up to 11 days in the 3D culture [43].

Metastatic cancer cells are resistant to extracellular matrix detachment-induced apoptosis (anoikis) [44]. Anoikis resistance therefore determines the cell survival and behaviour in a 3D culture. It was previously shown that MDA-MB-231 cells in 3D culture remains viable up to 48 h; however, remarkable MCF7 cell death occurs after 24 h in a 3D culture [45]. Despite the general assumption that the uptake processes of nutrients and NPs are reduced in 3D culture, our data indicate that QD accumulation is increased in MDA-MB-231 cells in 3D culture conditions compared with 2D (Figure 4B). The same tendency was also confirmed in our 3D co-culture study in which MDA-MB-231 cells internalised almost twice as much QDs compared with MCF7 cells (Figure 6F–H). Thus, we demonstrated that nanoengineered MSCs could be a tool for targeting metastatic breast cancer cells. It has been reported that metastatic breast cancer cells demonstrate higher nanocarrier uptake efficiency than MCF7 due to the overexpression of integrin receptors which mediate the uptake of NPs through integrin receptor mediated endocytosis [46].

Ex vivo injected MSCs have a relatively short lifespan within the body. On average, 24 h after the injection, these MSCs are relocated to the liver and spleen [47,48]. MSCs overexpress the drug efflux transporter P-glycoprotein, which ensures rapid excretion of toxic substances from MSCs. Thus, MSCs are an excellent vector for low cytotoxicity anticancer drugs [4]. Sadhukha et al. demonstrated that nanoengineered MSCs home to A549 lung cancer in vivo and remain there for at least 3 h, which could be sufficient time to release drugs into the tumour. The encapsulation of NP-linked anticancer drugs could ensure metered drug release in tumours [2]. QD linkage to photosensitisers, such as chlorin e_6, causes damage to MiaPaCa2 cancer cells via light-induced cytotoxicity, demonstrating a promising approach for NP-based cancer therapies [49]. These approaches indicate that MSCs could be used as potential drug delivery vectors in tumour therapies.

Conclusion

In summary, we demonstrated the feasibility of a 3D co-culture model to study targeted drug delivery by nanoengineered MSCs. For NP delivery purposes, MSC labelling with QDs in serum-free medium ensures increased loading efficiency. The QD transfer from MSCs is more efficient in co-culture with the metastatic breast cancer cell line MDA-MB-231 compared with non-metastatic MCF7 cells. Thus, nanoengineered MSCs could be considered as nanoparticle delivery vehicles to specifically target metastatic breast cancer cells.

Experimental

Cell culture

Primary human skin mesenchymal stem cells (MSCs) from frozen primary cell stock were used in accordance with authorised approval from the Institute of Experimental and Clinical Medicine Ethics Committee, University of Latvia (issued 04.06.2014) as described previously [24]. The cells were propagated in the medium Dulbecco's modified Eagle's medium/nutrient mixture F-12 (DMEM/F12) (3:1 v/v) supplemented with 10% of fetal bovine serum (FBS) and antibiotics (100 U/mL penicillin, 100 µg/mL streptomycin) (complete MSC medium). Cell suspensions were propagated in tissue culture flasks until 80% confluence in a humidified chamber at 37 °C with 5% CO_2. MSCs from passages 3 to 6 were used in experiments. The cells cultivated in complete or serum-free medium (DMEM/F12 3:1) were used for the experiments.

Human breast cancer cell lines MDA-MB-231 (ATCC HTB-26™) and MCF7 (ATCC HTB-22™) were propagated in DMEM supplemented with 10% FBS and penicillin/streptomycin (100 U/mL and 100 µg/mL, respectively) (complete cancer cell medium). The cells were cultured in 25 cm^2 polystyrene tissue culture flasks up to 90% confluence in complete cell culture medium in a humidified chamber at 37 °C with 5% CO_2.

For passaging, the cells were trypsinised using 0.25% trypsin–EDTA solution. All cell reagents were purchased from Sigma-Aldrich, St. Louis, MO, USA.

Establishment of 3D cell culture model

A poly(2-hydroxethyl methacrylate) (polyHEMA) coating was prepared as described elsewhere [50]. In brief, the PolyHEMA solution was poured into the wells of a 24-well tissue culture polystyrene plate to cover the surface. The plate was then air dried in a laminar airflow chamber overnight. The MSCs, MDA-MB-231 and MCF7 cells were seeded at a density 5×10^4 cells per well on polyHEMA-coated plates in the complete cell culture media. Then, the 3D spheroid formation was analysed using an EVOS XL light transmission microscope at 24, 48 and 72 h (AMG, Washington, USA).

To distinguish between cell populations in the co-culture, CD90 was chosen as a selective marker for MSCs and EpCAM was chosen as a marker for MCF7 cells. CD90 expression dynamics were analysed in MSCs after 24, 48, 72 and 96 h of propagation in 3D culture. The spheroids were pelleted by centrifugation at 250 g for 5 min, trypsinised for 5 min at 37 °C to obtain a single cell suspension, and finally centrifuged and suspended in 100 µL of PBS. The samples were stained with FITC mouse anti-human CD90 (clone 5E10, BD Bioscience, Carlsbad, CA, USA) or FITC mouse anti-human EpCAM (clone EBA-1, BD Bioscience, Carlsbad, CA, USA) for 30 min at room temperature. Flow cytometry data were acquired on a Guava EasyCyte 8HT flow cytometer and analysed by ExpressPro software (Millipore, MA, USA).

Quantum dots

Qdot® 655 ITK™ non-targeted carboxyl-coated quantum dots were purchased from Thermo Fisher Scientific, USA. The QDs are composed of a CdSe core and ZnS shell coated with an amphiphilic polymer and functionalised with carboxylate. The QDs have an emission maxima of 655 nm. Xu et al. reported that the hydrodynamic diameter of the nanoparticles is 14.55 ± 4.157 nm and the zeta potential is −35.1 mV [51]. The stock solution was prepared at a concentration of 8 µM in 50 mM borate with pH 9.0. Further preparations of the QD solution are described at each methodological part separately.

Preparation of nanoengineered cells

Carboxyl QD655 (Thermo Fisher Scientific, Waltham, Massachusetts, USA) was used in the study. To estimate the optimal QD concentration for uptake experiments, 5×10^4 MSCs were allowed to adhere to 6-well tissue culture polystyrene (TCPS) plates and cultured in the presence of QDs of 2 nM to 32 nM concentration for 6 h in complete or serum-free medium. The cells were then harvested by trypsinisation and resuspended in 200 µL PBS for further studies.

Cell viability assay

The effect of QDs on MSC viability was analysed using the cell counting kit 8 (CCK8) (Sigma-Aldrich, St. Louis, MO, USA). Briefly, 5×10^3 cells per well were seeded on a 96-well plate in 100 µL of complete medium. On the next day, QDs at concentrations ranging from 0.5 to 64 nM were added in serial dilutions using a 2-fold dilution factor either in complete or serum-free medium. The cells in complete medium were incubated with QDs for 24 and 48 h. The cells in serum-free medium were incubated with QDs for 6 h followed by replenishment with fresh complete medium. The cells were subsequently incubated for 24 and 48 h. After incubation, 10 µL of CCK8 reagent was added to each well, and the cells were incubated for 2 h at 37 °C in 5% CO_2 and 90% humidity. The background signal controls containing QDs at all tested concentrations in the cell culture medium were introduced. The optical density was measured using a BioTek ELx808 spectrophotometer (BioTek Instruments, Winooski, VT, USA) at a wavelength of 450 nm.

Quantum dot release assay

To analyse the release of the QDs from the MSCs in the 3D culture, the cells were labelled with 8 nM QDs in serum-free medi-

um or 16 nM QDs in complete medium for 6 h on TCPS plates. The cells were then trypsinised and seeded in polyHEMA-coated plates in complete medium. MSC spheroids were harvested at 24, 48 and 72 h and trypsinised for 5 min at 37 °C to obtain a single cell suspension. The QD signal was analysed by flow cytometry as described in the section "Establishment of 3D cell culture model".

3D co-culture model for quantum dot transfer analysis

Prior to 3D co-culture seeding, 1×10^5 MSCs were labelled with 8 nM QDs for 6 h in serum-free medium. The cells were then trypsinised, and 5×10^4 MSCs were seeded in polyHEMA-coated plates for co-culture with 2.5×10^4 MCF7 or MDA-MB-231 cells (2:1) in complete medium [52,53]. After 24 h, supernatants containing floating spheroids were aspirated and centrifuged at 250 g for 5 min. The pellet was suspended in 0.25% trypsin–EDTA for 5 min at 37 °C to ensure the dissociation of the spheroids into a single cell suspension. The cells were washed, stained with CD90 FITC or EpCAM FITC and analysed by flow cytometry.

For fluorescence imaging of QD transfer, the cancer cell and MSC mono- or co-culture spheroids were harvested after 24 h of propagation on the polyHEMA coating, trypsinised to obtain single cell suspension and then allowed to adhere to microscopy chamber slides overnight in complete medium. Next, the cells were stained with human CD90 FITC (clone DG3, Miltenyi Biotec, Bergisch Gladbach, Germany) diluted 1:11 in complete medium for 1 h at room temperature. The samples were then counterstained with Hoechst 33342 trihydrochloride (10 mg/mL) solution (Thermo Fisher Scientific, USA), fixed with 4% PFA and mounted with ProLong gold anti-fade mounting medium.

Fluorescence imaging

For the z-scan measurements, MSC spheroids were stained with 5 μM 3,3'-dioctadecyloxacarbocyanine perchlorate (DiO) in complete medium for 45 min at 37 °C and counterstained with Hoechst dye. The cells were then trypsinised and seeded in 3D culture for 24 h. The spheroids were then transferred to 4-well chamber slides. All reagents were obtained from Thermo Fisher Scientific, Waltham, Massachusetts, USA.

Fluorescence imaging was performed as described previously [54]. A Nikon eclipse Ti microscope equipped with a Nikon C2 confocal system was used. A Nikon S Plan Fluor ELWD 40×/0.60 objective was used. A 488 nm laser was used to excite CD90 FITC and DiO. In addition, a 405 nm laser was used to excite Hoechst and QD655. To detect the fluorescence, the following filters were used: 447/60 nm with Hoechst 525/50 nm for CD90 FITC and DiO, and a 561 long pass filter for QD655 (all from Nikon, Tokyo, Japan). Each channel was recorded separately to avoid spectral overlap. The images were analysed using Nis-Elements C 4.13 software (Nikon, Tokyo, Japan). Quantification of the QD fluorescence signal was performed using Nis-Elements C 4.13 software.

Cell viability in 3D culture

Cell viability in the 3D culture was analysed by propidium iodide (PI, Sigma-Aldrich, St. Louis, MO, USA). MSCs, MCF7 and MDA-MB-231 mono- or co-culture spheroids were harvested from 3D culture after 24 and 48 h, trypsinised and stained with FITC mouse anti-human CD90 (clone 5E10). The samples were then treated with 10 μg/mL PI at a 1:40 dilution in PBS for 5 min at room temperature and analysed by flow cytometry.

Statistical analysis

Statistical analysis was performed using GraphPad Prism Software (GraphPad Inc., California, USA). Data were expressed as the mean ± standard error of mean. The differences between the studied groups ($n = 3$) were statistically assessed by one-way ANOVA followed by Tukey's post hoc test. The significance was represented as follows: *p-value < 0.05, **p-value < 0.01, ***p-value < 0.001.

Supporting Information

Supporting Information File 1

Additional experimental information.
Endocytosis inhibitor assay; QD endocytic pathway analysis in MSCs, MCF7 and MDA-MB-231 cells; Confocal microscopy z-sections of MSC and breast cancer cell co-culture spheroids; EpCAM expression in MSCs and breast cancer cells MCF7 and MDA-MB-231; QD transfer from nanoengineered MSCs to MCF7 cells using EpCAM as a selective marker for MCF7 cells.
[https://www.beilstein-journals.org/bjnano/content/supplementary/2190-4286-9-32-S1.pdf]

Acknowledgements

This work was supported by Taiwan-Lithuania-Latvia mutual research collaboration fund grant (LV-LT-TW-/2016/6) and Latvia Science Council grant (No. 625/2014).

References

1. Jackson, H.; Muhammad, O.; Daneshvar, H.; Nelms, J.; Popescu, A.; Vogelbaum, M. A.; Bruchez, M.; Toms, S. A. *Neurosurgery* **2007,** *60,* 524–530.
2. Sadhukha, T.; O'Brien, T. D.; Prabha, S. *J. Controlled Release* **2014,** 243. doi:10.1016/j.jconrel.2014.10.015

3. Ramdasi, S.; Sarang, S.; Viswanathan, C. *Int. J. Hematol. Oncol. Stem Cell Res.* **2015,** *9,* 2.
4. Gao, Z.; Zhang, L.; Hu, J.; Sun, Y. *Nanomedicine* **2013,** *9,* 2. doi:10.1016/j.nano.2012.06.003
5. Shah, K. *Adv. Drug Delivery Rev.* **2012,** *64,* 739. doi:10.1016/j.addr.2011.06.010
6. Dominici, M.; Le Blanc, K.; Mueller, I.; Slaper-Cortenbach, I.; Marini, F.; Krause, D.; Deans, R.; Keating, A.; Prockop, D.; Horwitz, E. *Cytotherapy* **2006,** *8,* 315. doi:10.1080/14653240600855905
7. Li, Z.; Fan, D.; Xiong, D. *Stem Cell Invest.* **2015,** *2,* 6. doi:10.3978/j.issn.2306-9759.2015.03.01
8. Sage, E. K.; Thakrar, R. M.; Janes, S. M. *Cytotherapy* **2016,** *18,* 1435. doi:10.1016/j.jcyt.2016.09.003
9. Li, L.; Guan, Y.; Liu, H.; Hao, N.; Liu, T.; Meng, X.; Fu, C.; Li, Y.; Qu, Q.; Zhang, Y.; Ji, S.; Chen, L.; Chen, D.; Tang, F. *ACS Nano* **2011,** *5,* 7462. doi:10.1021/nn202399w
10. Studeny, M.; Marini, F. C.; Champlin, R. E.; Zompetta, C.; Fidler, I. J.; Andreeff, M. *Cancer Res.* **2002,** *62,* 3603–3608.
11. Kidd, S.; Spaeth, E.; Dembinski, J. L.; Dietrich, M.; Watson, K.; Klopp, A.; Battula, V. L.; Weil, M.; Andreeff, M.; Marini, F. C. *Stem Cells* **2009,** *27,* 2614. doi:10.1002/stem.187
12. Lourenco, S.; Teixeira, V. H.; Kalber, T.; Jose, R. J.; Floto, R. A.; Janes, S. M. *J. Immunol.* **2015,** *194,* 3463. doi:10.4049/jimmunol.1402097
13. Dapkute, D.; Steponkiene, S.; Bulotiene, D.; Saulite, L.; Riekstina, U.; Rotomskis, R. *Int. J. Nanomed.* **2017,** *12,* 8129. doi:10.2147/IJN.S143367
14. Edmondson, R.; Broglie, J. J.; Adcock, A. F.; Yang, L. J. *Assay Drug Dev. Technol.* **2014,** *12,* 207. doi:10.1089/adt.2014.573
15. Fennema, E.; Rivron, N.; Rouwkema, J.; van Blitterswijk, C.; de Boer, J. *Trends Biotechnol.* **2013,** *31,* 108. doi:10.1016/j.tibtech.2012.12.003
16. Katt, M. E.; Placone, A. L.; Wong, A. D.; Xu, Z. S.; Searson, P. C. *Front. Bioeng. Biotechnol.* **2016,** 12. doi:10.3389/fbioe.2016.00012
17. Yamada, K. M.; Cukierman, E. *Cell* **2007,** *130,* 601. doi:10.1016/j.cell.2007.08.006
18. Zanoni, M.; Piccinini, F.; Arienti, C.; Zamagni, A.; Santi, S.; Polico, R.; Bevilacqua, A.; Tesei, A. *Sci. Rep.* **2016,** *6,* 19103. doi:10.1038/srep19103
19. Ivascu, A.; Kubbies, M. *J. Biomol. Screening* **2006,** *11,* 922. doi:10.1177/1087057106292763
20. Kelm, J. M.; Timmins, N. E.; Brown, C. J.; Fussenegger, M.; Nielsen, L. K. *Biotechnol. Bioeng.* **2003,** *83,* 173. doi:10.1002/bit.10655
21. Mehta, G.; Hsiao, A. Y.; Ingram, M.; Luker, G. D.; Takayama, S. *J. Controlled Release* **2012,** *164,* 192. doi:10.1016/j.jconrel.2012.04.045
22. Pericleous, P.; Gazouli, M.; Lyberopoulou, A.; Rizos, S.; Nikiteas, N.; Efstathopoulos, E. P. *Int. J. Cancer* **2012,** *131,* 519. doi:10.1002/ijc.27528
23. Lobba, A. R. M.; Forni, M. F.; Carreira, A. C. O.; Sogayar, M. C. *Cytometry, Part A* **2012,** *81,* 1084. doi:10.1002/cyto.a.22220
24. Riekstina, U.; Cakstina, I.; Parfejevs, V.; Hoogduijn, M.; Jankovskis, G.; Muiznieks, I.; Muceniece, R.; Ancans, J. *Stem Cell Rev. Rep.* **2009,** *5,* 378. doi:10.1007/s12015-009-9094-9
25. Pietilä, M.; Lehenkari, P.; Kuvaja, P.; Kaakinen, M.; Kaul, S. C.; Wadhwa, R.; Uemura, T. *Exp. Cell Res.* **2013,** *319,* 2770. doi:10.1016/j.yexcr.2013.07.023
26. Melzer, C.; Yang, Y.; Hass, R. *Cell Commun. Signaling* **2016,** *14,* 20. doi:10.1186/s12964-016-0143-0
27. Caicedo, A.; Fritz, V.; Brondello, J.-M.; Ayala, M.; Dennemont, I.; Abdellaoui, N.; de Fraipont, F.; Moisan, A.; Prouteau, C. A.; Boukhaddaoui, H.; Jorgensen, C.; Vignais, M.-L. *Sci. Rep.* **2015,** *5,* 9073. doi:10.1038/srep09073
28. Yang, Y.; Otte, A.; Hass, R. *Stem Cells Dev.* **2015,** *24,* 1205. doi:10.1089/scd.2014.0413
29. He, K.; Luo, W.; Zhang, Y.; Liu, F.; Liu, D.; Xu, L.; Qin, L.; Xiong, C.; Lu, Z.; Fang, X.; Zhang, Y. *ACS Nano* **2010,** *4,* 3015. doi:10.1021/nn1002198
30. Pi, Q. M.; Zhang, W. J.; Zhou, G. D.; Liu, W.; Cao, Y. *BMC Biotechnol.* **2010,** 36. doi:10.1186/1472-6750-10-36
31. Oh, N.; Park, J. H. *Int. J. Nanomed.* **2014,** *9* (Suppl. 1), 51. doi:10.2147/IJN.S26592
32. Peng, L.; He, M.; Chen, B.; Wu, Q.; Zhang, Z.; Pang, D.; Zhu, Y.; Hu, B. *Biomaterials* **2013,** *34,* 9545. doi:10.1016/j.biomaterials.2013.08.038
33. Zeng, X. H.; Morgenstern, R.; Nyström, A. M. *Biomaterials* **2014,** *35,* 1227. doi:10.1016/j.biomaterials.2013.10.042
34. Zubris, K. A. V.; Liu, R.; Colby, A.; Schulz, M. D.; Colson, Y. L.; Grinstaff, M. W. *Biomacromolecules* **2013,** *14,* 2074. doi:10.1021/bm400434h
35. Liu, Q.; Li, H.; Xia, Q.; Liu, Y.; Xiao, K. *Int. J. Nanomed.* **2015,** *10,* 7073. doi:10.2147/IJN.S94543
36. Cesarz, Z.; Tamama, K. *Stem Cells Int.* **2016,** *2016,* 9176357. doi:10.1155/2016/9176357
37. Chen, Y.-C.; Lou, X.; Zhang, Z.; Ingram, P.; Yoon, E. *Sci. Rep.* **2015,** *5,* 12175. doi:10.1038/srep12175
38. Shimony, N.; Avrahami, I.; Gorodetsky, R.; Elkin, G.; Tzukert, K.; Zangi, L.; Levdansky, L.; Krasny, L.; Haviv, Y. S. *Nephrol., Dial., Transplant.* **2008,** *23,* 2071. doi:10.1093/ndt/gfn062
39. Wiesmann, A.; Bühring, H.-J.; Mentrup, C.; Wiesmann, H.-P. *Head Face Med.* **2006,** *2,* 8. doi:10.1186/1746-160X-2-8
40. Lee, H. J.; Choi, B. H.; Min, B.-H.; Park, S. R. *Arthritis Rheum.* **2009,** *60,* 2325. doi:10.1002/art.24786
41. Frith, J. E.; Thomson, B.; Genever, P. G. *Tissue Eng., Part C* **2010,** *16,* 735. doi:10.1089/ten.TEC.2009.0432
42. Mandel, K.; Yang, Y.; Schambach, A.; Glage, S.; Otte, A.; Hass, R. *Stem Cells Dev.* **2013,** *22,* 3114. doi:10.1089/scd.2013.0249
43. Santos, J. M.; Camões, S. P.; Filipe, E.; Cipriano, M.; Barcia, R. N.; Filipe, M.; Teixeira, M.; Simões, S.; Gaspar, M.; Mosqueira, D.; Nascimento, D. S.; Pinto-do-Ó, P.; Cruz, P.; Cruz, H.; Castro, M.; Miranda, J. P. *Stem Cell Res. Ther.* **2015,** *9,* 90. doi:10.1186/s13287-015-0082-5
44. Malin, D.; Strekalova, E.; Petrovic, V.; Rajanala, H.; Sharma, B.; Ugolkov, A.; Gradishar, W. J.; Cryns, V. L. *Oncogene* **2015,** *34,* 5626. doi:10.1038/onc.2015.12
45. Akekawatchai, C.; Roytrakul, S.; Kittisenachai, S.; Isarankura-Na-Ayudhya, P.; Jitrapakdee, S. *Asian Pac. J. Cancer Prev.* **2016,** *17,* 581. doi:10.7314/APJCP.2016.17.2.581
46. Murugan, C.; Rayappan, K.; Thangam, R.; Bhanumathi, R.; Shanthi, K.; Vivek, R.; Thirumurugan, R.; Bhattacharyya, A.; Sivasubramanian, S.; Gunasekaran, P.; Kannan, S. *Sci. Rep.* **2016,** *6,* No. 34053. doi:10.1038/srep34053
47. Eggenhofer, E.; Benseler, V.; Kroemer, A.; Popp, F. C.; Geissler, E. K.; Schlitt, H. J.; Baan, C. C.; Dahlke, M. H.; Hoogduijn, M. J. *Front. Immunol.* **2012,** *3,* 297. doi:10.3389/fimmu.2012.00297

48. Kraitchman, D. L.; Tatsumi, M.; Gilson, W. D.; Ishimori, T.; Kedziorek, D.; Walczak, P.; Segars, W. P.; Chen, H. H.; Fritzges, D.; Izbudak, I.; Young, R. G.; Marcelino, M.; Pittenger, M. F.; Solaiyappan, M.; Boston, R. C.; Tsui, B. M. J.; Wahl, R. L.; Bulte, J. W. M. *Circulation* **2005,** *112,* 1451. doi:10.1161/CIRCULATIONAHA.105.537480
49. Steponkiene, S.; Valanciunaite, J.; Skripka, A.; Rotomskis, R. *J. Biomed. Nanotechnol.* **2014,** *10,* 679. doi:10.1166/jbn.2014.1738
50. Kuroda, Y.; Wakao, S.; Kitada, M.; Murakami, T.; Nojima, M.; Dezawa, M. *Nat. Protoc.* **2013,** *8,* 1391. doi:10.1038/nprot.2013.076
51. Xu, G.; Lin, G.; Lin, S.; Wu, N.; Deng, Y.; Feng, G.; Chen, Q.; Qu, J.; Chen, D.; Chen, S.; Niu, H.; Mei, S.; Yong, K.-T.; Wang, X. *Sci. Rep.* **2016,** *6,* 37677. doi:10.1038/srep37677
52. Maestroni, G. J. M.; Hertens, E.; Galli, P. *Cell. Mol. Life Sci.* **1999,** *55,* 663. doi:10.1007/s000180050322
53. Long, X.; Matsumoto, R.; Yang, P.; Uemura, T. *Cell Struct. Funct.* **2013,** *38,* 109–121. doi:10.1247/csf.12029
54. Saulite, L.; Dapkute, D.; Pleiko, K.; Popena, I.; Steponkiene, S.; Rotomskis, R.; Riekstina, U. *Beilstein J. Nanotechnol.* **2017,** *8,* 1218–1230. doi:10.3762/bjnano.8.123

4 publikacija / 4th publication

3D cellular spheroids as tools for understanding carboxylated quantum dot behavior in tumors

Jarockyte G, **Dapkute D**, Karabanovas V, Daugmaudis JV, Ivanauskas F, Rotomskis R.

Biochimica et biophysica acta. General subjects **1862**:914-923 (2018)

DOI: 10.1016/j.bbagen.2017.12.014

5 publikacija / 5th publication

Impact of Quantum Dot Surface on Complex Formation with Chlorin e6 and Photodynamic Therapy

Skripka A, **Dapkute D**, Valanciunaite J, Karabanovas V, Rotomskis R.

Nanomaterials **9**(1):9 (2019)

DOI: 10.3390/nano9010009

nanomaterials

MDPI

Article

Impact of Quantum Dot Surface on Complex Formation with Chlorin e_6 and Photodynamic Therapy

Artiom Skripka [1], Dominyka Dapkute [1,2], Jurga Valanciunaite [1], Vitalijus Karabanovas [1,3] and Ricardas Rotomskis [1,4,*]

1 Biomedical Physics Laboratory, National Cancer Institute, P. Baublio st 3b, LT-08406, Vilnius, Lithuania; artiom.skripka@emt.inrs.ca (A.S.); dominyka.dapkute@nvi.lt (D.D.); Jurgaval7@gmail.com (J.V.); Vitalijus.Karabanovas@nvi.lt (V.K.)
2 Life Science Center, Vilnius University, Sauletekio ave. 7, LT-10223 Vilnius, Lithuania
3 Department of Chemistry and Bioengineering, Vilnius Gediminas Technical University, Sauletekio ave. 11, LT-10221, Vilnius, Lithuania
4 Biophotonics Group of Laser Research Center, Faculty of Physics, Vilnius University, Sauletekio ave. 9, LT-10222, Vilnius, Lithuania
* Correspondence: ricardas.rotomskis@nvi.lt; Tel.: +370-5-219-0908

Received: 29 November 2018; Accepted: 18 December 2018; Published: 22 December 2018

Abstract: Nanomaterials have permeated various fields of scientific research, including that of biomedicine, as alternatives for disease diagnosis and therapy. Among different structures, quantum dots (QDs) have distinctive physico-chemical properties sought after in cancer research and eradication. Within the context of cancer therapy, QDs serve the role of transporters and energy donors to photodynamic therapy (PDT) drugs, extending the applicability and efficiency of classic PDT. In contrast to conventional PDT agents, QDs' surface can be designed to promote cellular targeting and internalization, while their spectral properties enable better light harvesting and deep-tissue use. Here, we investigate the possibility of complex formation between different amphiphilic coating bearing QDs and photosensitizer chlorin e_6 (Ce_6). We show that complex formation dynamics are dependent on the type of coating—phospholipids or amphiphilic polymers—as well as on the surface charge of QDs. Förster's resonant energy transfer occurred in every complex studied, confirming the possibility of indirect Ce_6 excitation. Nonetheless, *in vitro* PDT activity was restricted only to negative charge bearing QD-Ce_6 complexes, correlating with better accumulation in cancer cells. Overall, these findings help to better design such and similar complexes, as gained insights can be straightforwardly translated to other types of nanostructures—expanding the palette of possible therapeutic agents for cancer therapy.

Keywords: photodynamic therapy; quantum dots; chlorin e_6; energy transfer

1. Introduction

Semiconductor quantum dots (QDs) have unique size-dependent optical properties and are used in biological and medical research [1], including the advancement of photodynamic therapy (PDT) of cancer [2]. PDT is a treatment method that combines light and light sensitive drugs—photosensitizers (PS)—to produce reactive oxygen species, which are deleterious to biological objects. Being non-invasive and highly selective, PDT is considered as an effective method to battle various types of malignancies with minimal damage to healthy tissues. The idea of using QDs for PDT is based on their ability to serve as Förster resonance energy transfer (FRET) donors to classical PS [2]. As energy donors, QDs possess all the necessary properties, such as broad absorption spectrum,

tunable photoluminescence (PL) band position, high PL quantum yield (QY), long lifetime, and, most importantly, a far superior extinction coefficient as compared to classical PDT agents [3]. Combining these properties in a single donor, QD potentiates PS excitation and subsequently enhances the singlet oxygen generation efficiency [4–8]. Moreover, excitation of PS is restricted to use of visible light (typically in the red spectral side), hence to superficial applicability of PDT in tissues. Switching to near-infrared excitation, which coincides with optical transparency of tissues as in the case of two-photon excitation, enables PDT at greater tissue depths. In this regard, QDs could be used for two-photon PDT [9–11], as they have a large two-photon absorption cross section and remain photostable even at high laser excitation powers [12,13], in turn overcoming the two-photon excitation limits imposed on a variety of common PS.

Different QD–PS systems reported to date were designed by either covalent or non-covalent binding of PS [4,7,14,15]. In the latter case, the stability and subsequently FRET efficiency of the system highly depend on the interaction nature between QDs and PS.

We have previously shown that the second-generation PS, chlorin e_6 (Ce_6), and QDs bearing phospholipid coating self-assemble into a stable complex with high FRET efficiency [16,17]. The major driving force of QD-Ce_6 complex formation is the hydrophobic interaction between the non-polar moieties of amphiphilic Ce_6 and phospholipids. Such a non-covalent QD-Ce_6 complex retained high FRET efficiency in living cells and produced a significant phototoxic effect [18]. Additionally, we showed that the type of phospholipids in QD coating plays a crucial role in the formation and long-term stability of QD-Ce_6 complex [19].

The importance of such and similar complexes lies in the simplicity of its formation and nature of the interaction, which results in exceptionally efficient energy transfer between the QDs and the bound PS. Moreover, it is valuable to understand if the self-assembly of such nanoparticle (NP)-PS complexes [20,21] could be directly translated in terms of varying the amphiphilic coating of NPs, how it would influence the indirect excitation of the PS, colloidal stability, accumulation in cells, and eventually the PDT effect.

In this work, we explore the QD-Ce_6 complex by using QDs with two types of amphiphilic coating, namely lipids and polymers with differently charged terminal groups, to compare formation, stability, and FRET efficiency of QD-Ce_6 complex in each case. To the best of our knowledge this is the first report that investigates QD-Ce_6 complex formation with amphiphilic polymer coated QDs. Furthermore, we show the surface coating dependent accumulation of these complexes within breast cancer cells and its influence on PDT efficiency; this enables the current paper to go beyond photophysical studies and by direct comparison select an optimal QD-Ce_6 formulation for the future of PDT.

2. Materials and Methods

2.1. Materials

CdSe/ZnS QDs encapsulated with polyethylene glycol (PEG) grafted phospholipids (*L*-QDs), bearing amine or carboxyl functional groups, were purchased from eBioscience Inc. (Waltham, MA, USA). Amphiphilic polymer coated CdSe/ZnS QDs (*P*-QDs) with either PEG-amine or carboxyl group were purchased from Invitrogen Corp. (Carlsbad, CA, USA). All QDs had a photoluminescence (PL) band at around 605 nm. Chlorin e_6 (Ce_6) tetrasulfonic acid was obtained from Frontier Scientific Inc. (Logan, UT, USA). All materials were used without further purification. Stock solution of Ce_6 was prepared by dissolving the powder in a small amount of 0.2 M NaOH solution and further diluting with phosphate buffer (PB) (pH 7). Working concentration of *L*- and *P*-QDs PB sols was 0.05 μM. QD:Ce_6 molar concentration ratio was varied from 1:0.05 to 1:10, adding a small amount (5 μL) of Ce_6 solution into 2000 μL of working QDs sol.

2.2. Spectral Studies

Steady-state absorption spectra were recorded with a Cary 50 UV-VIS spectrophotometer (Varian Inc., Palo Alto, CA, USA). PL measurements were carried out with a Cary Eclipse spectrophotometer (Varian Inc., Palo Alto, CA, USA). Fluorescence decay measurements were performed with a F920 spectrophotometer (Edinburgh Instruments, Livingston, UK), equipped with a single photon photomultiplier detector (S900-R) (Hamamatsu, Shizuoka, Japan) and a picosecond pulsed diode laser (EPL-405) (excitation wavelength 405 nm, pulse width 66.9 ps, repetition rate 2 MHz) (Edinburgh Instruments, Livingston, UK). Quartz cuvettes with the optical path length of 1 cm were used for all measurements.

2.3. Cell Culturing and Labeling

For intracellular localization of QDs, QD-Ce_6 complexes and Ce_6, MDA-MB-231 breast cancer cells (ATCC, USA) were seeded on a Nunc LabTek II chamber slide (Thermo Fisher Scientific, Waltham, MA, USA) at a density of 25,000 cells per well using standard cell culture medium (Dulbecco's modified Eagle's medium (DMEM), 10% fetal bovine serum (FBS), 1% penicillin/streptomycin antibiotic mix (all from Gibco, Waltham, MA, USA). Upon cell attachment, cells were treated with serum-free cell medium containing 10 nM of either different *P*-QDs or *L*-QDs or their QD-Ce_6 complexes for 24 hours. In addition, 1 μM Ce_6 solution was used as a control. Samples for confocal microscopy were prepared as previously described [22]. Briefly, cells were fixed with 4% paraformaldehyde solution (Sigma Aldrich, USA) and permeabilized with 0.2% Triton-X 100 (Sigma Aldrich, St. Louis, MO, USA). Actin filaments were stained with 15 U/mL Alexa Fluor 488 Phalloidin (Thermo Fisher Scientific, Waltham, MA, USA) and 25 μg/mL Hoechst 33342 (Sigma Aldrich, St. Louis, MO, USA) was used to label nuclei.

2.4. PDT Studies

To test the PDT effect, 10X concentrated QD-Ce_6 complexes maintaining QD:Ce_6 molar concentration ratio at 1:10 were prepared in a small amount of phosphate buffered saline (PBS) (pH 7.4) and kept at room temperature for 3 hours for complexes to equilibrate. Different QD-Ce_6 sols in PBS were then diluted 10 times in a serum-free cell growth medium and poured over the cells grown on Nunc Lab-Tek chambered coverglass (Thermo Fisher Scientific, USA) at a density of 25,000 cells per well. After 24 hours the cells were irradiated with 470 nm light (MAX-302 xenon light source (Asahi Spectra, Japan)) providing a 17.7 J/cm^2 irradiation dose in each well. After irradiation, cells were returned to the incubator. Twenty-four hours post treatment, 2 μM calcein AM and 4 μM ethidium homodimer-1 (LIVE/DEAD viability/cytotoxicity test kit by Thermo Fisher Scientific, Waltham, MA, USA) were added to each well and kept for 20 min before confocal microscopy analysis. Statistical analysis of PDT-affected cells was performed by direct counting of green (alive) and red (dead) cells in at least 5 different fields. Statistical significance was assessed using unpaired two-tailed Student's *t* test.

2.5. Cellular Microscopy

Cell samples were imaged with a laser scanning confocal microscope (Nikon Eclipse TE2000-S, C1 Plus; Nikon, Japan) using either oil-immersion 60× NA 1.4 objective (Plan Apo VC; Nikon, Japan) for intracellular localization studies or dry 20× NA 0.5 objective (Plan Fluor; Nikon, Japan) for visualizing live/dead cells after the PDT. Diode laser (404 nm) excitation was used for Hoechst 33342, argon ion laser (488 nm) for Alexa Fluor 488 Phalloidin, calcein AM, and ethidium homodimer-1, and helium-neon laser (543 nm) for QDs. Images were captured with the EZ-C1 v3.90 image analysis software (Nikon, Japan) and processed using EZ-C1 Bronze v3.80 (Nikon, Japan) and ImageJ 1.48 (National Institute of Health, Bethesda, MD, USA) software.

3. Results and Discussion

3.1. QD-Ce$_6$ Complex Formation

In order to determine the effect of the QD coating on the complex formation with photosensitizer Ce$_6$, we examined four different types of QDs. Namely, QDs with phospholipid (*L*-QDs) or amphiphilic polymer (*P*-QDs) coatings, bearing either amine or carboxyl terminal groups. It should be noted that all QDs except *P*-QD(carboxyl) were also grafted with PEG.

The absorbance of QDs covered the major part of the visible spectrum starting from UV and terminating with the first excitonic band at 594 or 600 nm for *L*-QDs and *P*-QDs, respectively (Figure 1A). The PL band was centered at 605 nm for every QD studied. The PL band's full width at half maximum was around 26 and 21 nm for *L*-QDs and *P*-QDs, respectively (Figure 1A). Absorption and PL properties of *L*-QDs or *P*-QDs were independent of the surface charge (Figure S1). Absorption spectrum of Ce$_6$ solution showed the Soret band at around 404 nm and several less pronounced Q-bands, with the most intense Q(I) at 654 nm (Figure 1B). Emission of Ce$_6$ in PB was centered at 660 nm.

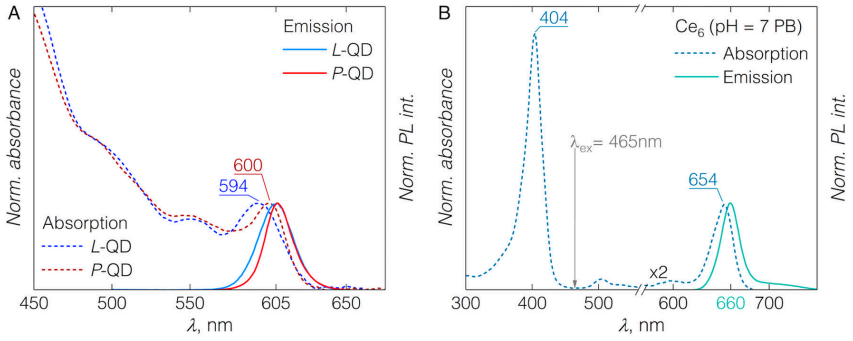

Figure 1. (**A**) Normalized absorption and emission spectra of quantum dots (QDs) functionalized with either phospholipids (*L*-QD) or amphiphilic polymer (*P*-QD) and bearing amine surface charge. (**B**) Normalized absorption and emission spectra of pure chlorin e$_6$ (Ce$_6$) in phosphate buffer (PB) (pH 7); note, the absorption region of Q(I) band is magnified for clarity; labels indicate absorption maxima position in nanometers. Emission spectra were measured with 400 nm excitation light. Arrow indicates excitation wavelength of 465 nm, used for Förster resonance energy transfer (FRET) studies.

As shown previously [16,17], mixed together, QDs and Ce$_6$ form a complex, resulting in spectral changes of both constituents. Most significantly, the fluorescence band of Ce$_6$ shifts towards the red spectral side from 660 to 672 nm (Figure 2). Such a bathochromic shift is typically observed for Ce$_6$ in non-polar milieu [23–25]. QDs' coating—phospholipids or amphiphilic polymers—provide such non-polar microenvironment for bound Ce$_6$ molecules. Furthermore, in the QD-Ce$_6$ complex, the close proximity of Ce$_6$ to the QD's surface permits an efficient FRET [16]. The FRET from QDs to Ce$_6$ in QD-Ce$_6$ complex was confirmed by the fluorescence spectroscopy and fluorescence decay studies. When QD-Ce$_6$ complex was excited at the wavelength (465 nm) solely absorbed by QDs (see Figure S2 for fluorescence excitation spectrum of Ce$_6$), the emission bands of both, the QDs at 605 nm and the Ce$_6$ at 672 nm, were observed—indicating FRET.

In both cases of *L*-QDs, irrespective of the surface charge, the formation of QD-Ce$_6$ proceeded almost instantaneously after the addition of Ce$_6$ (1 nM) to the QD sol (0.02 μM)—resulting in a quenching of QD PL band and appearance of Ce$_6$ fluorescence at 672 nm (Figure 2A,B). Upon increasing the Ce$_6$ concentration in the sol up to a QD:Ce$_6$ molar concentration ratio of 1:10, the intensity of QD PL kept decreasing, and that of Ce$_6$ reached a maximum at QD:Ce$_6$ of 1:5 (Figure 2A,B; Figure 3A). Further increasing the amount of Ce$_6$ in the sol resulted in the decrease of Ce$_6$ fluorescence, probably

due to the concentration quenching effect. Importantly, although carboxyl groups of Ce_6 molecules are negatively charged, the QD-Ce_6 complex formation happened in a similar fashion for both the positively charged *L*-QD(amine) and negatively charged *L*-QD(carboxyl). Hence, indicating that the hydrophobic interaction between the Ce_6 and non-polar part of QD coating can overcome the potential barrier of the electrostatic repulsion.

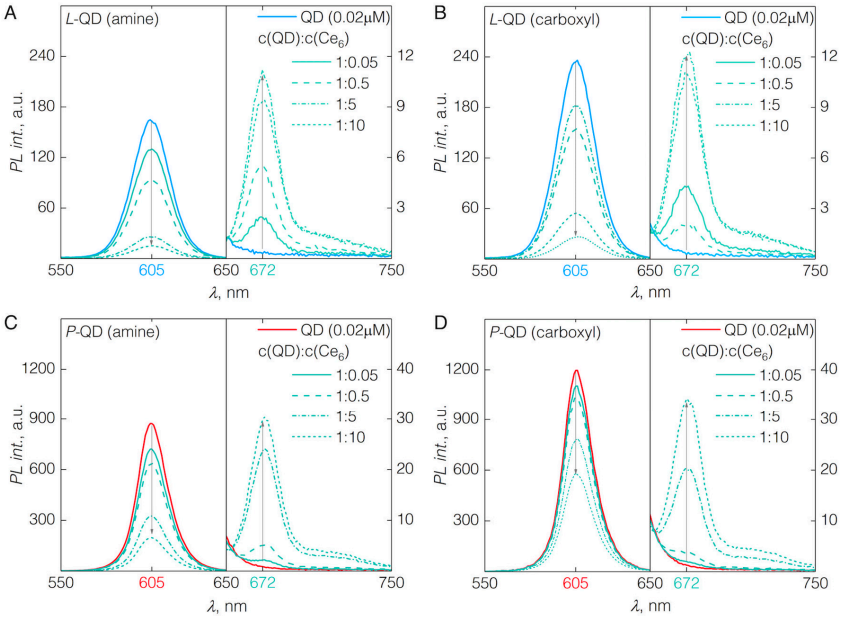

Figure 2. Emission spectra of pure QDs and respective QD-Ce_6 complexes varying the molar concentration ratio between QDs and Ce_6 from 1:0.05 to 1:10. Spectra were recorded under 465 nm excitation. (**A**) *L*-QD(amine)-Ce_6; (**B**) *L*-QD(carboxyl)-Ce_6; (**C**) *P*-QD(amine)-Ce_6; (**D**) *P*-QD(carboxyl)-Ce_6.

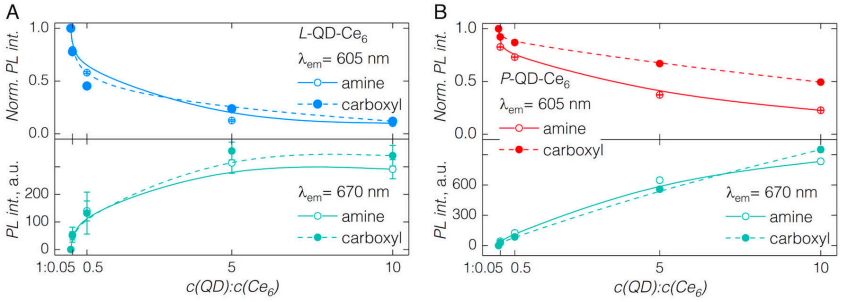

Figure 3. Normalized emission intensity of pure QDs and in the presence of increasing amount of Ce_6 together with absolute fluorescence intensity of Ce_6 after the binding to QDs. (**A**) *L*-QD-Ce_6; (**B**) *P*-QD-Ce_6. Line plots are introduced to guide the eye.

Similarly, as in the case of *L*-QDs, the complex formation between Ce_6 and QDs with the amphiphilic polymer coating (*P*-QDs) was observed by the bathochromic shift of the Ce_6 emission band to 672 nm and simultaneous quenching of the QD emission at 605 nm (Figure 2C,D). However,

several differences in the *P*-QD-Ce_6 complex formation were observed. In contrast to *L*-QD-Ce_6, the quenching of QD PL (and subsequent increase of Ce_6 PL) was considerably less pronounced when increasing the molar concentration of Ce_6 in the sol, and the saturation effect of QD-Ce_6 complex formation was not observed even at QD:Ce_6 of 1:10. Differences of *P*-QD-Ce_6 complex formation might stem from the possible crosslinking of the polymer coating [26,27], which would sterically hinder the intercalation of Ce_6 within. Particularly in the case of *P*-QD(carboxyl), the interaction between the Ce_6 and QDs was further impeded by the electrostatic repulsion, as the PL of carboxyl bearing QDs was significantly less quenched than that of their amine counterparts. Additionally, absence of PEG might have caused the slower complex formation dynamics with *P*-QD(carboxyl), however the exact influence of PEG in QD-Ce_6 complex formation remains unknown and requires further investigation.

It is worth noting that for the same crosslinking reasons, the amphiphilic polymer coating usually ensures better colloidal stability of NPs [26]. Thus, determined by the surface coating of QDs, a tradeoff exists between the dynamics of QD-Ce_6 complex formation and its subsequent colloidal stability. We have additionally checked for the PL intensity changes during the first 16 min after the addition of the highest amount of Ce_6 (QD:Ce_6 = 1:10), which suggested that the QD-Ce_6 complex is not obstructed from being formed in the case of *P*-QDs, rather it requires longer equilibration time (Figure S2, Figure 3). Notably, within the same time interval, PL intensity of *L*-QDs in QD-Ce_6 complex decreased, alluding to a decreased colloidal stability of lipid coated QDs (Figure S2).

3.2. FRET from QDs to Ce_6

After establishing the QD-Ce_6 complex formation dynamics for differently coated QDs, we proceeded with estimation of FRET parameters for each QD:Ce_6 molar ratio studied, at a time point when Ce_6 is added to the sols. FRET efficiency was estimated from the QDs' PL decay (Equation 1), accounting only for the dynamic quenching—non-radiative energy transfer.

$$E = 1 - \frac{\langle \tau_{DA} \rangle}{< \tau_D >} \quad (1)$$

Here, $<\tau_D>$ and $<\tau_{DA}>$ denote average photoluminescence decay time of donor (QDs) alone and in the presence of acceptor (Ce_6), respectively. The average PL decay time for *L*-QDs decreased from 17.2 to 3 ns and 17.8 to 2.9 ns in the case *L*-QD(amine) and *L*-QD(carboxyl), respectively, at the highest concentration of Ce_6 (Figure 4A,B). FRET efficiencies were around 82.8 and 83.7% for *L*-QD(amine)-Ce_6 and *L*-QD(carboxyl)-Ce_6, respectively (Table 1). High FRET values support the notion of Ce_6 present in the phospholipid coating—in close proximity to the surface of QDs. In the case of *P*-QDs, addition of Ce_6 to the *P*-QD(amine) sol, reduced the PL decay time from 14.6 to 4.8 ns, yielding 66.9% FRET efficiency, while for *P*-QD(carboxyl) it changed from 13.2 to 7.9 ns, hence 40.1% FRET efficiency (Figure 4C,D). Overall, FRET efficiencies obtained by exploiting hydrophobic interaction between Ce_6 and amphiphilic coatings of QDs are highest reported thus far, when compared to other QD-Ce_6 systems comprised of electrostatically or covalently interacting moieties [7,28].

Table 1. FRET parameters for different types of QD:Ce_6 complexes at various Ce_6 amounts (*m*).

Quantity	***L*-QD(amine)**		***L*-QD(carboxyl)**		***P*-QD(amine)**		***P*-QD(carboxyl)**	
QY	0.14		0.18		0.34		0.37	
J, 10^{-13} $M^{-1}cm^3$	1.16		1.19		1.26		1.22	
R_0, Å	38.0		39.8		44.7		45.0	
m	*E*, %	*r*, Å	*E*, %	*r*, Å	*E*, %	*r*, Å	*E*, %	*r*, Å
0.5	23.9	41.1	20.8	44.3	10.9	56.5	5.4	64.7
5	74.9	41.5	70.6	45.0	47.3	59.5	24.4	71.1
10	82.8	43.0	83.7	44.5	66.9	58.3	40.1	70.7

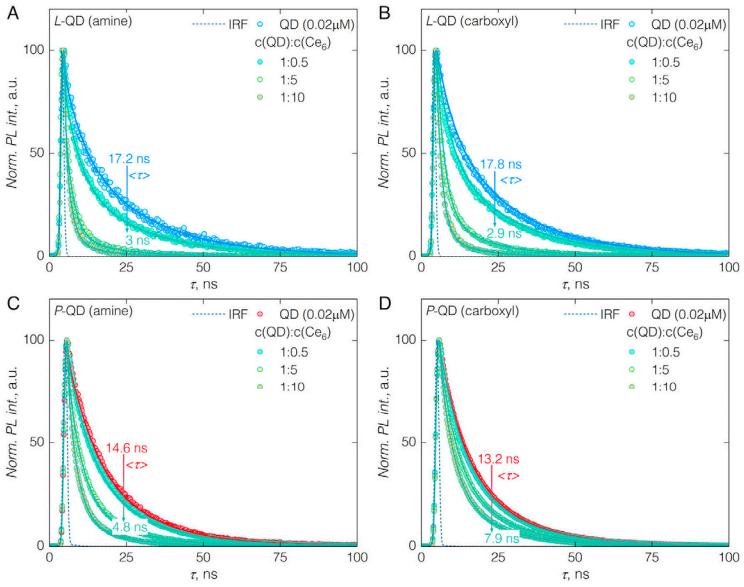

Figure 4. PL decay time (λ_{ex} = 405 nm; λ_{em} = 605 nm) of pure QDs and in the QD-Ce_6 complex at QD:Ce_6 molar concentration ratio of 1:0.5, 1:5 and 1:10. (**A**) *L*-QD(amine)-Ce_6; (**B**) *L*-QD(carboxyl)-Ce_6; (**C**) *P*-QD(amine)-Ce_6; (**D**) *P*-QD(carboxyl)-Ce_6. Amplitude-weighted lifetimes were obtained from tri-exponential fits of the PL decay curves. Instrument response function (IRF) is shown for each case.

In order to validate the presence of Ce_6 close to the surface of QDs, we have determined the relative center-to-center distance r between different types of QDs and Ce_6. PL *QY* for each type of QD was estimated *via* the comparative method, Rhodamine B served as a reference [29]; and obtained values (Table 1) were in line with those reported for QDs of similar structure [30,31]. The spectral overlap integral J and Förster distance R_0 between different QDs and Ce_6 was calculated according to Equations 2 and 3, respectively [32].

$$J = \frac{\sum F_D(\lambda)\varepsilon_A(\lambda)\lambda^4\Delta\lambda}{\sum F_D(\lambda)\Delta\lambda} \quad (2)$$

F_D is the emission spectrum of QDs, ε_A is the molar extinction coefficient of Ce_6, and λ is the wavelength in nanometers.

$$R_0 = 0.211\left(\kappa^2 n^{-4}\Phi_D J(\lambda)\right)^{\frac{1}{6}} \quad (3)$$

Φ_D is the quantum yield of the QDs' photoluminescence, n is the refractive index of the medium (here, 1.33), and κ^2 is a dipole orientation factor (here, 2/3—assuming random orientation of the QDs and Ce_6 upon binding). The presence of multiple acceptors (Ce_6) m with respect to a single donor (QD) was taken into account for r assessment (Equation 4).

$$E = \frac{mR_0^6}{mR_0^6 + r^6} \quad (4)$$

All of the obtained values are presented in Table 1. Relative *QY* was found to be similar between the same coating bearing QDs irrespective of the surface charge. Notably, *QY* of *P*-QDs was more than twice greater than that of *L*-QDs. While fairly similar PL band widths and peak positions of the investigated QDs yielded comparable spectral overlap values.

Förster distance R_0 (representing the donor-acceptor separation at 50% FRET efficiency) on average was approximately 45 Å for *P*-QDs, as compared to 38 and 40 Å for *L*-QD(amine) and *L*-QD(carboxyl). Differences for higher R_0 values in the case of *P*-QDs can be directly attributed to higher QY of these QDs. Finally, the average donor-acceptor center-to-center separation r in QD-Ce_6 complexes was around 42 and 45 Å for *L*-QD(amine)-Ce_6 and *L*-QD(carboxyl)-Ce_6, respectively. In the case of *P*-QDs, Ce_6 was separated by 58 and 69 Å from *P*-QD(amine) and *P*-QD(carboxyl), respectively. It is worth noting that higher r values in the latter case represent a situation for which exact number m of bound Ce_6 molecules is unknown due to slower binding kinetics, and thus are indicative only of the delayed complex formation (Figure S2). As a result, we have confirmed that complex formation is instantaneous between Ce_6 and *L*-QDs, while it requires more time for Ce_6 to intercalate into the amphiphilic polymer of *P*-QDs.

When further deliberating about the presence of Ce_6 in the coating of QDs, and subsequent FRET, it is worth noting that the refractive index specific to that microenvironment and not water has to be taken into account. The refractive index n, for phospholipids and amphiphilic polymers, might take values in the range of 1.4–1.6 [33,34]. We have checked for the effect of the refractive index on the R_0 and r, varying the value of n in Equation 3 from 1.33 to 1.6 (Figure S3A). With increasing n, R_0 decreased by 0.5 nm for the different QD-Ce_6 complexes. Similarly, the r values decreased by 0.5 nm for both types of *L*-QD-Ce_6 and 0.8 nm for *P*-QD-Ce_6. Although these differences might appear small, it is important to recognize that Ce_6 molecules can approach the surface of QD closer than thought initially. In fact, assuming the radius of *L*-QDs and Ce_6 to be approximately 3.6 and 0.5 nm, respectively [35], the shortest possible distance between the two is within the calculated range of $r = 3.8 \div 4.2$ nm for *L*-QD-Ce_6 (Figure S3C). On the other hand, although it is supposed that electric dipoles of QDs and bound Ce_6 molecules have random orientation when energy transfer takes place, hence κ^2 is 2/3, we cannot completely rule out the possibility of preferential orientation of Ce_6 when intercalated in the amphiphilic coating of QDs. Introducing this prospect (by varying κ^2 values in 2/3–4 range), we observe an increase in the R_0 and r values (Figure S3B), eluding to the possible greater separation between QDs and Ce_6 to achieve the same energy transfer efficiencies, if specific—non-random—orientation could be assumed.

3.3. Cellular Accumulation of QD-Ce_6 in Serum-Free Environment and PDT

To assess cellular internalization of QD-Ce_6 complex and its PDT activity, we have performed *in vitro* testing of all four variants in the triple-negative basal-like breast cancer cell line MDA-MB-231, notorious for its aggressiveness and cancer stem-like properties—showing resistance to conventional cancer treatment methods [36,37].

Notably, in the biological medium, surface charged QDs are rapidly coated with various proteins forming the so-called protein corona. Surface charge of QDs has an effect on the composition of the resulting protein corona, and their cellular uptake is often ascribed to the proteins assembled on the QDs' surface [38,39]. To avoid serum-determined accumulation, QDs and QD-Ce_6 complexes were incubated in the serum-free medium. QD-Ce_6 complexes accumulated inside the cells (Figure 5) in the manner of pure QDs, rather than of Ce_6. QDs are known to enter cells *via* endocytosis, localizing inside endocytic vesicles [40–42]. Meanwhile, Ce_6 diffuses through the membrane and labels cells in a relatively uniform pattern with a slight selectivity to lipid membranes due to its amphiphilicity (Figure 5). We have observed that negatively charged QDs and their QD-Ce_6 complexes were taken up by the cells noticeably better than their amine terminated counterparts. Additionally, cellular entry of QD-Ce_6 complexes was influenced by the coating type, as *P*-QDs were internalized by cancer cells better than *L*-QDs. NPs' surface chemistry greatly affects the efficiency of cellular accumulation and previous studies have showed that negatively charged NPs are internalized more rapidly than those of neutral or positive charge [43,44]. It is believed that carboxyl terminated QDs cluster at cationic sites of otherwise negative cell membrane, promoting NPs' uptake. Additionally, suppressed accumulation of carboxyl terminated *L*-QDs might be explained by the presence of PEG. Due to its "stealth" properties,

PEG reduces interaction with cellular membrane proteins, thus internalization of PEG coated NPs is restrained compared with non-PEGylated NPs [45].

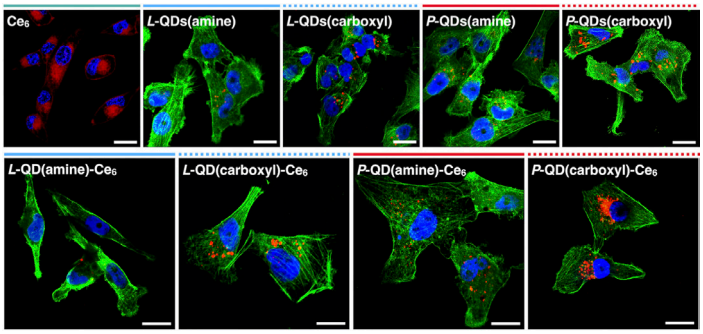

Figure 5. Accumulation of Ce_6, QDs with various surface coatings, and their respective complexes in MDA-MB-231 breast cancer cells. Red—Ce_6 (in the Ce_6 image) or QDs (in all the QD and QD-Ce_6 images); green—actin filaments; blue—nuclei. Scale bars in all images are 20 μm.

We further tested the PDT effect of the QD-Ce_6 complexes, induced solely *via* FRET—impinging light that is absorbed only by QDs and not Ce_6. MDA-MB-231 cells, treated with various QD-Ce_6 complexes, were irradiated under 470 nm light, and their viability was checked based on the number of alive (green) and dead (red) cells (Figure 6A). In correlation with cellular accumulation dynamics, PDT efficiency depended strongly on the type of the QDs' coating. First, the PDT effect was evident only in cells treated with carboxyl-functionalized QD-Ce_6 complexes. As cellular internalization of amine-functionalized QD-Ce_6 complexes was restricted, these variants showed negligible phototoxicity towards cells. Second, *L*-QD(carboxyl)-Ce_6 induced a 42% decrease in cancer cell viability and apoptotic-like morphology, while *P*-QD(carboxyl)-Ce_6 demonstrated 100% phototoxicity (Figure 6B). As the formation of QD-Ce_6 complexes was given enough time to equilibrate before being applied to cells, any differences in FRET activity could not account for the observed more efficient PDT, and thus were attributed solely to the better uptake of amphiphilic *P*-QD(carboxyl)-Ce_6 inside the cells. It is also worth pointing out that despite the absence of covalent linking, Ce_6 was retained within the coating of internalized QDs, since control cells treated only with *P*-QD(carboxyl) or Ce_6, and irradiated with 470 nm light, remained unaffected and viable (Figure 6A).

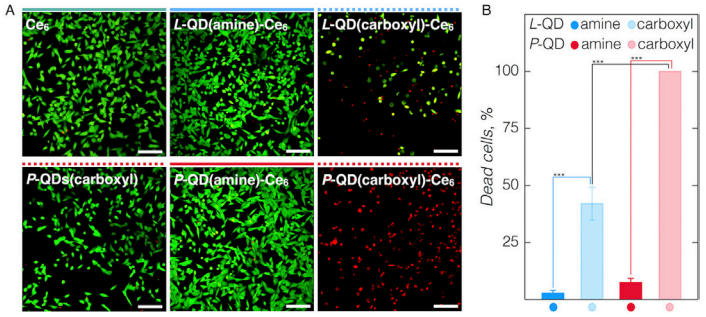

Figure 6. (**A**) Live (green)/Dead (red) images of cancer cells treated with different QD-Ce_6 complexes for 24 h and subjected to 470 nm irradiation at 17.7 J/cm^2 dosage. Images of the control experiments done with Ce_6 or *P*-QD(carboxyl) alone are also presented. Scale bars in all images are 100 μm. (**B**) Respective percentages of dead cells in each studied case. Significant differences $p < 0.0001$ are indicated with asterisks.

4. Conclusions

We have explored the possibility of QD-Ce_6 complex as a potential candidate for PDT, investigating the influence on the complex formation and activity of the QDs' coating. Namely, negatively and positively charged QDs with phospholipid or amphiphilic polymer coatings were investigated. We have observed rapid QD-Ce_6 complex formation for phospholipids bearing QDs, irrespective of their surface charge. While, QD-Ce_6 complex with amphiphilic polymer coated QDs formed at a much slower rate. For each complex, effective energy transfer from QDs to Ce_6 was observed. Following Förster's formalism, we have determined that hydrophobic interaction brings Ce_6 particularly close to the surface of QDs resulting in one of the most efficient FRET systems with an efficiency of up to 83.7%. *In vitro* experiments showed that only QD-Ce_6 complexes made of carboxyl terminated QDs have significant PDT activity, in direct correlation with their enhanced cellular uptake.

Overall, we have decisively shown the versatility of non-covalent QD-Ce_6 complexes, possible through a hydrophobic interaction of Ce_6 with various amphiphilic coatings of QDs. These systems proved to be robust and possess high FRET efficiency, which can be exploited for indirect mediation of PDT and cancer eradication.

Supplementary Materials: The following are available online at http://www.mdpi.com/2079-4991/9/1/9/s1. Figure S1: Absorption and emission spectra of *L*- and *P*-QDs, Figure S2: Fluorescence excitation spectrum of Ce_6, Figure S3: Change of *L*- and *P*-QD-Ce_6 PL signals with time, Figure S4: R_0, r values vs n and κ^2, and schematic representation of QD-Ce_6 complex.

Author Contributions: A.S. and D.D. performed the experiments, data analysis and drafted the manuscript. J.V., V.K., and R.R. conceptualized and supervised the work and contributed to the manuscript editing and validation.

Funding: The work was supported by the project "Postdoctoral Fellowship Implementation in Lithuania" funded by the European Union Structural Fund and by the project "Programming cells and management of tumor microenvironment for personal therapy in oncology–LASTER" (VP1-3.1-ŠMM-10-V-02-027).

Conflicts of Interest: The authors declare no conflicts of interest.

References

1. Michalet, X.; Pinaud, F.F.; Bentolila, L.A.; Tsay, J.M.; Doose, S.; Li, J.J.; Sundaresan, G.; Wu, A.M.; Gambhir, S.S.; Weiss, S. Quantum Dots for Live Cells, in Vivo Imaging, and Diagnostics. *Science* **2005**, *307*, 538–544. [CrossRef] [PubMed]
2. Samia, A.C.; Chen, X.; Burda, C. Semiconductor Quantum Dots for Photodynamic Therapy. *J. Am. Chem. Soc.* **2003**, *125*, 15736–15737. [CrossRef] [PubMed]
3. Hildebrandt, N.; Spillmann, C.M.; Algar, W.R.; Pons, T.; Stewart, M.H.; Oh, E.; Susumu, K.; Diaz, S.A.; Delehanty, J.B.; Medintz, I.L. Energy Transfer with Semiconductor Quantum Dot Bioconjugates: A Versatile Platform for Biosensing, Energy Harvesting, and Other Developing Applications. *Chem. Rev.* **2016**, *117*, 536–711. [CrossRef] [PubMed]
4. Shi, L.; Hernandez, B.; Selke, M. Singlet Oxygen Generation from Water-Soluble Quantum Dot-Organic Dye Nanocomposites. *J. Am. Chem. Soc.* **2006**, *128*, 6278–6279. [CrossRef] [PubMed]
5. Wu, S.-M.; Sun, X.-J.; Wang, L.-L.; Fei, M.-Y.; Yan, Z.-Y. Singlet Oxygen-Generating from Fluorescence Probes Based on Denatured Bovine Serum Albumin-Conjugated Cdte Quantum Dots and Photosensitizer Chlorin E6. *J. Nanopart. Res.* **2014**, *16*, 2701. [CrossRef]
6. Charron, G.; Stuchinskaya, T.; Edwards, D.R.; Russell, D.A.; Nann, T. Insights into the Mechanism of Quantum Dot-Sensitized Singlet Oxygen Production for Photodynamic Therapy. *J. Phys. Chem. C* **2012**, *116*, 9334–9342. [CrossRef]
7. Tsay, J.M.; Trzoss, M.; Shi, L.; Kong, X.; Selke, M.; Jung, M.E.; Weiss, S. Singlet Oxygen Production by Peptide-Coated Quantum Dot-Photosensitizer Conjugates. *J. Am. Chem. Soc.* **2007**, *129*, 6865–6871. [CrossRef]
8. Yaghini, E.; Pirker, K.F.; Kay, C.W.; Seifalian, A.M.; MacRobert, A.J. Quantification of Reactive Oxygen Species Generation by Photoexcitation of Pegylated Quantum Dots. *Small* **2014**, *10*, 5106–5115. [CrossRef]
9. Dayal, S.; Burda, C. Semiconductor Quantum Dots as Two-Photon Sensitizers. *J. Am. Chem. Soc.* **2008**, *130*, 2890–2891. [CrossRef]

10. Wen, Y.-N.; Song, W.-S.; An, L.-M.; Liu, Y.-Q.; Wang, Y.-H.; Yang, Y.-Q. Activation of Porphyrin Photosensitizers by Semiconductor Quantum Dots Via Two-Photon Excitation. *Appl. Phys. Lett.* **2009**, *95*, 143702. [CrossRef]
11. Skripka, A.; Valanciunaite, J.; Dauderis, G.; Poderys, V.; Kubiliute, R.; Rotomskis, R. Two-Photon Excited Quantum Dots as Energy Donors for Photosensitizer Chlorin E6. *J. Biomed. Opt.* **2013**, *18*, 078002. [CrossRef] [PubMed]
12. Pu, S.-C.; Yang, M.-J.; Hsu, C.-C.; Lai, C.-W.; Hsieh, C.-C.; Lin, S.H.; Cheng, Y.-M.; Chou, P.-T. The Empirical Correlation between Size and Two-Photon Absorption Cross Section of Cdse and Cdte Quantum Dots. *Small* **2006**, *2*, 1308–1313. [CrossRef] [PubMed]
13. Larson, D.R.; Zipfel, W.R.; Williams, R.M.; Clark, S.W.; Bruchez, M.P.; Wise, F.W.; Webb, W.W. Water-Soluble Quantum Dots for Multiphoton Fluorescence Imaging in Vivo. *Science* **2003**, *300*, 1434–1436. [CrossRef] [PubMed]
14. Orlova, A.O.; Martynenko, I.V.; Maslov, V.G.; Fedorov, A.V.; Gun'ko, Y.K.; Baranov, A.V. Investigation of Complexes of Cdte Quantum Dots with the Aloh-Sulphophthalocyanine Molecules in Aqueous Media. *J. Phys. Chem. C* **2013**, *117*, 23425–23431. [CrossRef]
15. Zenkevich, E.; Cichos, F.; Shulga, A.; Petrov, E.P.; Blaudeck, T.; von Borczyskowski, C. Nanoassemblies Designed from Semiconductor Quantum Dots and Molecular Arrays. *J. Phys. Chem. B* **2005**, *109*, 8679–8692. [CrossRef] [PubMed]
16. Valanciunaite, J.; Klymchenko, A.S.; Skripka, A.; Richert, L.; Steponkiene, S.; Streckyte, G.; Mely, Y.; Rotomskis, R. A Non-Covalent Complex of Quantum Dots and Chlorin E6: Efficient Energy Transfer and Remarkable Stability in Living Cells Revealed by Flim. *RSC Adv.* **2014**, *4*, 52270–52278. [CrossRef]
17. Valanciunaite, J.; Skripka, A.; Streckyte, G.; Rotomskis, R. Complex of Water-Soluble Cdse/Zns Quantum Dots and Chlorin E6: Interaction and Fret. *Laser Appl. Life Sci.* **2010**, *7376*, 737607. [CrossRef]
18. Steponkiene, S.; Valanciunaite, J.; Skripka, A.; Rotomskis, R. Cellular Uptake and Photosensitizing Properties of Quantum Dot-Chlorin E6 Complex: In Vitro Study. *J. Biomed. Nanotechnol.* **2014**, *10*, 679–686. [CrossRef]
19. Karabanovas, V.; Skripka, A.; Valanciunaite, J.; Kubiliute, R.; Poderys, V.; Rotomskis, R. Formation of Self-Assembled Quantum Dot–Chlorin E6 Complex: Influence of Nanoparticles Phospholipid Coating. *J. Nanopart. Res.* **2014**, *16*, 2508. [CrossRef]
20. Valančiūnaitė, J.; Skripka, A.; Araminaitė, R.; Kalantojus, K.; Streckytė, G.; Rotomskis, R. Spectroscopic Study of Non-Covalent Complex Formation between Different Porphyrin Analogues and Quantum Dots with Lipidbased Coating. *Chemija* **2011**, *22*, 181–187.
21. Skripka, A.; Marin, R.; Benayas, A.; Canton, P.; Hemmer, E.; Vetrone, F. Covering the Optical Spectrum through Collective Rare-Earth Doping of NaGdF4 Nanoparticles: 806 and 980 nm Excitation Routes. *Phys. Chem. Chem. Phys.* **2017**, *19*, 11825–11834. [CrossRef] [PubMed]
22. Dapkute, D.; Steponkiene, S.; Bulotiene, D.; Saulite, L.; Riekstina, U.; Rotomskis, R. Skin-Derived Mesenchymal Stem Cells as Quantum Dot Vehicles to Tumors. *Int. J. Nanomed.* **2017**, *12*, 8129–8142. [CrossRef] [PubMed]
23. Frolov, A.A.; Zenkevich, E.I.; Gurinovich, G.P.; Kochubeyev, G.A. Chlorin E6-Liposome Interaction. Investigation by the Methods of Fluorescence Spectroscopy and Inductive Resonance Energy Transfer. *J. Photochem. Photobiol. B* **1990**, *7*, 43–56. [CrossRef]
24. Mojzisova, H.; Bonneau, S.; Vever-Bizet, C.; Brault, D. The Ph-Dependent Distribution of the Photosensitizer Chlorin E6 among Plasma Proteins and Membranes: A Physico-Chemical Approach. *Biochim. Biophys. Acta* **2007**, *1768*, 366–374. [CrossRef] [PubMed]
25. Aluigi, A.; Sotgiu, G.; Ferroni, C.; Duchi, S.; Lucarelli, E.; Martini, C.; Posati, T.; Guerrini, A.; Ballestri, M.; Corticelli, F.; et al. Chlorin E6 Keratin Nanoparticles for Photodynamic Anticancer Therapy. *RSC Adv.* **2016**, *6*, 33910–33918. [CrossRef]
26. Parak, W.J.; Pellegrino, T.; Plank, C. Labelling of Cells with Quantum Dots. *Nanotechnology* **2005**, *16*, R9–R25. [CrossRef]
27. Pellegrino, T.; Manna, L.; Kudera, S.; Liedl, T.; Koktysh, D.; Rogach, A.L.; Keller, S.; Rädler, J.; Natile, G.; Parak, W.J. Hydrophobic Nanocrystals Coated with an Amphiphilic Polymer Shell: A General Route to Water Soluble Nanocrystals. *Nano Lett.* **2004**, *4*, 703–707. [CrossRef]

28. Martynenko, I.V.; Orlova, A.O.; Maslov, V.G.; Baranov, A.V.; Fedorov, A.V.; Artemyev, M. Energy Transfer in Complexes of Water-Soluble Quantum Dots and Chlorin E6 Molecules in Different Environments. *Beilstein J. Nanotechnol.* **2013**, *4*, 895–902. [CrossRef]
29. Magde, D.; Rojas, G.E.; Seybold, P.G. Solvent Dependence of the Fluorescence Lifetimes of Xanthene Dyes. *Photochem. Photobiol.* **1999**, *70*, 737–744. [CrossRef]
30. Dabbousi, B.O.; Rodriguez-Viejo, J.; Mikulec, F.V.; Heine, J.R.; Mattoussi, H.; Ober, R.; Jensen, K.F.; Bawendi, M.G. (Cdse)Zns Core−Shell Quantum Dots: Synthesis and Characterization of a Size Series of Highly Luminescent Nanocrystallites. *J. Phys. Chem. B* **1997**, *101*, 9463–9475. [CrossRef]
31. Gerion, D.; Pinaud, F.; Williams, S.C.; Parak, W.J.; Zanchet, D.; Weiss, S.; Alivisatos, A.P. Synthesis and Properties of Biocompatible Water-Soluble Silica-Coated Cdse/Zns Semiconductor Quantum Dots. *J. Phys. Chem. B* **2001**, *105*, 8861–8871. [CrossRef]
32. Lakowicz, J. *Principles of Fluorescence Spectroscopy*; Springer: New York, NY, USA, 2006; Volume 1.
33. Howland, M.C.; Szmodis, A.W.; Sanii, B.; Parikh, A.N. Characterization of Physical Properties of Supported Phospholipid Membranes Using Imaging Ellipsometry at Optical Wavelengths. *Biophys. J.* **2007**, *92*, 1306–1317. [CrossRef] [PubMed]
34. Lü, C.; Yang, B. High Refractive Index Organic–Inorganic Nanocomposites: Design, Synthesis and Application. *J. Mater. Chem.* **2009**, *19*, 2884–2901. [CrossRef]
35. Jennings, T.L.; Becker-Catania, S.G.; Triulzi, R.C.; Tao, G.; Scott, B.; Sapsford, K.E.; Spindel, S.; Oh, E.; Jain, V.; Delehanty, J.B.; et al. Reactive Semiconductor Nanocrystals for Chemoselective Biolabeling and Multiplexed Analysis. *ACS Nano* **2011**, *5*, 5579–5593. [CrossRef] [PubMed]
36. Mercatali, L.; La Manna, F.; Groenewoud, A.; Casadei, R.; Recine, F.; Miserocchi, G.; Pieri, F.; Liverani, C.; Bongiovanni, A.; Spadazzi, C.; et al. Development of a Patient-Derived Xenograft (PDX) of Breast Cancer Bone Metastasis in a Zebrafish Model. *Int. J. Mol. Sci.* **2016**, *17*, 1375. [CrossRef] [PubMed]
37. Xiong, G.; Stewart, R.L.; Chen, J.; Gao, T.; Scott, T.L.; Samayoa, L.M.; O'Connor, K.; Lane, A.N.; Xu, R. Collagen Prolyl 4-Hydroxylase 1 Is Essential for Hif-1α Stabilization and Tnbc Chemoresistance. *Nat. Commun.* **2018**, *9*, 4456. [CrossRef] [PubMed]
38. Fleischer, C.C.; Payne, C.K. Nanoparticle Surface Charge Mediates the Cellular Receptors Used by Protein-Nanoparticle Complexes. *J. Phys. Chem. B* **2012**, *116*, 8901–8907. [CrossRef]
39. Frohlich, E. The Role of Surface Charge in Cellular Uptake and Cytotoxicity of Medical Nanoparticles. *Int. J. Nanomed.* **2012**, *7*, 5577–5591. [CrossRef]
40. Karabanovas, V.; Zitkus, Z.; Kuciauskas, D.; Rotomskis, R.; Valius, M. Surface Properties of Quantum Dots Define Their Cellular Endocytic Routes, Mitogenic Stimulation and Suppression of Cell Migration. *J. Biomed. Nanotechnol.* **2014**, *10*, 775–786. [CrossRef]
41. Damalakiene, L.; Karabanovas, V.; Bagdonas, S.; Rotomskis, R. Fluorescence-Lifetime Imaging Microscopy for Visualization of Quantum Dots' Endocytic Pathway. *Int. J. Mol. Sci.* **2016**, *17*, 473. [CrossRef]
42. Damalakiene, L.; Karabanovas, V.; Bagdonas, S.; Valius, M.; Rotomskis, R. Intracellular Distribution of Nontargeted Quantum Dots after Natural Uptake and Microinjection. *Int. J. Nanomed.* **2013**, *8*, 555–568. [CrossRef] [PubMed]
43. Ryman-Rasmussen, J.P.; Riviere, J.E.; Monteiro-Riviere, N.A. Variables Influencing Interactions of Untargeted Quantum Dot Nanoparticles with Skin Cells and Identification of Biochemical Modulators. *Nano Lett.* **2007**, *7*, 1344–1348. [CrossRef] [PubMed]
44. Lunov, O.; Syrovets, T.; Loos, C.; Beil, J.; Delacher, M.; Tron, K.; Nienhaus, G.U.; Musyanovych, A.; Mailander, V.; Landfester, K.; et al. Differential Uptake of Functionalized Polystyrene Nanoparticles by Human Macrophages and a Monocytic Cell Line. *ACS Nano* **2011**, *5*, 1657–1669. [CrossRef] [PubMed]
45. Pelaz, B.; del Pino, P.; Maffre, P.; Hartmann, R.; Gallego, M.; Rivera-Fernandez, S.; de la Fuente, J.M.; Nienhaus, G.U.; Parak, W.J. Surface Functionalization of Nanoparticles with Polyethylene Glycol: Effects on Protein Adsorption and Cellular Uptake. *ACS Nano* **2015**, *9*, 6996–7008. [CrossRef] [PubMed]

6 publikacija / 6th publication

Hitchhiking nanoparticles: mesenchymal stem cell-mediated delivery of theranostic nanoparticles

Dapkute D, Pleckaitis M, Bulotiene D, Daunoravicius D, Rotomskis R, Karabanovas V.

ACS Applied Materials & Interfaces (2021)

Priimtas/accepted

.

UŽRAŠAMS

Vilniaus universiteto leidykla
Saulėtekio al. 9, III rūmai, LT-10222 Vilnius
El. p. info@leidykla.vu.lt, www.leidykla.vu.lt
Tiražas 15 egz.